Limits on $\nu_\mu \leftrightarrow \nu_{sterile}$ Oscillations by the π^0/μ Measurement in the Water Cherenkov Detectors

Shoei Nakayama

February 17, 2003

Abstract

Super-Kamiokande has reported evidence for oscillations of atmospheric muon neutrinos in the $\nu_\mu \leftrightarrow \nu_\tau$ mode or in the $\nu_\mu \leftrightarrow \nu_s$ mode. One of the ways to distinguish between $\nu_\mu \leftrightarrow \nu_\tau$ and $\nu_\mu \leftrightarrow \nu_s$ is measuring a double ratio $R_{\pi^0} = (\pi^0/\mu)_{\mathrm{Data}} / (\pi^0/\mu)_{\mathrm{MC}}$ for the atmospheric neutrino sample in Super-Kamiokande. Since the single π^0 sample has a large NC fraction, the two scenarios make a difference in R_{π^0}.

To test our Monte Carlo simulation and reduce the systematic uncertainty on R_{π^0}, we have made a measurement of R_{π^0} in the 1kt water Cherenkov detector using K2K beam neutrinos before oscillations. We obtained R_{π^0} equal to unity, indicating very good agreement between the observed data and our Monte Carlo expectation. The measurement uncertainty on R_{π^0} in the 1kt detector is estimated to be about 9 %.

We carefully applied this result to SK R_{π^0} in the neutrino energy region from 500 MeV to 2500 MeV, over which neutrinos producing 1kt π^0 events were distributed. The total systematic uncertainty on SK R_{π^0} was reduced from 20 % to 14 %. Using the events observed in a 1489.2 live days exposure of Super-Kamiokande, the measured R_{π^0} is found to be more consistent with the $\nu_\mu \leftrightarrow \nu_\tau$ oscillation hypothesis, while the $\nu_\mu \leftrightarrow \nu_s$ oscillation hypothesis is about $1.3\,\sigma$ away at the Super-Kamiokande's best fit oscillation parameters.

Though this analysis is independent of matter effects in the test region of Δm^2 above $1.0 \times 10^{-3}\,\mathrm{eV}^2$, our result is consistent with the result obtained by the SK analysis using matter effects on high energy muon neutrinos.

Acknowledgments

I would like to thank all the people who supported and encouraged me during my time in graduate school. I am grateful to my advisor Yoji Totsuka for involving me with great experiments, Super-Kamiokande and K2K. In spite of his busyness as the leader of SK, he was always willing to spare the time for advising me. I further owe my sincerest thanks to Yoshitaka Itow. I have learned a lot of things under his excellent guidance. This thesis would never be completed without his hearty support.

I would also like to extend my gratitude to K.Nishikawa, K.Nakamura, Y.Suzuki, T.Kajita, H.W.Sobel, J.L.Stone, C.K.Jung, and R.J.Wilkes. Their management of both experiments enables me to accomplish my works. Thanks to the cooperation of Kamioka Mining and Smelting Company and the diligent efforts of the KEK-PS machine and beam channel groups. I gratefully acknowledge the financial support by the Japan Society for the Promotion of Science.

I am grateful to all the members of the K2K-1kt group, especially C.M.Mauger, M.Miura, T.Nakaya, A.K.Ichikawa, I.Kato, A.Shima, C.McGrew, E.Sharkey, K.Mack, J.Zalipska, and S.Mine. I have had many useful discussions with them. It has been a pleasure. The analysis presented in this thesis also depends on the hard work by all the members of the SK-atmpd group, especially K.Kaneyuki, M.Shiozawa, S.Moriyama, K.Ishihara, K.Okumura, Y.Obayashi, T.Toshito, J.Kameda, K.Kobayashi, M.Ishitsuka, E.Kearns, C.Yanagisawa, D.Casper, M.Messier, and A.Kibayashi. This thesis is greatly indebted to them.

I would like to thank M.Nakahata, Y.Fukuda, Y.Takeuchi, Y.Koshio, H.Ishino, T.Namba, and N.Sakurai. They were willing to give me their useful knowledge during my time in Kamioka. In KEK, I got a lot of benefit from M.Sakuda, T.Kobayashi, T.Ishii, Y.Oyama, T.Hasegawa, A.Suzuki, T.Ishida, M.Kohama, T.Maruyama, Y.Hayato, T.Inagaki, and M.Yoshida. I am also thankful to all the staffs in the Kamioka Observatory for their continuous support.

I would like to express my special thanks to my fellows, S.Yamada, K.Kobayashi, Y.Kobayashi, H.Takeuchi, M.Ishitsuka, S.Fukuda, T.Ooyabu, C.Saji, K.Nitta, Y.Gando, C.Mitsuda, T.Kato. We had some discussions related to physics and many discussions unrelated to physics. We went from place to place by car. We always amused each other with tricks. I am very fortune to have their continued friendship.

My deepest appreciation goes to my parents. This work is dedicated to them.

Contents

Chapter 1

Introduction

1.1 Atmospheric Neutrino

When primary cosmic rays interact with nuclei in the earth's atmosphere, many secondary mesons, mostly pions and some kaons, are produced in hadronic showers :

$$p\,(\mathrm{He}) + A_{\mathrm{air}} \rightarrow X + \pi^{\pm}, K^{\pm}, K^{0}, \cdots \tag{1.1}$$

where A_{air} represents a nucleus in the air, mainly nitrogen and oxygen, and X represents hadrons. Neutrinos are produced mainly by the following decay chains of secondary charged pions :

$$\begin{aligned} \pi^{+} &\rightarrow \mu^{+} + \nu_{\mu} \\ &\qquad \hookrightarrow e^{+} + \nu_{e} + \overline{\nu}_{\mu} \end{aligned} \tag{1.2}$$

$$\begin{aligned} \pi^{-} &\rightarrow \mu^{-} + \overline{\nu}_{\mu} \\ &\qquad \hookrightarrow e^{-} + \overline{\nu}_{e} + \nu_{\mu} \end{aligned} \tag{1.3}$$

Thus, neutrinos produced in the atmosphere are called "atmospheric neutrinos". Note that from this decay chain, the expected flux ratio $(\nu_{\mu}+\overline{\nu}_{\mu})/(\nu_{e}+\overline{\nu}_{e})$ should be about two for relatively low energy neutrinos. For neutrinos of higher energies above a few GeV, this flavor ratio becomes greater than two because flight distances of pions become longer and there is less chance for muons to decay before reaching the ground.

The expected absolute flux of atmospheric neutrinos is shown in Figure 1.1 [1, 2]. The systematic uncertainty on the absolute flux of atmospheric neutrinos is estimated to be about 20 %, which mostly comes from the uncertainties on cross sections of hadronic interactions and on fluxes of primary cosmic ray components [1]. However, the flavor ratio $(\nu_{\mu} + \overline{\nu}_{\mu})/(\nu_{e} + \overline{\nu}_{e})$ is well known with about 5 % uncertainty over a broad range of neutrino energies from 0.1 GeV to 10 GeV, since neutrino productions are dominated by the charged pion decay chain in this energy range. The expected flavor ratio is shown in Figure 1.2-(a). Figure 1.2-(b) shows the prediction of $\nu/\overline{\nu}$ flux ratios. The ratios, which depend on the proton/neutron ratio of primaries, are also know with 5 % uncertainties.

Originally, the Kamiokande [3, 4] and IMB [5, 6] experiment studied atmospheric neutrinos as backgrounds to the nucleon decay search. These underground water Cherenkov detectors were able to identify the charged particles generated in neutrino interactions. The flavor double

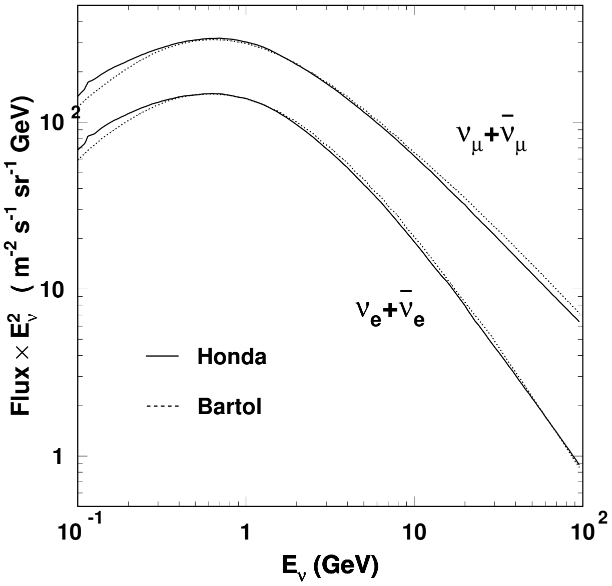

Figure 1.1: The expected flux of atmospheric neutrinos at the Kamioka site assuming middle solar activity. Solid lines show the Honda calculation [1] and dashed lines show the Bartol calculation [2].

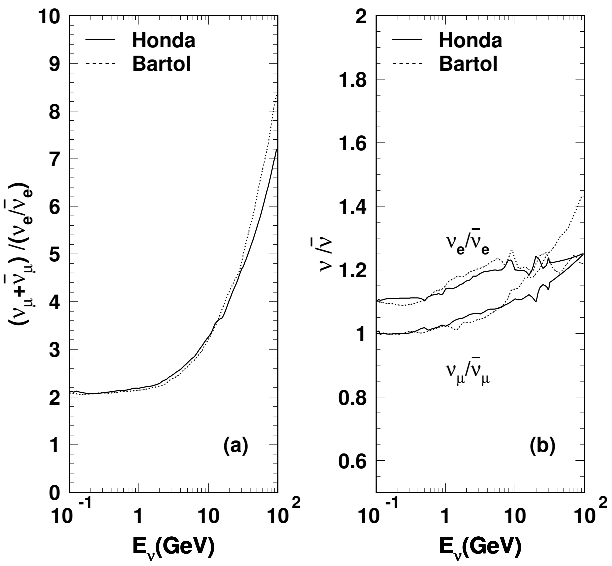

Figure 1.2: The expected atmospheric neutrino flux ratios (a) $(\nu_\mu+\overline{\nu}_\mu)/(\nu_e+\overline{\nu}_e)$ and (b) $\nu/\overline{\nu}$. Solid lines show the Honda calculation [1] and dashed lines show the Bartol calculation [2].

ratio was measured in both experiments :

$$R \equiv \frac{(\mu/e)_{\rm Data}}{(\mu/e)_{\rm MC}} \tag{1.4}$$

where $\mu(e)$ represents the number of events which appear to come from CC $\nu_\mu(\nu_e)$ interactions. The suffix 'Data' represents the result of observation and the suffix 'MC' represents the Monte Carlo prediction. The R obtained by Kamiokande and IMB were significantly lower than 1. This problem is sometimes called "atmospheric neutrino anomaly".

1.2 Neutrino Oscillation

Today, the answer to the atmospheric neutrino anomaly is thought to be neutrino oscillations. In the Standard Model of elementary particles, neutrinos are regarded as exactly massless particles [7, 8, 9]. However, there is no definite reason to forbid the finite mass of neutrinos. In 1962, Maki, Nakagawa and Sakata suggested if neutrinos have mass, their mass eigenstates might not be the same as their flavor eigenstates and they could mix, resulting in flavor oscillations of neutrinos [10].

Here, we consider neutrino oscillations between two flavors α and β. Using the mixing angle θ, flavor eigenstates can be expressed as superpositions of mass eigenstates $|\nu_1\rangle$ and $|\nu_2\rangle$:

$$\begin{pmatrix} |\nu_\alpha\rangle \\ |\nu_\beta\rangle \end{pmatrix} = \begin{pmatrix} \cos\theta & \sin\theta \\ -\sin\theta & \cos\theta \end{pmatrix} \begin{pmatrix} |\nu_1\rangle \\ |\nu_2\rangle \end{pmatrix} \equiv U \begin{pmatrix} |\nu_1\rangle \\ |\nu_2\rangle \end{pmatrix} \tag{1.5}$$

The time evolution of mass eigenstates is described as the solution of Schrödinger equation, like :

$$\begin{pmatrix} |\nu_1(t)\rangle \\ |\nu_2(t)\rangle \end{pmatrix} = \begin{pmatrix} \exp(-iE_1 t) & 0 \\ 0 & \exp(-iE_2 t) \end{pmatrix} \begin{pmatrix} |\nu_1(0)\rangle \\ |\nu_2(0)\rangle \end{pmatrix} \tag{1.6}$$

where E_1 and E_2 are eigenvalues of mass eigenstates $|\nu_1\rangle$ and $|\nu_2\rangle$, respectively. Therefore the time evolution of flavor eigenstates is :

$$\begin{pmatrix} |\nu_\alpha(t)\rangle \\ |\nu_\beta(t)\rangle \end{pmatrix} = U \begin{pmatrix} \exp(-iE_1 t) & 0 \\ 0 & \exp(-iE_2 t) \end{pmatrix} U^{-1} \begin{pmatrix} |\nu_\alpha(0)\rangle \\ |\nu_\beta(0)\rangle \end{pmatrix} \tag{1.7}$$

Suppose that ν_α is produced in a weak interaction at $t = 0$, its survival probability is calculated as :

$$\begin{aligned} P(\nu_\alpha \to \nu_\alpha) &= |\langle \nu_\alpha(0)|\nu_\alpha(t)\rangle|^2 && (1.8) \\ &= 1 - \sin^2 2\theta \sin^2\left(\frac{(E_2 - E_1)L}{2}\right) && (1.9) \end{aligned}$$

where t is replaced with neutrino flight length L. If neutrinos have very small but finite mass, the following approximation can be used :

$$\begin{aligned} E_2 - E_1 &= \sqrt{m_2^2 + p_2^2} - \sqrt{m_1^2 + p_1^2} \\ &\simeq \left(p + \frac{m_2^2}{2p}\right) - \left(p + \frac{m_1^2}{2p}\right) \\ &\simeq \frac{\Delta m^2}{2E} && (1.10) \end{aligned}$$

where $p_1 = p_2 \simeq E$ is assumed, and $\Delta m^2 \equiv m_2^2 - m_1^2$.

Finally, the survival probability of ν_α is given by :

$$P(\nu_\alpha \to \nu_\alpha) = 1 - \sin^2 2\theta \sin^2 \left(\frac{\Delta m^2 L}{4E}\right) \tag{1.11}$$

$$= 1 - \sin^2 2\theta \sin^2 \left(\pi \frac{L}{l}\right) \tag{1.12}$$

where $l \equiv 4\pi E/\Delta m^2$ is the oscillation length. For the given neutrino energy E, the survival probability P oscillates as a function of its flight length L. This phenomenon is called neutrino oscillation.

In 1996, Super-Kamiokande [11, 12], a larger type of Kamiokande, started its observation. One of the main aims of this experiment is to observe atmospheric neutrinos with much higher statistics and precision and solve the atmospheric neutrino anomaly problem. Two years later, Super-Kamiokande concluded that their measurement results gave the evidence for neutrino oscillation [13].

Figure 1.3 shows the zenith angle distributions for atmospheric neutrino events observed in a 1489.2 live days exposure of Super-Kamiokande [14]. The zenith angle of a neutrino corresponds to its baseline L, the distance from the neutrino production point to the detection point. The upward-going ($\cos\theta \simeq -1$) neutrinos are produced in the atmosphere of the opposite side of the globe and travel more than 10000 km through the earth, while the downward-going ($\cos\theta \simeq 1$) neutrinos only travels of the order of 10 km from the upper atmosphere. Thus, by measuring the zenith angle distributions, atmospheric neutrino experiments vary the neutrino baseline L. The figures also show the atmospheric neutrino Monte Carlo expectations with no oscillations and with $\nu_\mu \leftrightarrow \nu_\tau$ oscillations at best fit oscillation parameters $(\sin^2 2\theta, \Delta m^2) = (1.00,\ 2.5\times10^{-3}$ eV^2). The expectation with $\nu_\mu \leftrightarrow \nu_\tau$ oscillations agrees very well with the observed data. The 90 % confidence level allowed parameter region for $\nu_\mu \leftrightarrow \nu_\tau$ oscillations is as follows [14]:

$$\sin^2 2\theta > 0.92 \tag{1.13}$$

$$1.6 \times 10^{-3}(\mathrm{eV}^2) < \Delta m^2 < 3.9 \times 10^{-3}(\mathrm{eV}^2) \tag{1.14}$$

To confirm the existence of neutrino oscillations and measure oscillation parameters more accurately, the first accelerator long-baseline experiment, K2K, started in 1999 [15]. A beam of almost pure ν_μ with an energy spectrum similar to atmospheric neutrinos is created using a proton synchrotron at KEK and steered through the earth toward Super-Kamiokande. With its base-line of 250 km and neutrino energies around 1 GeV, K2K is designed to test the parameter region allowed in the atmospheric neutrino analyses.

There are two more Δm^2 regions favored by experiments.

Super-Kamiokande has observed solar neutrinos [16], which are electron neutrinos generated by nuclear interactions inside the sun, as well as atmospheric neutrinos. Since energies of solar neutrinos are in the range from several 100 keV to 15 MeV and their flight length is about 1.5×10^8 km, measurements of solar neutrinos are sensitive to Δm^2 down to $\sim 10^{-11}$ eV^2. The SNO experiment [17], which stated observations in 1999, has also observed solar neutrinos using

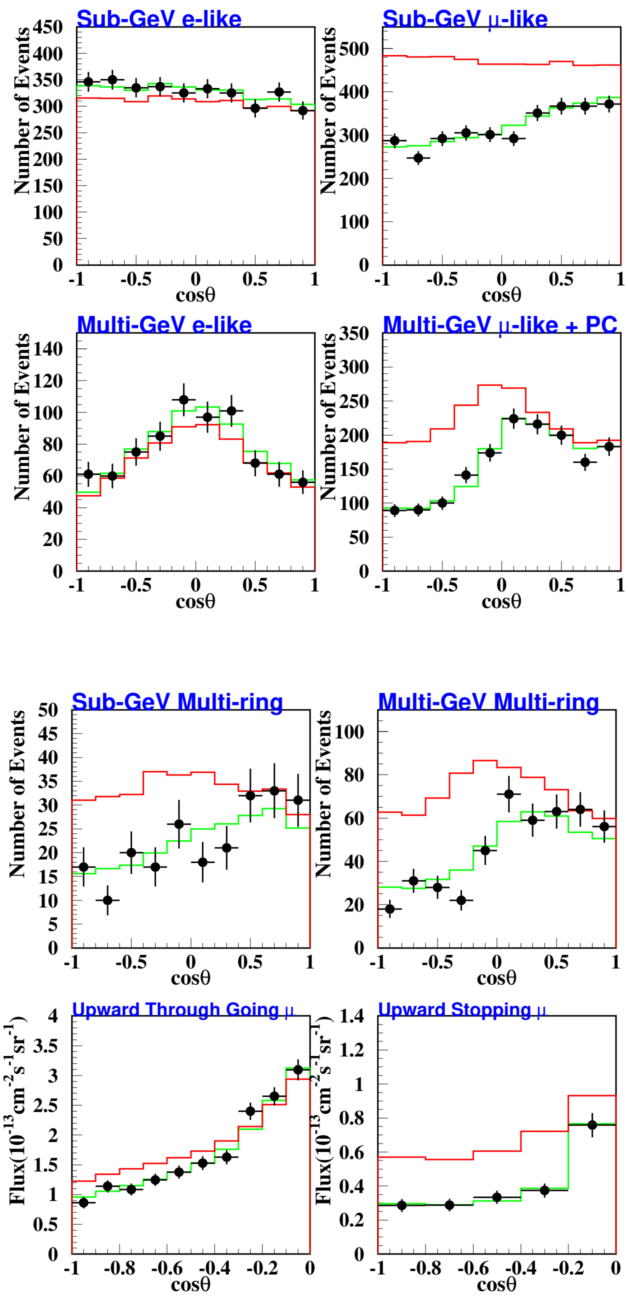

Figure 1.3: The zenith angle distributions for atmospheric neutrino events observed in a 1489.2 live days exposure of Super-Kamiokande [14]. $\cos\theta \simeq 1$ ($\cos\theta \simeq -1$) indicates downward-going (upward-going) direction. There also shown the distributions for the atmospheric neutrino Monte Carlo expectations with no oscillations (red histograms) and with $\nu_\mu \leftrightarrow \nu_\tau$ oscillations (green histograms) at best fit oscillation parameters $(\sin^2 2\theta, \Delta m^2) = (1.00,\ 2.5{\times}10^{-3}\ \mathrm{eV}^2)$.

the Cherenkov detector filled with heavy water, D_2O. Details are not given here, but these solar neutrino experiments indicate the existence of Δm^2 around $(3 \sim 25) \times 10^{-5}\text{eV}^2$ [18]. Recently, this result was confirmed using different source of neutrinos by the KamLAND experiment [19]. This experiment have searched for oscillations of $\overline{\nu}_e$'s emitted from distant power reactors. The $\overline{\nu}_e$ flux at the detector site is dominated by a few reactors at an average distance of $\sim 180\,\text{km}$. The energies of produced $\overline{\nu}_e$'s are around $3\,\text{MeV}$, so the experiment is sensitive to Δm^2 down to several 10^{-6}eV^2. After a 145 days exposure, the experiment gave the definite evidence for $\overline{\nu}_e$ disappearance.

Another Δm^2 region was suggested by LSND [20]. LSND (the Liquid Scintillation Neutrino Detector) was operated at Los Alamos National Lab from 1993 to 1998, searching for $\overline{\nu}_\mu \to \overline{\nu}_e$ oscillation. The experiment used $\overline{\nu}_\mu$'s as decay products of μ^+'s which were generated by the proton beam and stopped at the beam dump. These $\overline{\nu}_\mu$'s have energies of Michel spectrum ($E < 53\,\text{MeV}$). The detector holding mineral oil doped with small amount of scintillator was located about 30 m far from the neutrino production area. LSND reported the positive evidence of $\overline{\nu}_e$ appearance. The Δm^2 allowed is in the range above $0.05\,\text{eV}^2$ [20]. Notably, KARMEN which is a similar experiment to LSND has excluded a large fraction of the LSND allowed region [21]. Due to the exclusion from KARMEN and some reactor experiments, the remaining LSND allowed region of the Δm^2 is around $0.2 \sim 2\ \text{eV}^2$ [22].

1.3 Sterile Neutrino

As described in previous section, assuming these experiments are correct, there exists three different Δm^2's :

Atmospheric Neutrino Observation	$\Delta m^2 : (1 \sim 4) \times 10^{-3}\,\text{eV}^2$
Solar Neutrino and Reactor Neutrino Observation	$\Delta m^2 : (3 \sim 25) \times 10^{-5}\,\text{eV}^2$
LSND	$\Delta m^2 : (2 \sim 20) \times 10^{-1}\,\text{eV}^2$

These results imply at least four neutrino mass eigenstates. However, the number of active neutrino flavors are known to be three, as for neutrinos with mass less than half of the Z^0 mass, by precise measurements of the decay width of Z^0 boson using the high energy e^+e^- colliders, LEP at CERN and SLC at SLAC [23]. Thus, if there is a fourth generation of neutrino, it must be a neutrino which does not interact via weak current. Such a neutrino is called "sterile neutrino" and sometimes denoted by ν_s. All the experiments giving the evidence for neutrino oscillations see the disappearance of neutrinos, except for LSND. Therefore these neutrinos might oscillate into sterile neutrinos instead of active neutrinos.

One of the methods to distinguish active-active oscillations and active-sterile oscillations in a disappearance experiment is to measure the rate of NC interactions. In the active-active oscillation case, the reason for neutrino disappearance is that the oscillation takes place at the neutrino energy where the new active flavor is below threshold for CC interactions. The same is not true for NC interactions because a charged lepton is not produced. Therefore the NC rate should be the same as that without oscillations. However, in the active-sterile case, there should be attenuation of the NC rate as well as the CC rate.

Another way to distinguish the two cases is looking for the matter effect in the earth [24, 25, 26]. When a neutrino travels in matter, it is affected by a weak forward scattering potential.

Since the ordinary matter contains neither μ's nor τ's, the coherent forward scatterings of ν_μ and ν_τ are identical. Therefore the presence of matter in the neutrino way does not modify the probability of $\nu_\mu \leftrightarrow \nu_\tau$ oscillations. On the other hand, ν_s does not interact with matter even via neutral current. This introduces an effective potential which modifies the mixing angle and oscillation length :

$$P(\nu_\mu \to \nu_s) = \sin^2 2\theta_m \sin^2\left(\pi \frac{L}{l_m}\right) \tag{1.15}$$

$$\sin^2 2\theta_m = \frac{\sin^2 2\theta}{(\zeta - \cos 2\theta)^2 + \sin^2 2\theta} \tag{1.16}$$

$$l_m = \frac{l}{\sqrt{(\zeta - \cos 2\theta)^2 + \sin^2 2\theta}} \tag{1.17}$$

The parameter ζ is given by $\mp\sqrt{2}E_\nu G_F N_n/\Delta m^2$, where N_n is the neutron density in the matter, the minus sign is for neutrinos, and the plus sign is for anti-neutrinos. For the density of matter in the earth, ζ reaches unity for E_ν of $5\,\mathrm{GeV}\times\Delta m^2/(10^{-3}\mathrm{eV}^2)$. Assuming $\Delta m^2 = 3\times10^{-3}$ eV^2 near the Super-Kamiokande best fit, neutrinos with energy above approximately 15 GeV will have the oscillation probability suppressed by matter effect if the oscillation is $\nu_\mu \leftrightarrow \nu_s$.

In order to distinguish whether atmospheric ν_μ's are oscillating into ν_τ's or ν_s's, Super-Kamiokande has measured the zenith angle distributions of three independent data samples, one NC sample and two CC ν_μ samples produced by high energy neutrinos. Neither attenuation of NC rate nor suppression of CC disappearance has not been seen for upward-going events in each sample, and the $\nu_\mu \leftrightarrow \nu_s$ hypothesis was excluded at 99 % confidence level [27].

The analysis in this thesis is related to the former, the NC rate. In order to distinguish whether atmospheric muon neutrinos are oscillating into tau neutrinos or sterile neutrinos, we measure $R_{\pi^0} \equiv (\pi^0/\mu)_{\mathrm{Data}}/(\pi^0/\mu)_{\mathrm{MC}}$ in Super-Kamiokande, where π^0/μ represents the ratio of the number of π^0 events to the number of μ events. The single π^0 sample has the large NC fraction, while the μ-like sample mostly comes from CC interactions. This analysis is independent of matter effect, because neutrinos which produce the π^0 sample and the μ-like sample used in the analysis do not have sufficiently high energies to be affected by the matter in the earth.

Chapter 2

Super-Kamiokande Detector

2.1 Cherenkov Light

Super-Kamiokande is a large water Cherenkov detector. Cherenkov light is emitted as illustrated in Figure 2.1, when a charged particle travels in a medium with the velocity faster than the light velocity in the medium :

$$v \geq \frac{c}{n} \tag{2.1}$$

where v is the particle's velocity, n is the refractive index of the medium and c is the light velocity in vacuum. In water ($n \simeq 1.34$), the threshold momenta for Cherenkov radiation of electrons, muons and pions are about 0.57, 118 and 156 MeV/c, respectively.

Trajectories of emitted light form a cone along the charged particle's direction with a characteristic half angle of θ_C as :

$$\cos\theta_C = \frac{1}{n\beta} \tag{2.2}$$

where $\beta = v/c$. In water, the characteristic Cherenkov angle is about 42° for a energetic charged particle with $\beta \simeq 1$. The number of Cherenkov photons, dN, emitted during a particle's travel of dx has the following wavelength dependence :

$$\frac{d^2N}{dxd\lambda} = \frac{2\pi\alpha}{\lambda^2}\left(1 - \frac{1}{(n\beta)^2}\right) \tag{2.3}$$

where λ is the wavelength of emitted photons and α is the fine structure constant. In water, the number of emitted photons is roughly 340 photons/cm for the wavelength of 300 nm to 600 nm.

A Cherenkov cone projects a circular or oval image on a plane. Super-Kamiokande can recognize these Cherenkov ring images using the photomultiplier tubes arranged on the detector surface. Figure 2.2 shows a view of a typical simulated event in Super-Kamiokande.

2.2 Detector

Super-Kamiokande is the largest water Cherenkov detector in the world. It is placed at Kamioka Observatory (the Institute for Cosmic Ray Research, University of Tokyo) in Mozumi Mine (the Kamioka Mining and Smelting Company) located in Kamioka Town, Gifu Prefecture, Japan. By virtue of its location of 1000 m underground below the peak of Mt. Ikenoyama, which

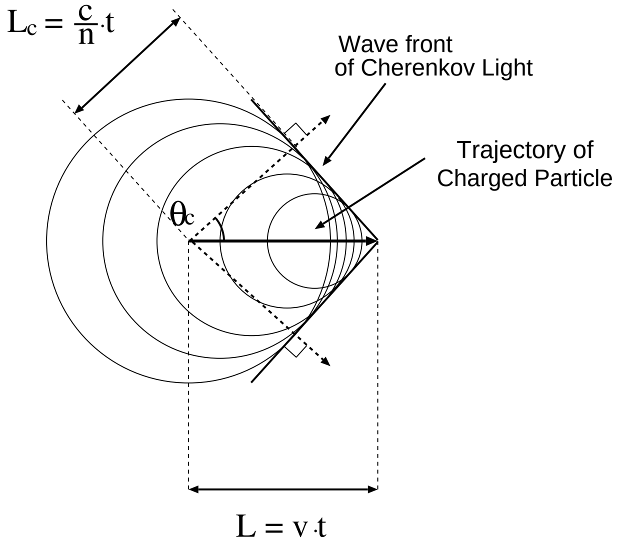

Figure 2.1: Cherenkov radiation. Dashed arrows show the direction of emitted light. It makes a cone with a half angle of θ_C.

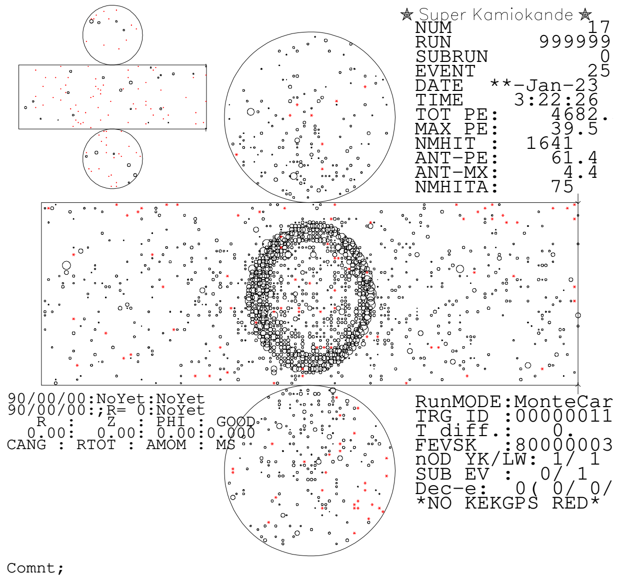

Figure 2.2: A typical simulated event in Super-Kamiokande. The size of small circles in the unrolled cylinder represents the amount of Cherenkov light detected in each photomultiplier tube. The ring image produced by a muon with its momentum of 700 MeV/c is clearly visible.

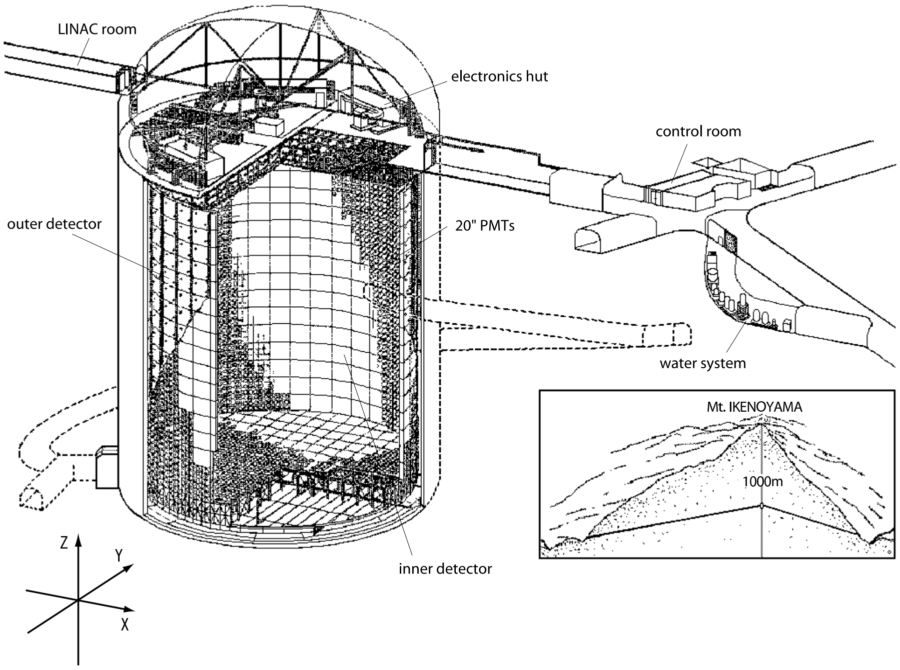

Figure 2.3: Super-Kamiokande detector and its location.

is equivalent to 2700 m of water, the cosmic ray muon flux at the detector site is reduced by about 5 orders of magnitude compared to that on the surface of the earth.

Figure 2.3 shows a schematic view of the detector and other facilities. A stainless steel cylindrical tank, 41 m in height and 39.3 m in diameter, holds 50 kt of highly purified water. The detector water is optically divided into three concentric cylindrical regions.

The inner region is 36.2 m in height and 33.8 m in diameter (32 kt) and monitored by 11146 inward facing 50 cm diameter photomultiplier tubes (PMTs), 7650 on the barrel wall and 1748 each on the top and the bottom. These PMTs are mounted on the supporting frame made of stainless steel at 70 cm regular intervals, as shown in Figure 2.4, and their photocathode coverage is about 40 % of the entire surface of the inner region. The rest of the surface is covered by opaque black polyethylene telephthalate sheets in order to improve the optical separation and suppress low energy events due to residual radioactivity occurring behind PMTs. This part of the detector is referred to as the inner detector (ID).

The thickness of the outer region is 2.0 m on top/bottom and 2.2 m on barrel. This region completely surrounds the inner detector and viewed by 1885 20 cm diameter PMTs facing outward toward the wall of the tank. The PMTs are distributed with 1275 on the barrel wall, 302 on the top and 308 on the bottom. This part of the detector is called the outer detector (OD). The OD photocathode coverage is only 1 %. To increase light collection, each OD PMT is equipped with a 60 cm $\times$ 60 cm $\times$ 1 cm wavelength shifter plate. Furthermore, the large spaces between PMTs are covered with DuPont Tyvec sheets, highly reflective white materials. The primary functions of the OD are to reject incoming cosmic ray muons and tag the outgoing charged particles.

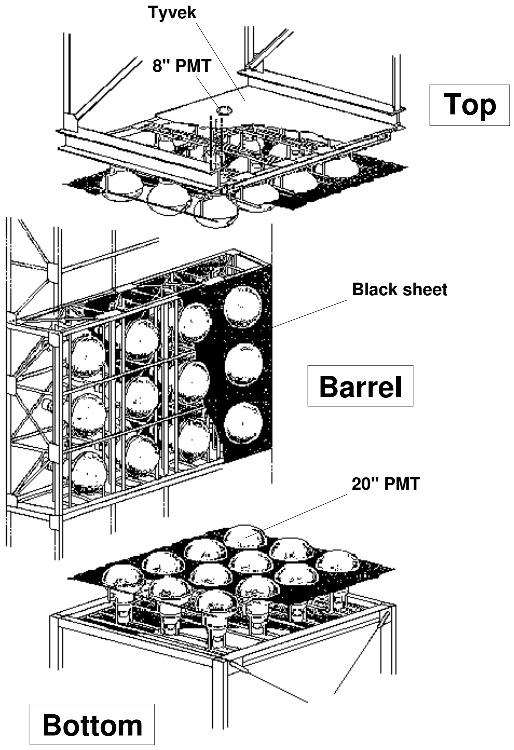

Figure 2.4: The supporting frame of PMTs.

The middle region, sometimes called the dead zone, is an uninstrumented cylindrical shell of 0.55 m thick between the ID and the OD. This region is occupied by supporting structures and cables of the ID and OD PMTs, as well as water. Along with the water in OD, the dead zone functions as a barrier to the γ-rays and neutrons from the tank surrounding rock.

The definition of the detector coordinate is described at the left bottom corner in Figure 2.3. The center of the ID is set to $(x, y, z) = (0, 0, 0)$.

2.2.1 Photomultiplier Tube

The photomultiplier tubes used in the ID are 50 cm diameter PMTs, Hamamatsu R3600, which were originally developed by Hamamatsu Photonics K.K. in cooperation with members of the Kamiokande experiment [28]. The PMTs used in Super-Kamiokande have some improvement over those used in Kamiokande [29]. Figure 2.5 shows a schematic view of the 50 cm PMT and Table 2.1 summarizes its specifications.

The photocathode area is coated by a bialkali (Sb-K-Cs) material on the inner surface of the hemispherical glass face. The reason for choosing the bialkali is that the wavelength dependence of its quantum efficiency matches the spectrum of Cherenkov light through pure water, as shown in Figure 2.6. To collect photoelectrons emitted from the large photocathode area, the

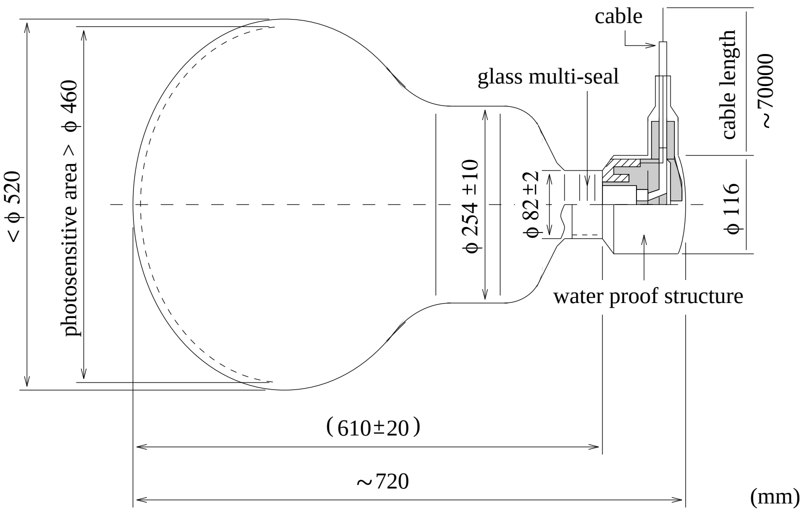

Figure 2.5: A schematic view of the 50 cm PMT.

Model	Hamamatsu R3600
Manufacturer	Hamamatsu Photonics K.K.
Shape	Hemispherical
Photocathode area	$2400\,\mathrm{cm}^2$
Photocathode material	Bialkali (Sb-K-Cs)
Window material	Pyrex glass ($4 \sim 5\,\mathrm{mm}$)
Pressure tolerance	$6\,\mathrm{kg/cm}^2$ water proof
Dynodes	Venetian blind type, 11 stages
Quantum efficiency	$20\,\%$ at $\lambda = 390\,\mathrm{nm}$
Gain	10^7 at $\sim 2000\,\mathrm{V}$
Dark current	$200\,\mathrm{nA}$ at 10^7 gain
Dark pulse rate	$3\,\mathrm{kHz}$ at 10^7 gain
Cathode non-uniformity	$< 10\,\%$
Anode non-uniformity	$< 40\,\%$
Transit time	$90\,\mathrm{nsec}$ at 10^7 gain
Transit time spread	$2.2\,\mathrm{nsec}$ ($1\,\sigma$) for 1 p.e. equivalent signals
Weight	$13\,\mathrm{kg}$

Table 2.1: Specifications of the 50 cm PMT.

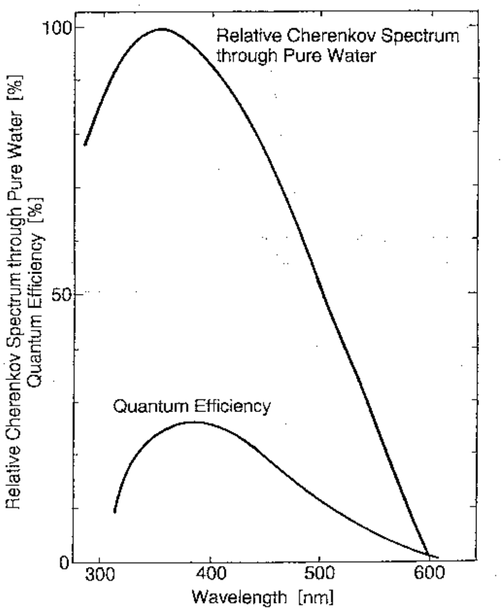

Figure 2.6: Quantum efficiency of the 50 cm PMT as a function of wavelength compared with the relative spectrum of Cherenkov light through pure water.

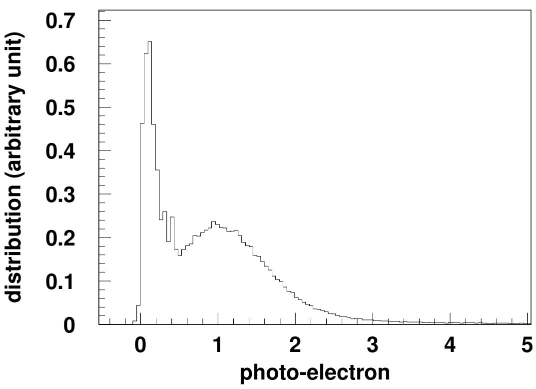

Figure 2.7: Single photoelectron pulse height distribution of the 50 cm PMT.

first dynode needs to be as large as possible. The Venetian blind type dynode is used for this PMT. For the Super-Kamiokande experiment, the dynode structure and the bleeder-chain are optimized to achieve good timing response and collection efficiency. The collection efficiency for photoelectrons at the first dynode is over 70 %. The single p.e. peak can be clearly seen in Figure 2.7. The timing resolution of the PMTs is about 2.2 nsec.

The geomagnetic field affects photoelectron trajectories in the PMTs. The 50 cm PMT requests the operation in the field below 100 mG for its uniform response, while the average geomagnetic field at the detector site is about 450 mG. To counteract this, 26 sets of horizontal and vertical Helmholtz coils are arranged around the tank. The residual magnetic field is kept about 50 mG in every position of the detector.

The 20 cm PMTs (Hamamatsu R1408) and the wavelength shifter plates in the OD were recycled from the IMB experiment [30]. The timing resolution of the OD PMTs is about 15 nsec with the wavelength shifter plate, versus 11 nsec without the plate. This resolution is considerably poorer than the 2 nsec resolution of the ID PMTs, but still enough for the functions of the OD as a calorimeter and veto counter.

2.2.2 Water Purification System

Figure 2.8 shows a schematic view of the water purification system for Super-Kamiokande. The source of water filled in the Super-Kamiokande detector is abundant clean spring water flowing in the mine. Water is mostly recirculated with a small amount of new water added in each cycle to replace losses. About 30 ton/hour of water is being processed at all times. Below is the brief explanation of each component.

- 1 μm Filter — removes small particles.
- Heat Exchanger — cools water to reduce PMT dark noise rate and suppress growth of bacteria. The water temperature in the detector is kept at 14 °C.
- Cartridge Polisher — eliminates heavy ions.
- Ultra-Violet Sterilizer — kills any bacteria.
- Radon-reduced Air Dissolve Tank — dissolves radon-reduced air into water to increase radon removal efficiency at the vacuum degasifier stage.
- Reverse Osmosis — removes additional particles.
- Vacuum Degasifier — removes dissolved gases in water such as the oxygen and radon.
- Ultra Filter — removes very small particles of the order of 10 nm.
- Membrane Degasifier — also removes radon dissolved in water.

The typical number of particles of size greater than 0.2 μm is reduced to 6 particles/cc after purification, versus 1000 particles/cc before purification.

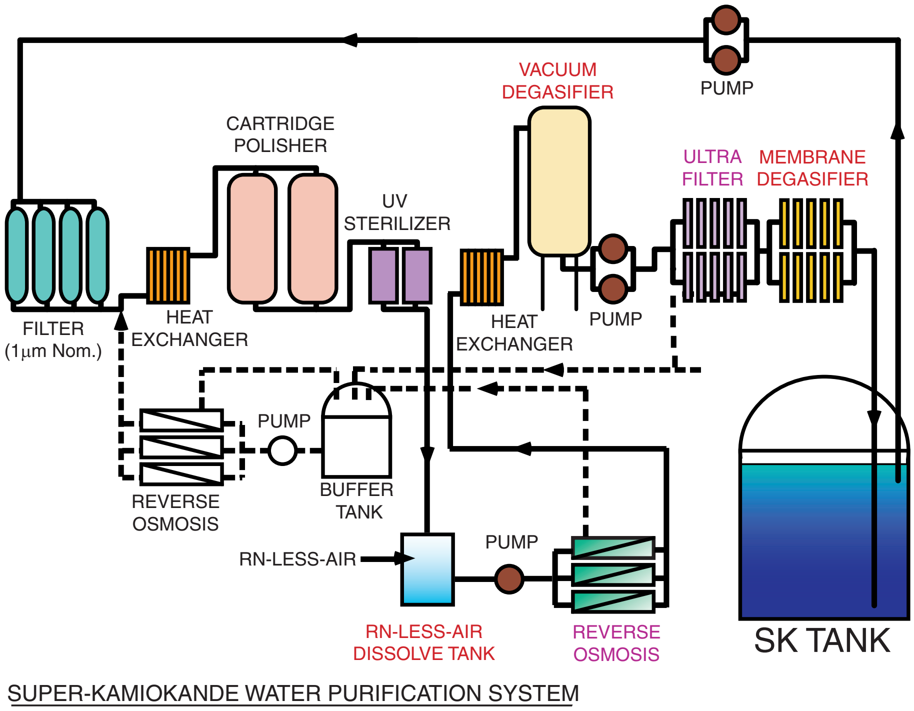

Figure 2.8: The water purification system for Super-Kamiokande.

2.2.3 Data Acquisition System

Inner Detector Electronics and Data Acquisition

Signals from the ID PMTs are processed by custom electronics modules called ATM (Analog Timing Module) [31, 32]. An ATM has functions of ADC/TDC and records charge and timing information of each PMT signal.

Figure 2.9 shows a block diagram of analog input part of the ATM. A PMT signal fed to an ATM is split into four signals by a current splitter. One branch is fed to a discriminator with the threshold level set at 0.25 p.e.. If the PMT signal exceeds the threshold level, a HITSUM signal is generated and sent to the global trigger module. In the mean time, the other branches of the split PMT signal lead to a charge to analog converter (QAC) with 400 nsec integrating window and a timing to analog converter (TAC). If the global trigger is issued, these information will be digitized and stored in internal FIFO memory of the ATM. If the global trigger does not arrive within 1300 nsec, the information will be cleared. There are two pairs of QAC and TAC for each PMT input so that two successive events, such as a muon and a following decay electron, can be processed. The ATM provides the charge dynamic range of 600 pC with 0.2 pC resolution and the time dynamic range of 1300 nsec with 0.4 nsec resolution.

Figure 2.10 shows a schematic view of the inner detector data acquisition system. An ATM board processes signals from 12 PMTs. There are 946 ATM boards in total. ADC/TDC data stored in ATM FIFO memory are read out by the online slave computers through VME memory modules called SMP (Super Memory Partner). 48 SMPs are used and each of them handles the

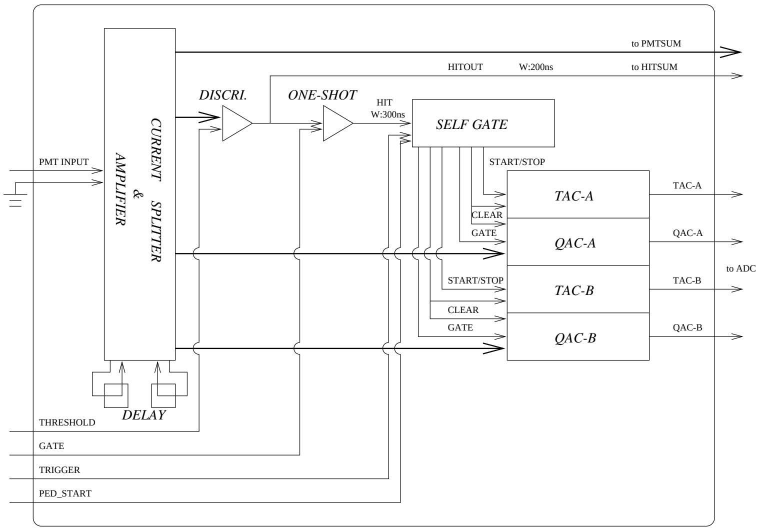

Figure 2.9: A block diagram of analog input part of the ATM.

data of 20 ATMs. The data collected by 8 slave computers are sent to the online host computer.

High voltage for each ID PMT is distributed by 48 CAEN SY527 multi-channel power supply systems. Each SY527 main frame accommodates 10 CAEN A933K high voltage supply boards which have 24 active distributor output channels. These systems are connected to a slow control computer via CAENET network so that high voltage can be controlled and monitored remotely.

Outer Detector Electronics and Data Acquisition

Signals from the OD PMTs are processed by different electronics [33]. A paddle card serves as a high voltage supply for 12 OD PMTs. It also picks off the PMT signals through a high voltage capacitor. Signals from 48 PMTs are collected by a QTC (Charge to Timing Converter) module. QTC modules emit an ECL logic pulse whose width is proportional to the amount of charge. The timing information is determined by the leading edge of the pulse. A QTC module also generates a HITSUM pulse to be sent to the global trigger module. If the global trigger is issued, the leading edge and width of an ECL pulse will be converted into charge and timing information by the LeCroy 1877 multi-hit TDC module. Converted information is stored in internal memory of the TDC module. The dynamic range of the TDC is set to 16 μsec with the resolution of 0.5 nsec. Each TDC modules has 96 input channels corresponding one channel per PMT. The stored data are read out by a online slave computer through VME memory modules called DPM (Dual Port Memory) and then transferred to the online host computer.

Trigger

Each ATM board generates a HITSUM signal of height proportional to the number of hit channels. These HITSUM signals are analog-summed over all the ATMs to produce the ID-HITSUM signal. There are three types of trigger signals derived from the ID-HITSUM. A schematic view of the trigger generation using the ID-HITSUM is shown in Figure 2.11. The

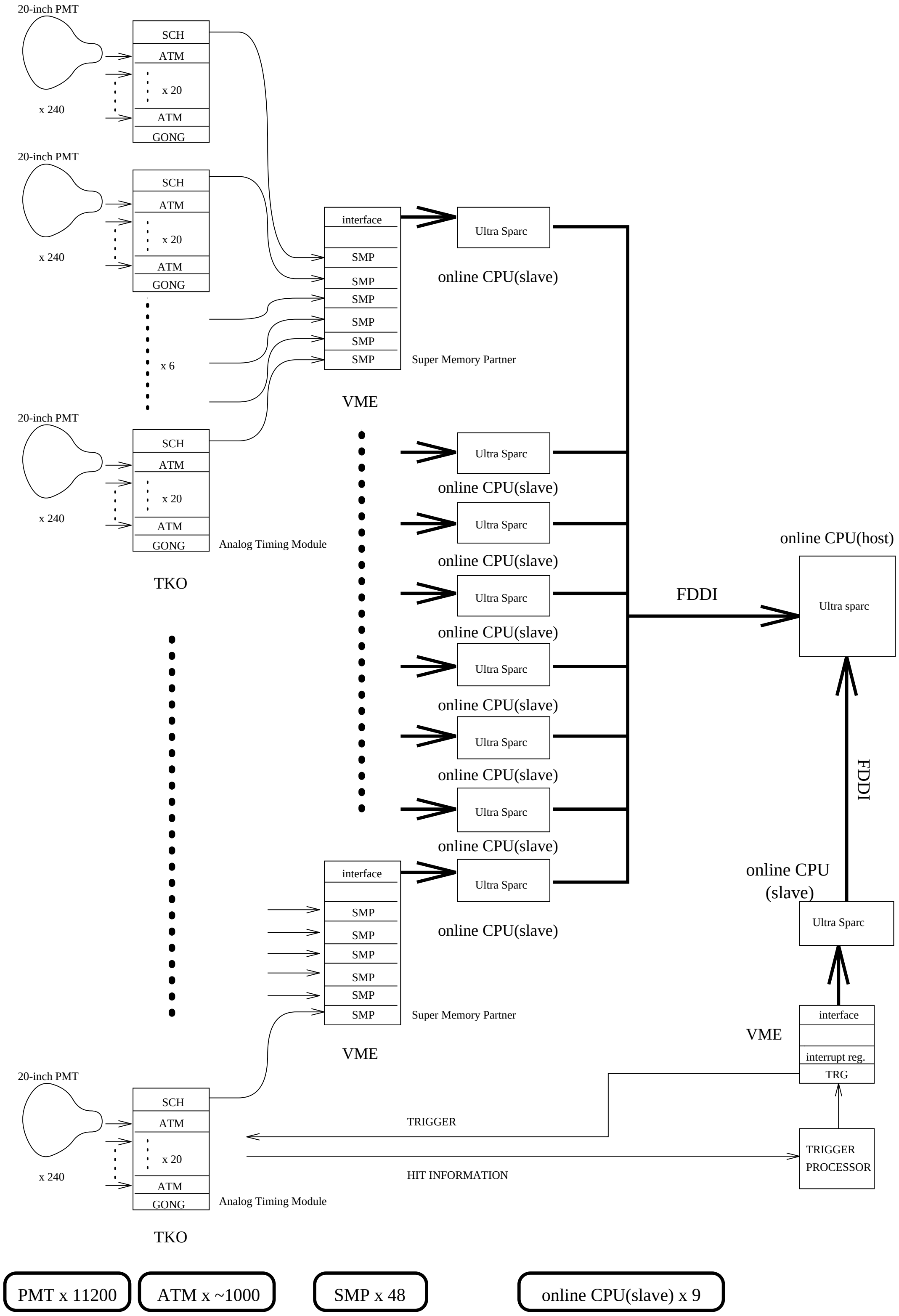

Figure 2.10: A schematic view of the inner detector data acquisition system.

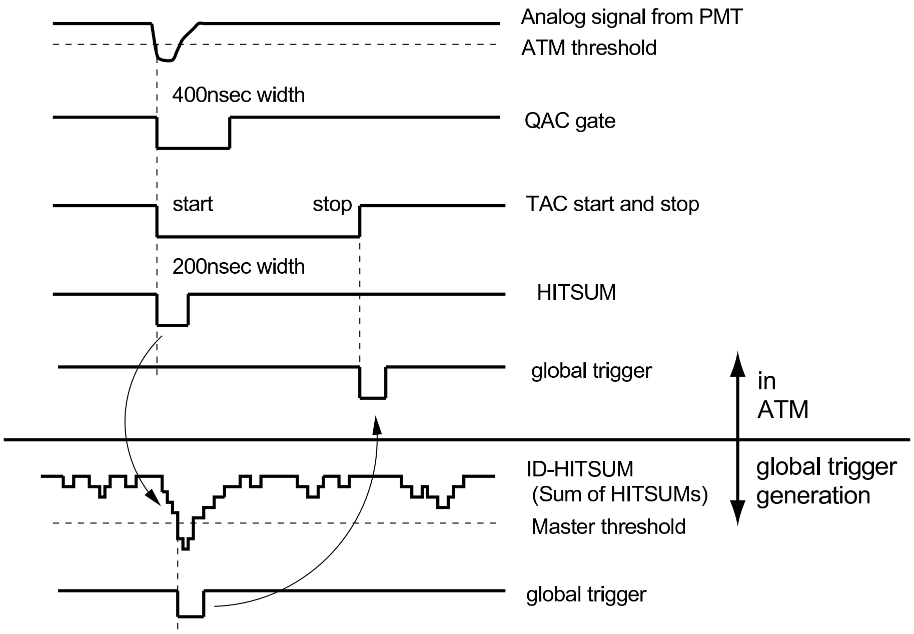

Figure 2.11: The trigger generation using the ID-HITSUM.

high energy (HE) trigger is generated when the ID-HITSUM crosses a threshold of -340 mV, which corresponds to 31 hits within a 200 nsec time window. The HE trigger rate is $5 \sim 6$ Hz. The thresholds for the low energy (LE) trigger and the super low energy (SLE) trigger are set -320 mV and -290 mV, respectively. The LE trigger corresponds to 29 hit ID PMTs within a 200 nsec time window. This is equivalent to the signal generated by 5.7 MeV electron. The LE trigger rate is about 11 Hz. The SLE trigger was implemented in May, 1997 in order to lower the analysis threshold of solar neutrino energy spectrum down to 4.6 MeV.

A similar procedure is used to generate the outer detector (OD) trigger. Each time a OD PMT signal exceeds a 0.25 p.e. threshold, the QTC module generates a HITSUM pulse with 200 nsec of width. These HITSUM signal from the QTCs are also summed up. The OD trigger requires 19 hits of the OD PMTs in a 200 nsec coincidence window.

These four types of trigger signals (HE, LE, SLE and OD) are fed into the VME hardware trigger module called TRG. If at least one type of the trigger signal is issued, the TRG module generates a global trigger signal and a 16-bit event number, which are distributed to all the frontend electronics. In the mean time, the TRG records the issued trigger type, the trigger time, and the event number. The multiple coincidence of the trigger types is allowed. The trigger data stored in the TRG are read by a separate online computer and transferred to the online host computer, to be merged with the ATM data.

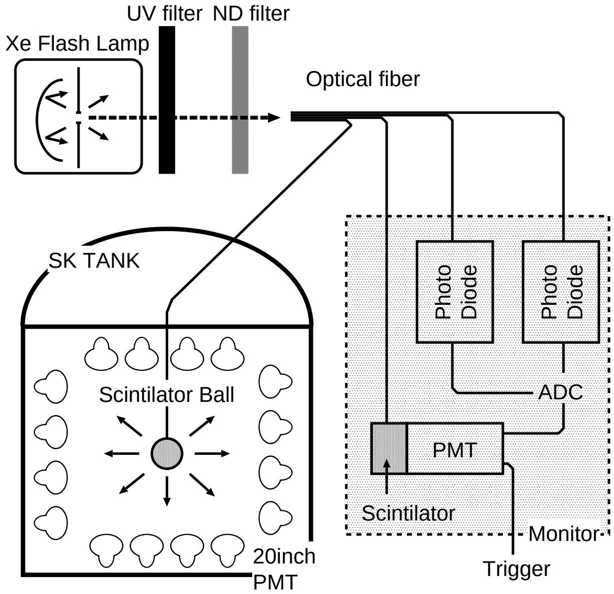

Figure 2.12: A schematic view of the relative gain measurement system using a Xe lamp.

2.3 Calibration

2.3.1 Relative Gain Calibration

The gain of all PMTs must be adjusted for the uniform response of the detector. At the beginning of the experiment, the high voltage of each ID PMT was set to provide approximately equal gain for all the ID PMTs.

The relative gain is measured by the system shown in Figure 2.12. A Xe flash lamp is used as a light source. Light generated by a Xe lamp is passed through an ultraviolet (UV) filter and split into four signals. One branch is injected into a scintillator ball placed in the detector tank via an optical fiber. The other branches are used for monitoring the Xe light intensity and also generating an calibration event trigger. The scintillator ball is made of acrylic resin mixed with BBOT wavelength shifter and MgO powder diffuser. BBOT absorbs UV light and emits light with a similar spectrum to that of Cherenkov light through pure water.

The observed charge of each PMT is corrected (corrected-Q) for the light attenuation, the light acceptance of the PMT, and the uniformity of the scintillator ball. It is further normalized by the pulse height of Xe light monitors. The high voltage value for each PMT is determined so that the corrected-Q of each PMT is approximately the same as those of all others. This measurement is done for various height of the scintillator ball and high voltage settings.

Figure 2.13 shows the relative gain distribution of all the ID PMTs after adjusting high voltage values. The horizontal axis shows the corrected-Q normalized by its mean. The relative gain spread is estimated to be about 7 %, and the remaining gain difference is corrected in software. After the initial gain adjustment, log term stability of the PMT gain has been monitored using the same system.

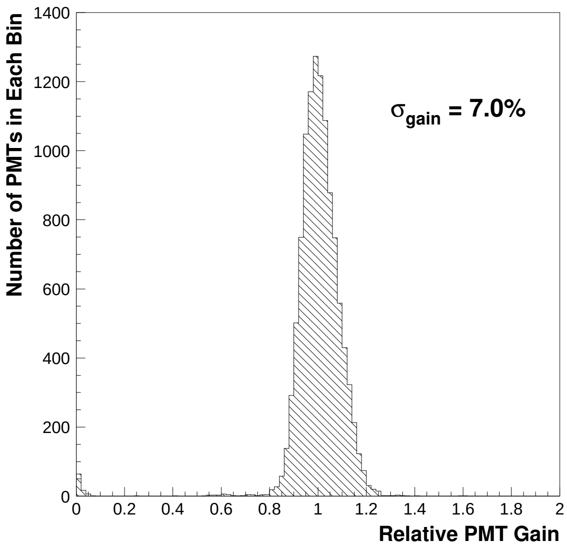

Figure 2.13: The relative gain distribution of all the ID PMTs, measured in 1996.

2.3.2 Timing Calibration

The relative timing of PMT hits is important for the vertex position reconstruction. Not only does it depend on the length of the PMT signal cable, but it is affected by the observed charge as well because of the discriminator slewing effect.

The relative timing is measured by the system shown in Figure 2.14. We use a N_2 laser which can emit intense light of wavelength 337 nm for a short time (~ 3 nsec) with a small jitter ($\sim \pm 0.5$ nsec). A dye laser module is used for converting the light wavelength to 384 nm, which is near the lower edge of the sensitive region of a PMT. The light is guided by an optical fiber into a diffuser ball placed in the detector tank. The diffuser ball is a 8 cm diameter glass sphere which contains a TiO_2 diffuser tip at the center and is filled with LUDOX, silica gel made of 20 nm glass fragments.

The measurement is done changing the light intensity by a variable attenuation filter. Figure 2.15 shows a typical scatter plot of the measured timing and charge for a 50 cm PMT, which is called a TQ-map. The dots represent the data. The circles represent the averaged timing for each charge bin with the error bars being their resolutions. Each PMT has its own TQ-map. In physics analyses, the timing information of each PMT is corrected using its TQ-map.

2.3.3 Water Transparency Measurement I

A direct measurement of the water attenuation length is done with a device consisting of a titanium-sapphire laser, a diffuser ball and a CCD camera [34]. Figure 2.16 shows the measurement system. The tunable titanium-sapphire laser is pumped up with an Nd:YAG laser, which can provide output energies of 2$\sim$3 mJ/pulse at a wavelength of 420 nm. The attenuation

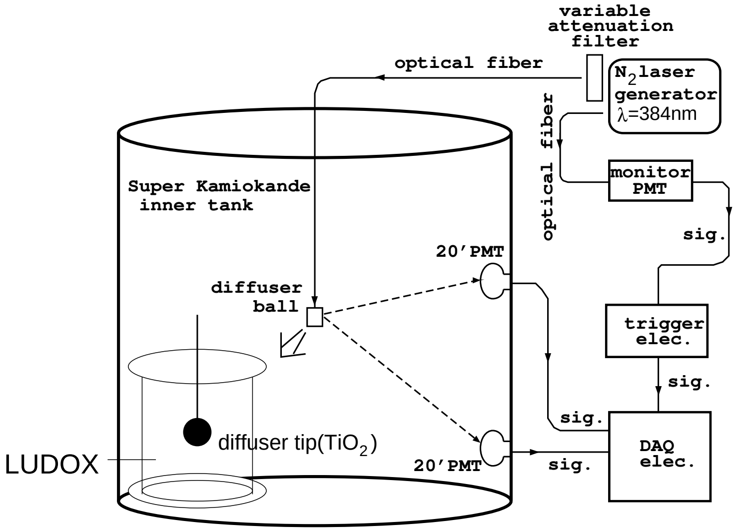

Figure 2.14: A schematic view of the timing measurement system using a laser.

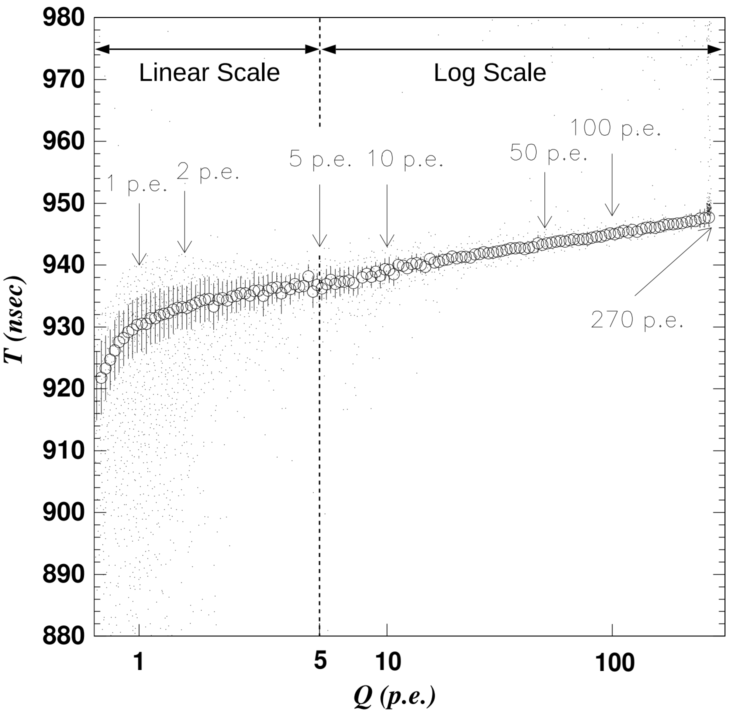

Figure 2.15: TQ-map, a measured two-dimensional plot of timing vs. charge distribution.

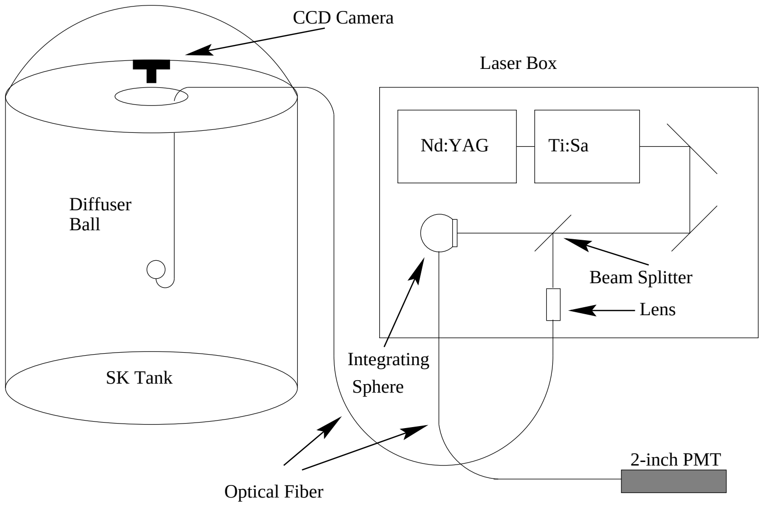

Figure 2.16: A schematic view of the water attenuation length measurement system.

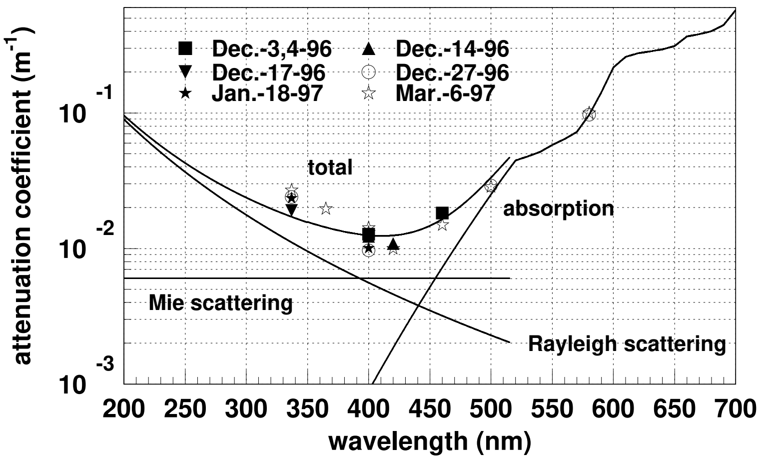

Figure 2.17: The wavelength dependence of attenuation coefficients ($L_{\rm atten}^{-1}$) by the measurement (points), compared with our model in the detector simulation (lines, see Section 3.3).

length for the various wavelength between 300 nm and 600 nm can be measured using a second harmonic generator.

To measure the attenuation length, the diffuser ball is lowered into the detector water and illuminated with the laser through an optical fiber. Then the image of the ball is taken by a CCD camera set on the top of the tank. This measurement is made at various depth of the ball and the attenuation length is estimated. The wavelength dependence of measured attenuation coefficients (L_{atten}^{-1}) is shown in Figure 2.17. The attenuation length takes a maximum of 100 m around 400 nm wavelength.

2.3.4 Water Transparency Measurement II

The light attenuation length in water is also measured by using Cherenkov light from cosmic ray muons passing vertically through the detector. The energy deposits by these energetic muons are almost constant ($\sim 2\,\mathrm{MeV/cm}$) and independent of particle energy, so we can use them as a constant light source. This method gives us a continuous monitoring of the attenuation length without disturbing normal data taking.

We select through-going muons which enter the inner tank through a 15.9 m radius circular region on the top surface with its center being on the tank axis and also exit through a 15.9 m radius circular region on the bottom surface. We also require the horizontal distance between the entry point and the exit point to be less than 5 m.

If we assume the light arriving at PMTs is not scattered, the charge Q observed by a PMT is calculated by :

$$Q = Q_0 \cdot \frac{f(\theta)}{l} \cdot \exp(-\frac{l}{L}) \tag{2.4}$$

where l is the Cherenkov photon path length, L is the attenuation length, Q_0 is a constant, and $f(\theta)$ is the PMT acceptance as a function of the photon incident angle θ on the PMT. Figure 2.18 shows the measured $Q{\cdot}l/f(\theta)$ as a function of the photon path length l in a typical run. The attenuation length is estimated to be about 95 m from the best fit result by a exponential function.

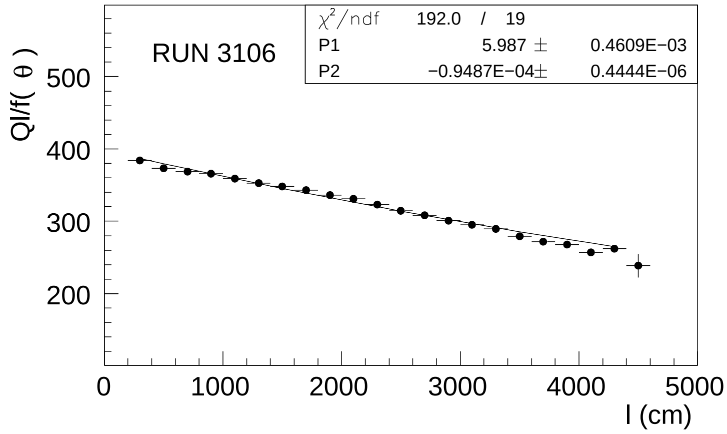

Figure 2.18: Effective observed charge for through-going muons as a function of the photon path length.

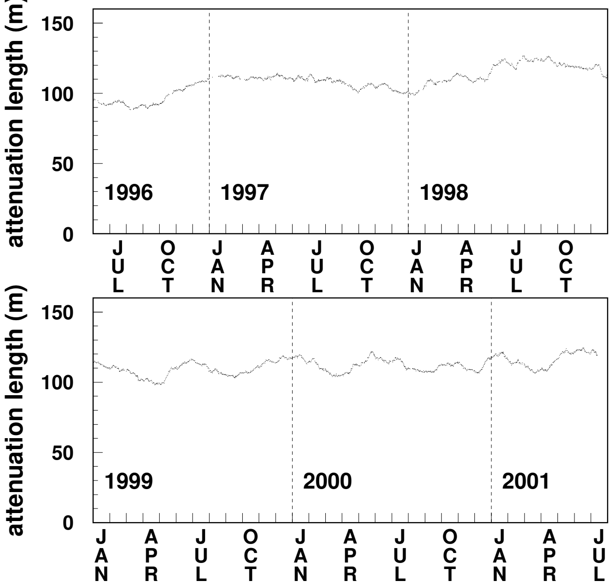

Figure 2.19: The time variation of the water attenuation length.

Since the data sample for this measurement is accumulated automatically while the normal data are taken, it is possible to continuously monitor the attenuation length as a function of time. Figure 2.19 shows the time variation of the water attenuation length. This time variation is corrected in reconstruction processes for the normal data (see Section 5.5).

2.3.5 Light Scattering Measurement

The light attenuation length in water can be described as $L = (\alpha_{scat} + \alpha_{abs})^{-1}$, where α_{scat} is the scattering coefficient and α_{abs} is the absorption coefficient. To measure the scattering and absorption coefficients separately, we use combinations of dye and N_2 lasers as light sources [35]. Figure 2.20 shows a schematic view of the scattering and absorption parameter measurement. Each laser fires every 6 seconds during normal data taking, and the light beam is injected vertically into the inner tank via an optical fiber. A typical event by the laser light is also shown in Figure 2.20. PMT hits clustered at the bottom of the tank are due to direct (unscattered) photons. The remaining PMT hits on the barrel wall and the top are due to photons scattered in the detector water and/or reflected on surfaces of bottom PMTs. The total charge in the cluster of bottom PMT hits is used for the normalization of the light intensity.

Figure 2.21 shows PMT hit time distributions of 337 nm-laser events in each detector region . The earlier peak in each distribution is made by scattered photons, and the later peak represents photons reflected by PMTs or black sheets. For the MC, the total number of scattered photons is used to adjust the absolute factor of the scattering coefficient (α_{scat}), and the shape of the hit time distribution is used to adjust the absolute factor of the absorption coefficient (α_{abs}). Then the light attenuation length is calculated using the measured scattering and absorption coefficients. The light attenuation length and its time variation obtained in this method are reasonably consistent with measurements described in Section 2.3.3 and Section 2.3.4 [35].

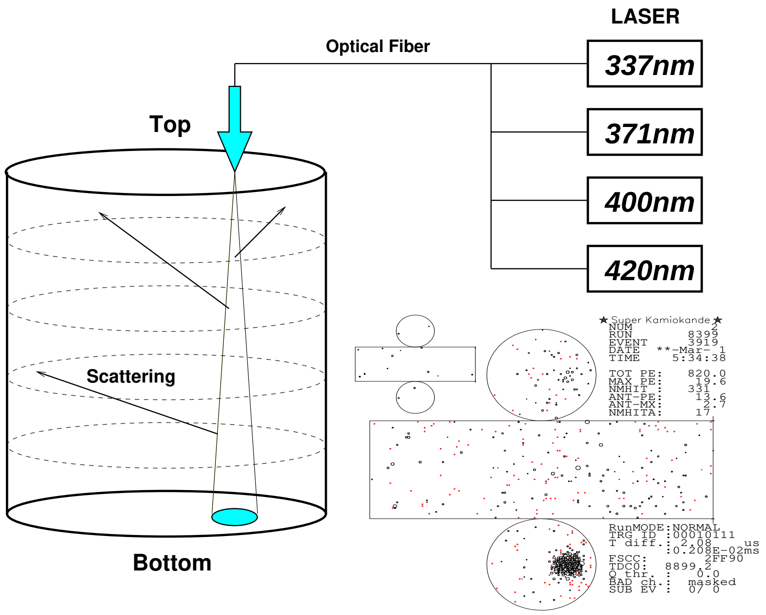

Figure 2.20: A schematic view of the scattering and absorption parameter measurement using laser systems, and a typical event.

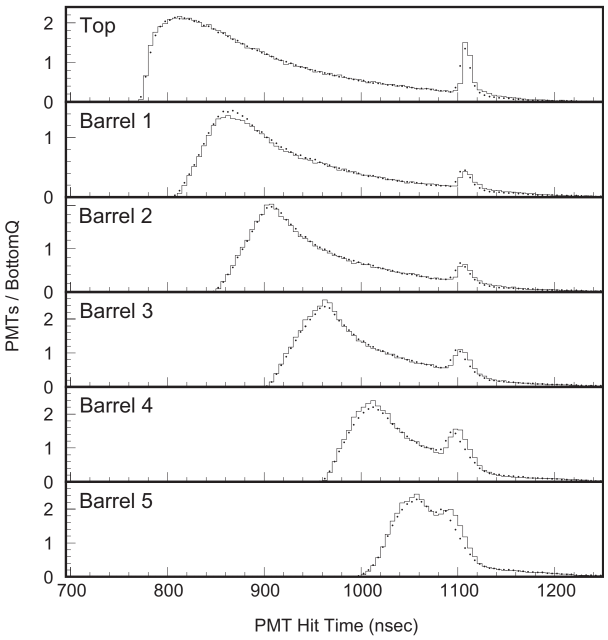

Figure 2.21: PMT hit time distributions of 337 nm-laser events in each detector region for the data (dots) and the MC which is tuned using the scattering and absorption parameters (histograms).

2.3.6 Absolute Energy Calibration

Super-Kamiokande has several methods to measure the absolute energy scale.

Electrons from Muon Decay

Electrons from the decay of cosmic ray muons stopped in the inner tank are used for checking the scale of relatively low energy ($\sim 50\,\mathrm{MeV}/c$). The selection criteria for decay electron events are :

(a) the number of hit ID PMTs in a 50 nsec time window is greater than 40

(b) time interval from a stopping muon event is in the range of $1.5\,\mu$sec $\sim 8.0\,\mu$sec

(c) the event vertex is in the fiducial volume

The positron energy spectrum from μ^+ decay is precisely calculated by pure V-A theory as :

$$\frac{d\Gamma}{dE_e} = \frac{G_F^2}{12\pi^2} m_\mu^2 E_e^2 (3 - \frac{4E_e}{m_\mu}) \ , \quad E_e \leq \frac{m_\mu}{2} \tag{2.5}$$

where E_e, m_μ and G_F are positron energy, muon mass and Fermi coupling constant, respectively. In case of μ^- decay, however, the energy spectrum of outgoing electrons are distorted because most of μ^- are trapped in a ^{16}O orbit [36]. This effect is taken into account for our simulation. In addition, we use the measured μ^+/μ^- ratio in our simulation [37]. Figure 2.22 shows the reconstructed momentum distribution for decay electron events. The difference in the mean values between the data and the MC is found to be about 2.2 %.

Neutrino-Induced π^0 Events

We can use the invariant mass of single-π^0 events produced by atmospheric neutrino interactions for checking the energy scale over several hundred MeV/c. Since π^0 events are discussed in detail later in this thesis, only the result is shown here. Figure 2.23 shows the invariant mass distribution of π^0 events. The difference in the fitted mass peaks between the data and the MC is about 3.0 %.

Cosmic Ray Stopping Muons - I

Reconstructing the entrance point of a stopping muon event and the vertex position of a subsequent decay electron event, we can know the track length of the stopping muon. Since the range of a muon is determined by its momentum, it can be used as an independent test of the momenta derived from the observed charge (For momentum determination, see Section 5.5). Stopping muon events are selected by the following criteria :

(a) the total number of p.e.s of the ID PMTs > 200 p.e.

(b) one cluster of hit OD PMTs

(c) an entrance point is on the top wall and the muon direction is downward, $\cos\theta > 0.94$

(d) one decay electron event with a time difference greater than $0.8\,\mu$sec

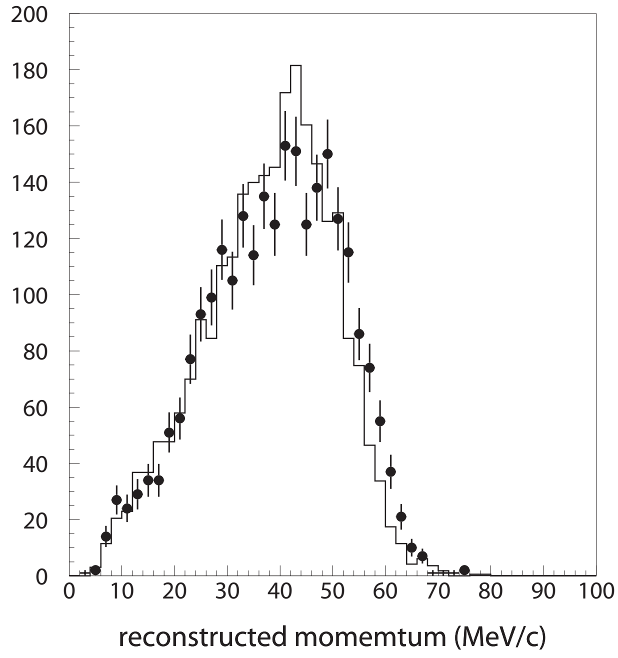

Figure 2.22: The reconstructed momentum distribution for decay electron events. The dots show the observed data and the histogram shows our Monte Carlo expectation.

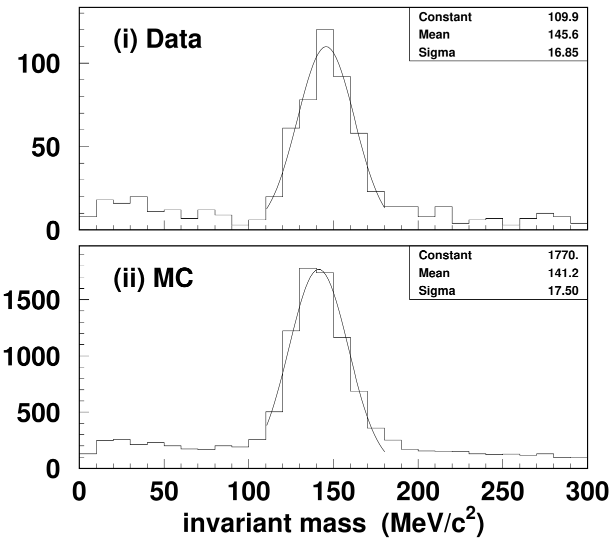

Figure 2.23: The invariant mass distribution of neutrino-induced π^0 events for (i) the data and (ii) the atmospheric neutrino Monte Carlo. The peaks are fitted by Gaussian distributions.

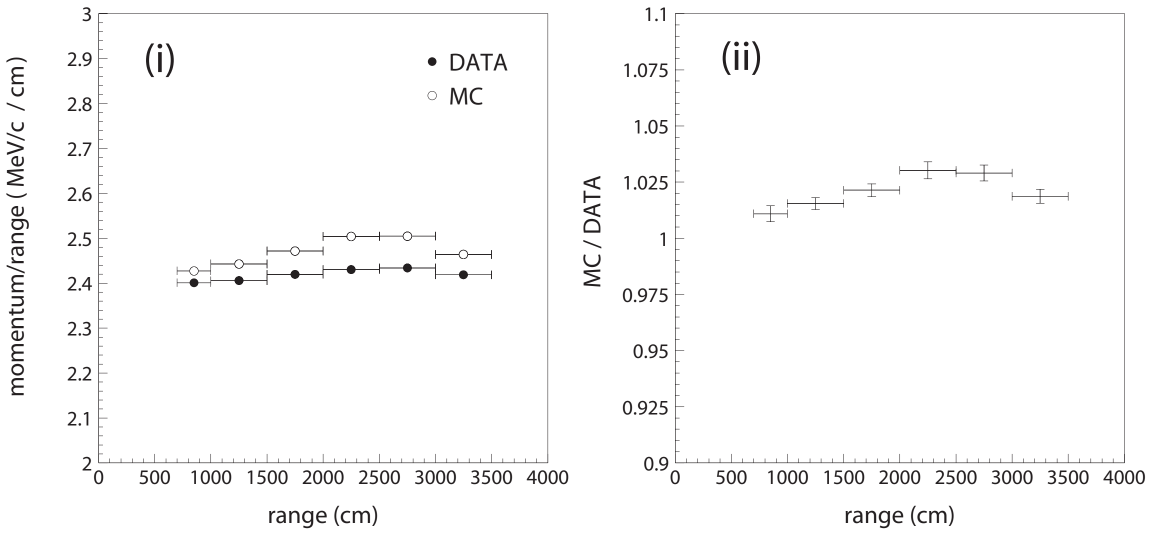

Figure 2.24: The momentum/range of stopping muon events (i) for the data and the MC, and (ii) its ratio between the data and the MC.

(e) the reconstructed muon range is greater than 7 m

Figure 2.24 shows the momentum/range ratio of stopping muon events for the data and the MC. Here, the MC events are generated using the reconstructed vertices and momentum vectors of the observed muon events. The difference of the momentum/range ratio between the data and the MC is within about 3.0 %.

Cosmic Ray Stopping Muons - II

The opening angle of the Cherenkov cone can be another source to check the energy scale given by cosmic ray stopping muons. Since the Cherenkov angle is a function of the momentum as follows, the reconstructed angle gives an independent estimation of the momentum :

$$\cos\theta_C = \frac{1}{n\beta} = \frac{1}{n}\sqrt{1+\frac{m^2}{p^2}} \tag{2.6}$$

This method is effective only for muons with relatively low energy ($< 400\,\mathrm{MeV}/c$), because $|d\theta/dp|$ is not large in the higher energy range. Stopping muon events for this analysis are selected by the following criteria :

(a) the total number of p.e.s of the ID PMTs is in the range of 200 p.e. $\sim$ 1500 p.e.

(b) one cluster of hit OD PMTs

(c) an entrance point is on the top wall, and its distance from the tank axis is less than 14.9 m

(d) the muon direction is downward, $\cos\theta > 0.9$

(e) one decay electron event with a time difference greater than 0.8 μsec

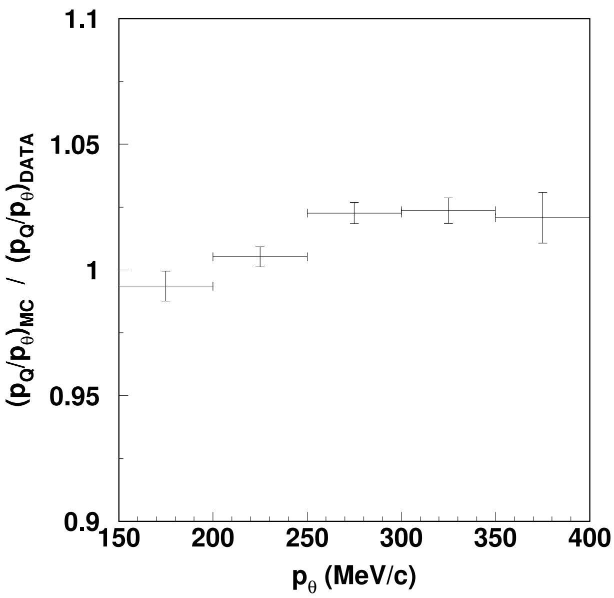

Figure 2.25: The p_Q/p_θ double ratio between the data and the MC, where p_θ is the muon momentum calculated from the reconstructed opening angle, and p_Q is the reconstructed momentum based on the observed charge (normal way).

Figure 2.25, p_θ shows the p_Q/p_θ double ratio between the data and the MC, where p_θ is the muon momentum calculated from the reconstructed opening angle, and p_Q is the reconstructed momentum based on the observed charge (normal way). The difference between the data and the MC is less than 3 %.

The absolute energy scale are checked using several sources. As summarized in Figure 2.26, the uncertainty of the energy scale is estimated to be within ± 3 % in the momentum range from $\sim 50\,\mathrm{MeV}/c$ to several GeV/c.

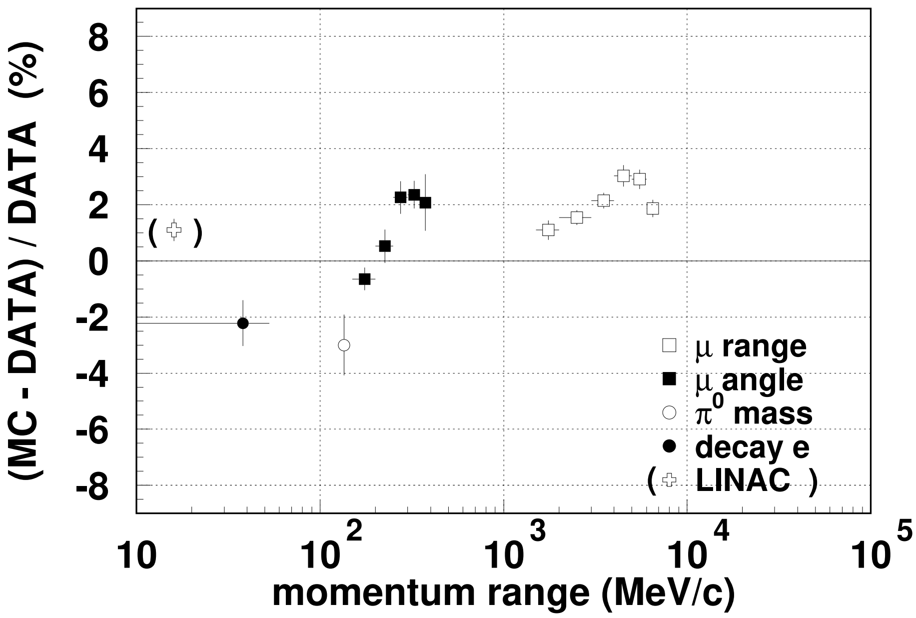

Figure 2.26: The summary of the absolute energy scale check. The horizontal axis shows the momentum range of each source.

Chapter 3

Simulation

3.1 Atmospheric Neutrino Flux

Among the several detailed calculation of the atmospheric neutrino flux, we adopt the neutrino flux calculated by Honda *et al.* (Honda flux). The flux calculated by Agrawal *et al.* (Bartol flux) is also used to estimate the systematic uncertainty on flux calculation.

The Honda calculation employs a full Monte Carlo method employed for low energy neutrinos (30 MeV $\sim$ 3 GeV), while a superposition approximation and a hybrid method are used for high energy neutrinos (1 GeV $\sim$ 3000 GeV).

In the case of low energy neutrinos, the fluxes of primary cosmic ray components are relatively well known. However, low energy cosmic ray fluxes are modulated by solar activity, and are affected by the geomagnetic field through the rigidity (= momentum/charge) cutoff. The proton-nucleus interaction is also important. In the Honda calculation, the nuclei and the primary energies of cosmic rays are sampled according to their energy spectrum and rigidity cutoff, and are put into the propagation program which simulates the interaction of particles in the atmosphere.

In the case of high energy neutrinos, parent high energy cosmic rays are not affected by solar activity or by geomagnetic field. However there are few measurements of the cosmic ray chemical composition at these energies, especially above 1 TeV. The superposition approximation used in the Honda calculation for high energy neutrino flux treats a nucleus as a bundle of independent nucleons, and consider the event caused by the nucleus as the sum of independent events caused by these nucleons. The hybrid method which is also used in the Honda calculation is calculation based on the ν-yield function for nucleons, ${\eta_\nu}^N(E, E_\nu, \theta)$, which denotes the number of neutrinos in the energy region from E_ν to $E_\nu + dE_\nu$, created by a nucleon with energy of E incident from zenith angle θ. The ${\eta_\nu}^N$ is calculated by a Monte Carlo method. The calculated fluxes below 10 GeV smoothly connect to the low energy calculation at around 3 GeV. This means that the systematic difference between the calculations for high energy and low energy atmospheric neutrino fluxes is very small.

The calculated absolute flux and flux ratios of atmospheric neutrinos are already shown in Figure 1.1 and in Figure 1.2, respectively. The systematic uncertainty on the absolute flux is estimated to be about 20 % in the energy region from 0.1 GeV to 10 GeV, while the uncertainty on the flux ratios are smaller than 5 %.

3.2 Neutrino Interaction

Atmospheric neutrinos interact with nucleons and electrons in water of the detector. In our atmospheric neutrino Monte Carlo simulation, the following charged current (CC) interactions and neutral current (NC) interactions are considered :

CC coherent pion production	$\nu + {}^{16}\mathrm{O} \rightarrow\ l^{\pm} + {}^{16}\mathrm{O} + \pi^{\mp}$
NC coherent pion production	$\nu + {}^{16}\mathrm{O} \rightarrow\ \nu + {}^{16}\mathrm{O} + \pi^{0}$
CC quasi-elastic scattering	$\nu + N \rightarrow\ l + N'$
NC elastic scattering	$\nu + N \rightarrow\ \nu + N$
CC single-meson production	$\nu + N \rightarrow\ l + N' + \mathrm{meson}$
NC single-meson production	$\nu + N \rightarrow\ \nu + N' + \mathrm{meson}$
CC multi-pion production	$\nu + N \rightarrow\ l + N' + m\pi\quad (m \geq 1)$
NC multi-pion production	$\nu + N \rightarrow\ \nu + N' + m\pi\quad (m \geq 1)$

where N and N' are nucleons, l is a charged lepton and m is the multiplicity of pions. The cross section calculation used in our simulation is described in the following sections for each interaction.

Since the cross section of the neutrino-electron elastic scattering is about 10^3 times smaller than that of the neutrino-nucleon interactions at the ~1 GeV neutrino energy region, we neglect this interaction in our simulation.

3.2.1 Coherent Pion Productions

Coherent pion production is a neutrino interaction with a nucleus, in which the nucleus remains intact without any change of its charge or isospin. Since the transferred momentum to the nucleus is very little, the angular distributions of outgoing leptons and pions are forward peaked sharply.

We use the differential cross section calculated by Rein & Sehgal [38] :

$$\frac{d\sigma}{dxdyd|t|} = \frac{G_F^2 M_N}{2\pi^2} f_\pi^2 A^2 E_\nu (1-y) \frac{1}{16\pi} (\sigma_{total}^{\pi N})^2 (1+r^2) (\frac{M_A^2}{M_A^2 + Q^2})^2 e^{-b|t|} F_{abs} \tag{3.1}$$

where $x = Q^2/(2M_N(E_\nu - E_l))$ and $y = (E_\nu - E_l)/E_\nu$ are Bjorken parameters, t is the square of the 4-momentum transfer to the nucleus, Q is the 4-momentum transfer of the lepton, G_F is the Fermi coupling constant, M_N is the nucleon mass, M_A is the axial-vector mass, A is the atomic number ($=16$ for oxygen), f_π is the pion decay constant ($=0.93\,m_\pi$), $\sigma_{total}^{\pi N}$ is the averaged cross section of pion-nucleon scatterings and b is in the order of the nucleus traverse dimensions ($=80\,\mathrm{GeV}^{-2}$ for oxygen). r is the ratio $Re(f_{\pi N}(0))/Im(f_{\pi N}(0))$, where $f_{\pi N}$ is the pion-nucleon scattering amplitude. F_{abs} is the factor to account for the pion absorption in the nucleus. Fig. 3.1 shows the cross sections for CC and NC coherent pion productions used in our Monte Carlo.

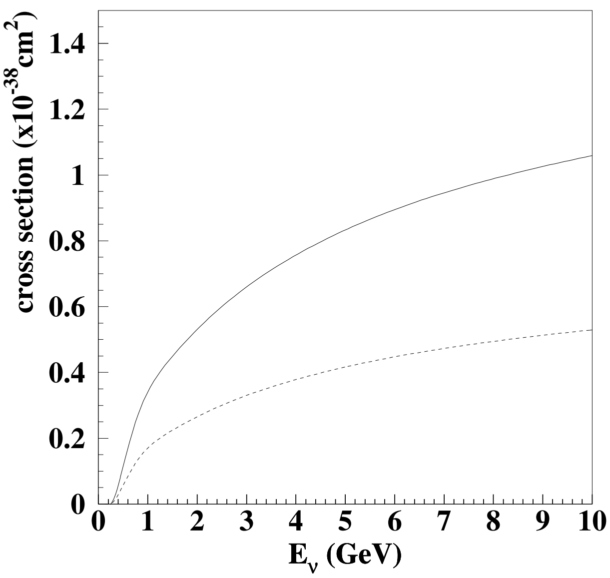

Figure 3.1: The cross sections of coherent pion productions off the ^{16}O nucleus used in our Monte Carlo. The solid line is for CC interactions while the dashed line is for NC interactions.

3.2.2 Quasi-Elastic Scatterings and Elastic Scatterings

CC quasi-elastic scatterings make a dominant contribution to interactions of neutrinos with energies below 1 GeV.

The cross section of this interaction is calculated based on the standard V-A (Vector and Axial vector) theory. The hadronic weak current is expressed as [39] :

$$\langle N'|J^{\mathrm{hadron}}|N\rangle = \cos\theta_c \bar{u}(N')\left(\gamma_\lambda F_V^1(q^2) + \frac{i\sigma_{\lambda\nu}q^\nu\xi F_V^2(q^2)}{2M_N} + \gamma_\lambda\gamma_5 F_A(q^2)\right)u(N) \tag{3.2}$$

where q is the 4-momentum transfer of the lepton, $F_V^1(q^2)$ and $F_V^2(q^2)$ are vector form factors, $F_A(q^2)$ is an axial vector form factor, θ_c is the Cabibbo angle and $\xi \equiv \mu_p - \mu_n$ using the anomalous magnetic dipole moments of protons and neutrons. The vector form factors are represented as following :

$$F_V^1(q^2) = \left(1 - \frac{q^2}{4M_N^2}\right)^{-1}\left[G_E(q^2) - \frac{q^2}{4M_N^2}G_M(q^2)\right] \tag{3.3}$$

$$\xi F_V^2(q^2) = \left(1 - \frac{q^2}{4M_N^2}\right)^{-1}\left[G_E(q^2) - G_M(q^2)\right] \tag{3.4}$$

$$G_E(q^2) = (1+\xi)^{-1}G_M(q^2) = \left(1 - \frac{q^2}{M_V^2}\right)^{-2} \tag{3.5}$$

The vector mass, M_V, is determined by $e-p$ scattering experiments and set to be 0.84 GeV/c^2

in our simulation. The axial vector form factor is approximated as a dipole :

$$F_A(q^2) = -1.23 \left(1 - \frac{q^2}{M_A^2}\right)^{-2} \tag{3.6}$$

using the axial vector mass, M_A. Some experiments suggest $0.9\ \mathrm{GeV}/c^2 < M_A < 1.1\ \mathrm{GeV}/c^2$ [40], and we adopt $M_A = 1.01\ \mathrm{GeV}/c^2$.

Finally, the differential cross section is expressed as :

$$\frac{d\sigma^{\nu(\bar{\nu})}}{dq^2} = \frac{M_N^2 G_F^2 \cos^2\theta_c}{8\pi E_\nu^2}\left[A(q^2) \mp B(q^2)\frac{s-u}{M_N^2} + C(q^2)\frac{(s-u)^2}{M_N^4}\right] \tag{3.7}$$

where s and u are Mandelstam variables and E_ν is the neutrino energy. Factors A, B and C are written as :

$$\begin{aligned} A(q^2) &= \frac{m^2 - q^2}{4M^2}\left[\left(4 - \frac{q^2}{M^2}\right)|F_A|^2 - \left(4 + \frac{q^2}{M^2}\right)|F_V^1|^2\right. \\ &\left. - \frac{q^2}{M^2}|\xi F_V^2|^2\left(1 + \frac{q^2}{4M^2}\right) - \frac{4q^2 F_V^1 \xi F_V^2}{M^2} - \frac{m^2}{M^2}\left((F_V^1 + \xi F_V^2)^2 + |F_A|^2\right)\right] && (3.8) \\ B(q^2) &= \frac{q^2}{M^2}\left(F_A(F_V^1 + \xi F_V^2)\right) && (3.9) \\ C(q^2) &= \frac{1}{4}\left(|F_A|^2 + |F_V^1|^2 - \frac{q^2}{4M^2}|\xi F_V^2|^2\right) && (3.10) \end{aligned}$$

Figure 3.2 shows our total cross sections of (a) $\nu_\mu + n \to \mu^- + p$ and (b) $\overline{\nu}_\mu + p \to \mu^+ + n$, compared with data from various experiments.

NC elastic scattering cross sections are derived from the following relations [46, 47] :

$$\begin{aligned} \sigma(\nu p \to \nu p) &= 0.153 \times \sigma(\nu n \to e^- p) && (3.11) \\ \sigma(\bar{\nu} p \to \bar{\nu} p) &= 0.218 \times \sigma(\bar{\nu} p \to e^+ n) && (3.12) \\ \sigma(\nu n \to \nu n) &= 1.5 \times \sigma(\nu p \to \nu p) && (3.13) \\ \sigma(\bar{\nu} n \to \bar{\nu} n) &= 1.0 \times \sigma(\bar{\nu} p \to \bar{\nu} p) && (3.14) \end{aligned}$$

In case of the scattering with a nucleon bound in a ^{16}O nucleus, Fermi motion and Pauli blocking need to be considered. We use the Fermi momentum distribution estimated from the electron scattering experiment on ^{12}C [48]. The Pauli blocking effect is taken requiring the outgoing nucleon momentum to be larger than the Fermi surface momentum of a ^{16}O nucleus ($= 217\ \mathrm{MeV}/c$ [48]).

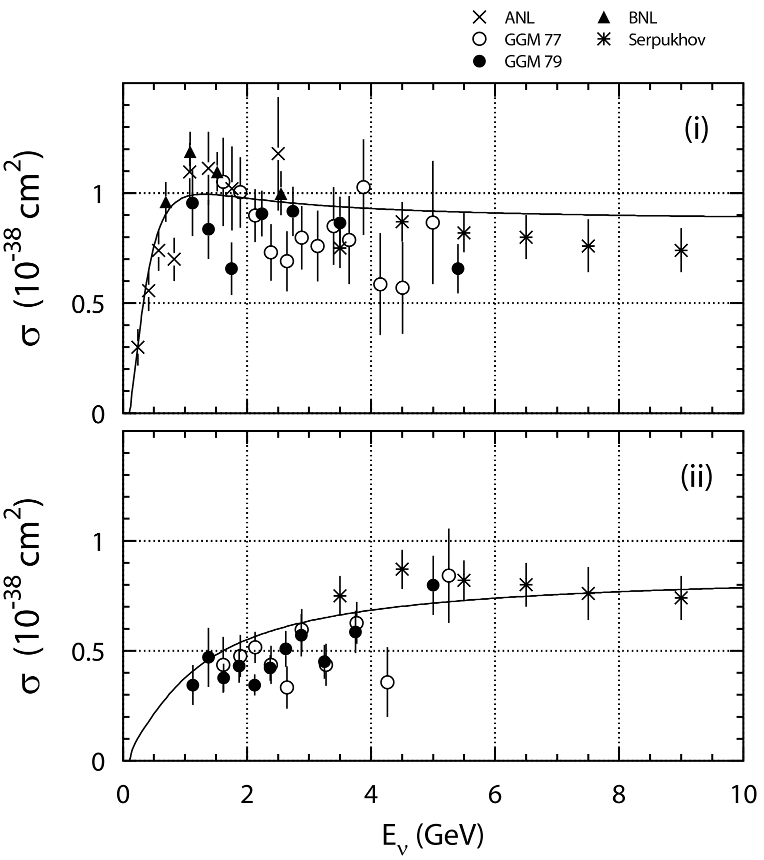

Figure 3.2: The total cross sections of (a) $\nu_\mu + n \rightarrow \mu^- + p$ and (b) $\overline{\nu}_\mu + p \rightarrow \mu^+ + n$. Solid lines show our calculations. Experimental data are from ANL [41], Gargamelle [42, 43], BNL [44] and Serpukhov [45].

3.2.3 Single-Meson Productions

Single-meson production is simulated based on the Rein & Sehgal's method [49]. This method assumes mediation by a baryon resonance :

$$\begin{array}{ll} \text{resonance production :} & \nu + N \to l + N^* \\ \text{resonance decay :} & N^* \to N' + \text{meson} \end{array}$$

where N^* represents a baryon resonance and the lepton l is either charged or neutral.

The differential cross section of a single resonance production with the mass M and the negligible width is written as :

$$\frac{d^2\sigma}{dq^2 dE_\nu} = \frac{1}{32\pi M_N E_\nu^2} \cdot \frac{1}{2} \sum_{spin} |T(\nu N \to l N^*)|^2 \, \delta(W^2 - M^2) \tag{3.15}$$

where W is the invariant mass of the hadronic system. $T(\nu N \to l N^*)$ is the amplitude of the resonance production and calculated using the FKR model [50]. For the resonance of finite width Γ, the δ-function in the differential cross section can be replaced by a Breit-Wignar factor :

$$\delta(W^2 - M^2) \quad \to \quad \frac{1}{2\pi} \cdot \frac{\Gamma}{(W-M)^2 + \Gamma^2/4} \tag{3.16}$$

To derive a meson production cross section, the production amplitude of each resonance is multiplied by the probability of the resonance decay into a nucleon and that meson. In our simulation, 18 baryon resonances which can be produced in $W < 2.0\,\mathrm{GeV}/c^2$ region are considered, the strongest being $\Delta(1232)$. Interference among these resonances is also taken into account. In Figures 3.3, 3.4 and 3.5, the calculated cross sections for single-pion productions are show with data from several experiments. It can be seen that the calculated cross sections agree well with experimental data. Though the Rein & Sehgal's method was originally developed for calculations of single-pion production cross sections, we extend this to single-η or single-K production.

In our simulation, the decay kinematics of $\Delta(1232)$ is decided by the Rein & Sehgal's detailed method taking the effect of polarization into account. For the decays of other resonances, we assume that the meson is emitted isotropically in the resonance rest frame.

3.2.4 Multi-Pion Productions

For CC deep inelastic neutrino-nucleon scattering, the cross section is expressed as [60] :

$$\begin{aligned} \frac{d^2\sigma^{\nu(\bar{\nu})}}{dxdy} &= \frac{G_F^2 M_N E_\nu}{\pi} \left((1 - y + \frac{y^2}{2} + C_1) F_2(x, q^2) \pm y(1 - \frac{y}{2} + C_2) x F_3(x, q^2) \right) \\ C_1 &= \frac{ym^2}{4M_N E_\nu x} - \frac{xyM_N}{2E_\nu} - \frac{m^2}{4E_\nu^2} - \frac{m^2}{2M_N E_\nu x} \\ C_2 &= -\frac{m^2}{4M_N E_\nu x} \end{aligned} \tag{3.17}$$

where x and y are Bjorken parameters, M_N is the nucleon mass and m is the outgoing lepton mass. For the nucleon structure functions F_2 and xF_3, we adopt the result of GRV94 [61]. Using

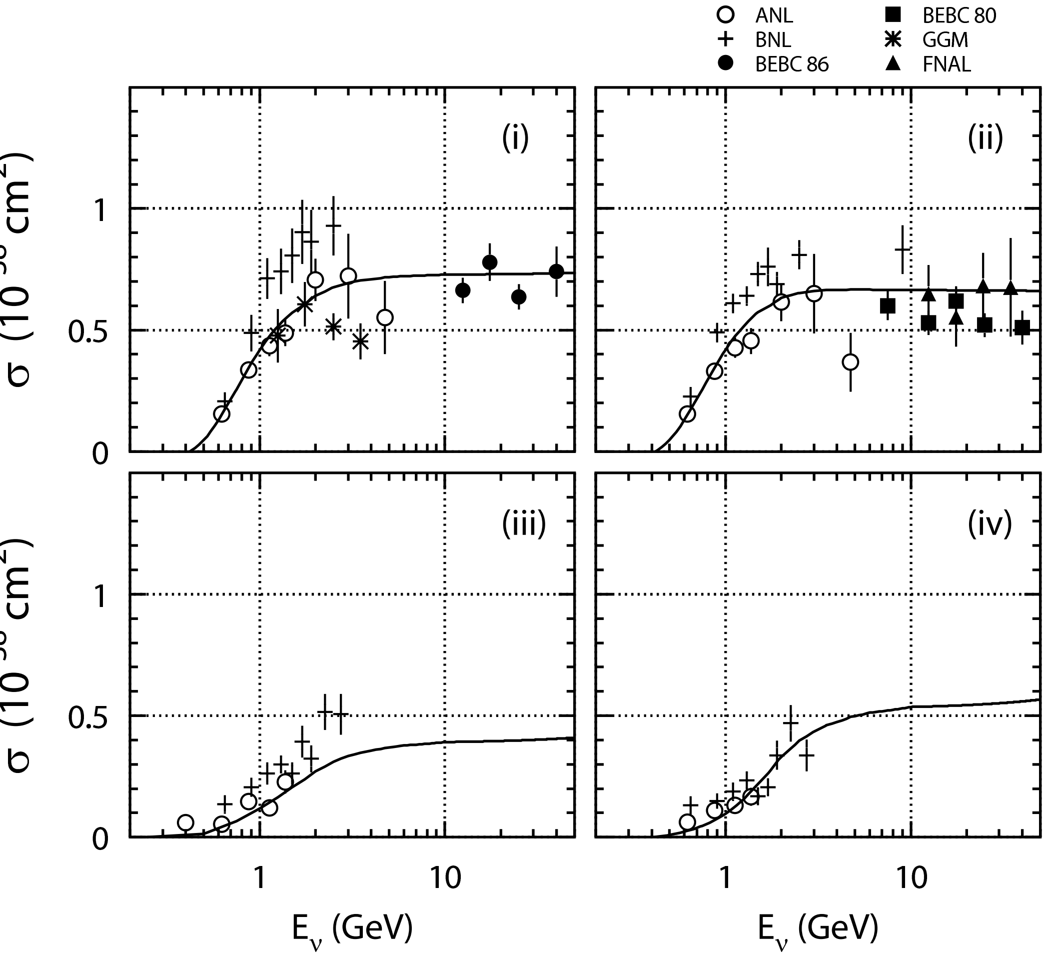

Figure 3.3: The total cross sections for CC single-pion productions of ν_μ. (a) $\nu_\mu p \to \mu^- p \pi^+$, (a') $\nu_\mu p \to \mu^- \Delta^{++}$ ($\nu_\mu p \to \mu^- p \pi^+$ in $W < 1.4$ GeV/c^2), (b) $\nu_\mu n \to \mu^- p \pi^0$, (c) $\nu_\mu n \to \mu^- n \pi^+$. Solid lines show our calculations. Experimental data are from ANL [51], BNL [52], BEBC [53, 54], Gargamelle [55] and FNAL [56].

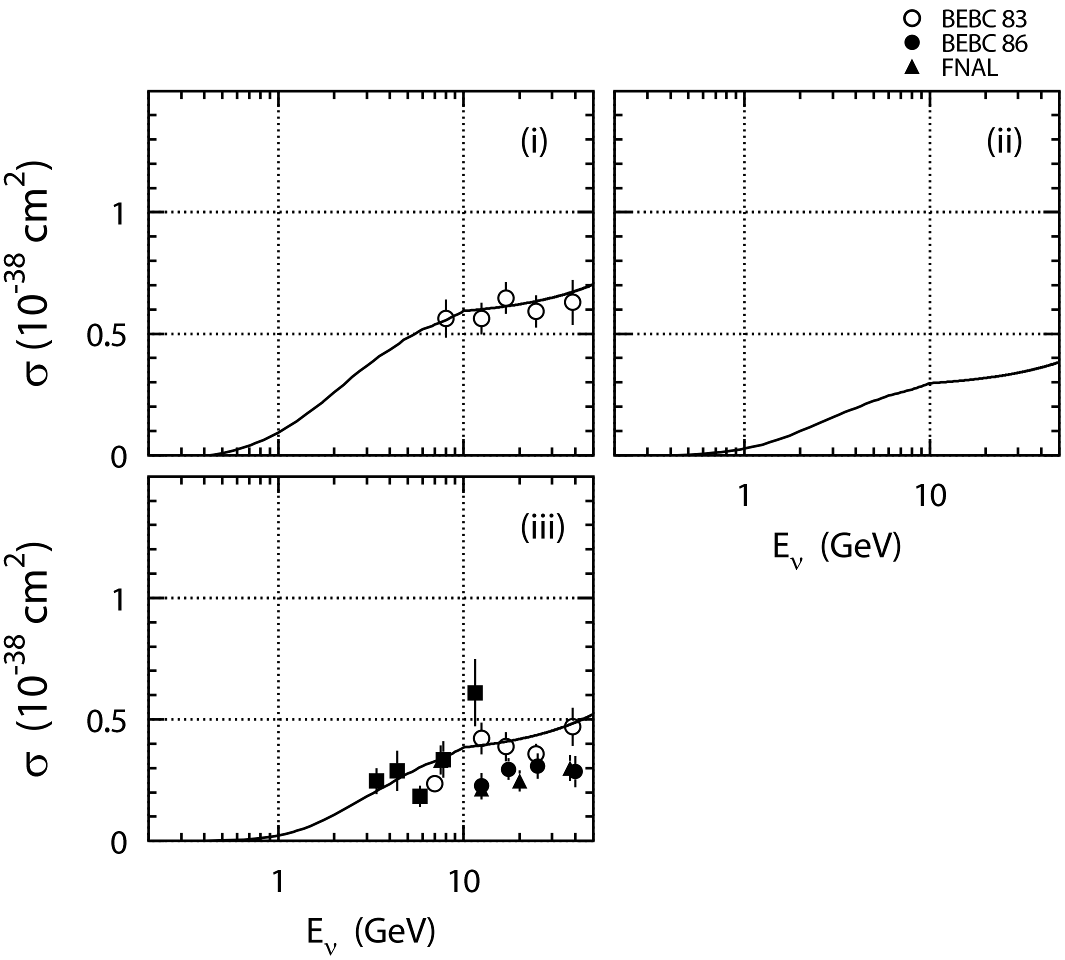

Figure 3.4: The total cross sections for CC single-pion productions of $\overline{\nu}_\mu$. (a) $\overline{\nu}_\mu n \to \mu^+ n \pi^-$, (b) $\overline{\nu}_\mu p \to \mu^+ n \pi^0$, (c) $\overline{\nu}_\mu p \to \mu^+ p \pi^-$. Solid lines show our calculations. Experimental data are from BEBC [57, 53] and FNAL [58].

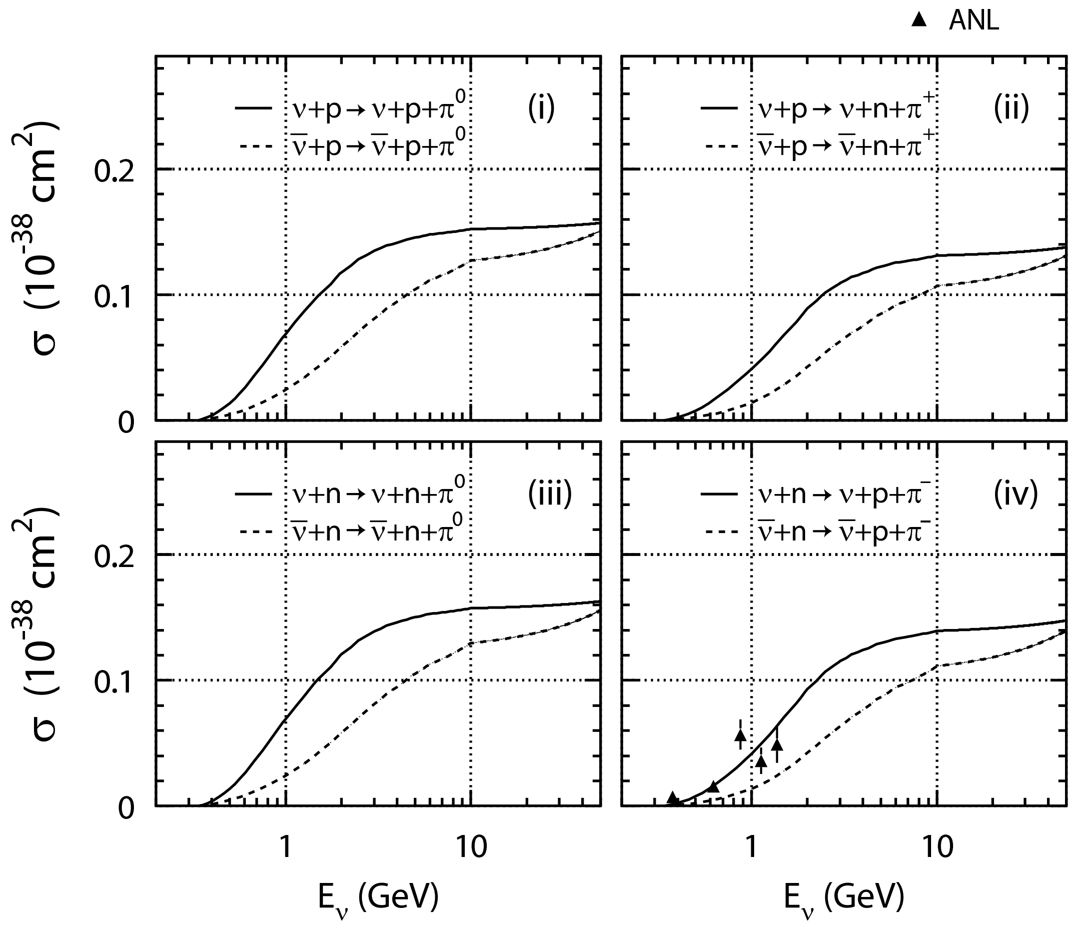

Figure 3.5: The total cross sections for NC single-pion productions of ν_μ and $\overline{\nu}_\mu$. Solid(Dashed) lines show our calculations for $\nu_\mu(\overline{\nu}_\mu)$ interactions. Experimental data are from ANL [59].

the above equation, we calculate the cross sections of CC multi-meson productions which satisfy $W > 1.3$ GeV/c^2.

In the region of $1.3\,\mathrm{GeV}/c^2 < W < 2.0\,\mathrm{GeV}/c^2$, we consider only pions as the produced mesons. The mean multiplicity of pions is estimated using the result of the Fermilab 15-foot bubble chamber experiment [62] :

$$\langle n_\pi \rangle = 0.09 + 1.83 \ln(W^2) \tag{3.18}$$

where $\langle n_{\pi^+} \rangle = \langle n_{\pi^-} \rangle = \langle n_{\pi^0} \rangle$ is assumed. For an individual event, the pion multiplicity is determined using KNO (Koba-Nielsen-Olsen) scaling. Keeping consistency with our cross section calculation method of single-meson productions which covers the $W < 2.0\,\mathrm{GeV}/c^2$ region (Section 3.2.3), we treat only deep inelastic scatterings with pion multiplicities above 1 in this region. The forward-backward asymmetry of outgoing pions in the hadronic center of mass system is also considered using results from the BEBC experiment [63] :

$$\frac{n_\pi^F}{n_\pi^B} = \frac{0.35 + 0.41 \ln(W^2)}{0.5 + 0.09 \ln(W^2)} \tag{3.19}$$

where the superscript F(B) means the forward(backward) direction of the hadronic system in the laboratory frame.

In the region of $W > 2.0\,\mathrm{GeV}/c^2$, the kinematics of the hadronic system are determined by JETSET/PYTHIA package [64]. This package treats not only pions but also K, η, ρ and so on.

NC cross section of deep inelastic scatterings are determined using the following relations estimated from experimental results [65, 66] :

$$\frac{\sigma(\nu N \to \nu X)}{\sigma(\nu N \to \mu^- X)} = \begin{cases} 0.26 & (\ E_\nu < 3\,\mathrm{GeV}\ ) \\ 0.26 + 0.04\,(E_\nu/3 - 1) & (\ 3\,\mathrm{GeV} \le E_\nu < 6\,\mathrm{GeV}\ ) \\ 0.30 & (\ E_\nu \ge 6\,\mathrm{GeV}\ ) \end{cases} \tag{3.20}$$

$$\frac{\sigma(\bar\nu N \to \bar\nu X)}{\sigma(\bar\nu N \to \mu^+ X)} = \begin{cases} 0.39 & (\ E_\nu < 3\,\mathrm{GeV}\ ) \\ 0.39 - 0.02\,(E_\nu/3 - 1) & (\ 3\,\mathrm{GeV} \le E_\nu < 6\,\mathrm{GeV}\ ) \\ 0.37 & (\ E_\nu \ge 6\,\mathrm{GeV}\ ) \end{cases} \tag{3.21}$$

The calculated CC total cross sections for both neutrinos and anti-neutrinos are shown in Figure 3.6, along with experimental data. The total cross sections are calculated summing up the cross section of each interaction channel, namely quasi-elastic scattering, single-meson productions, multi pion productions and coherent pion productions.

3.2.5 Nuclear Effects

Pions as products of a neutrino-nucleon interaction in ^{16}O nucleus often invite secondary interactions before leaving the nucleus.

We simulate nuclear effects of inelastic scattering, charge exchange and absorption. The cross section of each interaction is calculated using the model of Oset *et al.* [79]. The nuclear density in ^{16}O nucleus is assumed to be the Wood-Saxon form :

$$\rho(r) = \frac{Z}{A}\rho_0 \frac{1}{1 + \exp(\frac{r-c}{a})} \tag{3.22}$$

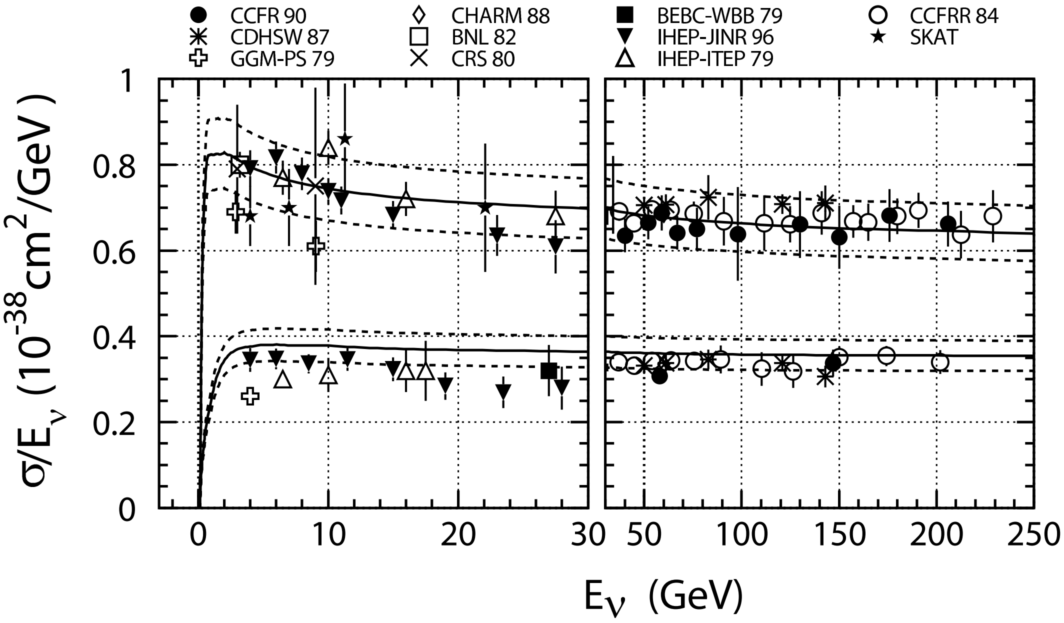

Figure 3.6: The CC total cross sections for both neutrinos and anti-neutrinos. Solid lines show our calculations for (upper line) CC neutrino interactions and (lower line) CC anti-neutrino interactions, along with the $\pm$ 10% scaled results (dashed lines). Experimental data are from CCFR [67], CDHSW [68], Gargamelle [69, 70], CHARM [71], BNL [72], CRS [73], BEBC-WBB [74], IHEP-JINR [75], IHEP-ITEP [76], CCFRR [77] and SKAT [78].

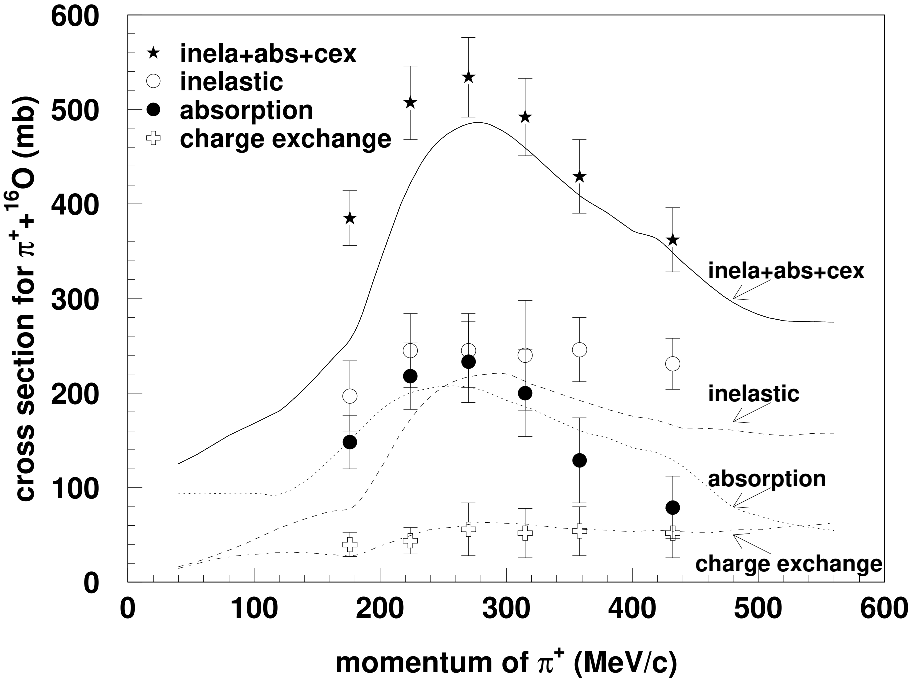

Figure 3.7: The cross sections of $\pi^+ - ^{16}$O interactions. The results of our calculation(lines) are shown with experimental data (points) taken from [81]

We choose ρ_0=0.48 m_π^3, a=0.41 fm, c=2.69 fm, Z=8 and A=16 for ^{16}O nucleus. In order to determine the angular and momentum distribution of scattered pions, we use the experimental results of $\pi - N$ phase shift analysis [80]. In addition, Pauli blocking is taken into account. For all interactions, the momentum of the outgoing nucleon must be above Fermi surface momentum of :

$$p_F(r) = \left(\frac{3}{2}\pi^2\rho(r)\right)^{\frac{1}{3}} \tag{3.23}$$

Figure 3.7 shows the calculated $\pi^+ - ^{16}$O interaction cross sections as a function of the initial pion momentum. The result of our simulation agrees well with Experimental data shown together. The calculated probability of each $\pi^0 - ^{16}$O interaction is shown in Figure 3.8.

3.3 Detector Simulation

Given their kinematics in the neutrino interaction simulation code, outgoing particles are tracked by a detector simulation program in turn. This detector simulator is a program based on GEANT package [82]. Figure 3.1 lists various processes which the GEANT original code serves in our simulation program.

We select CALOR package [83] to simulate hadronic interactions in water. This package has known to well reproduce the pion interactions down to low energy region. For still lower energy

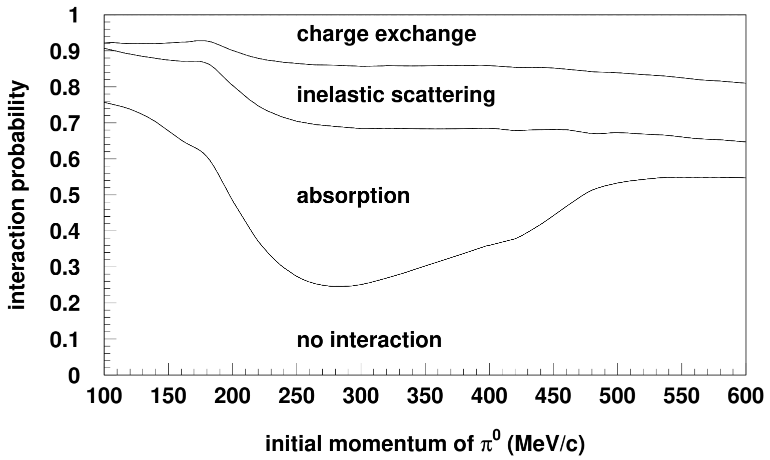

Figure 3.8: The calculated probability of each π^0–^{16}O interaction

γ	(e^+, e^-) pair production Compton scattering Photoelectric effect
$e^\pm$	Multiple scattering Ionization and δ-rays production Bremsstrahlung Annihilation of positron Generation of Cherenkov radiation
$\mu^\pm$	Decay in flight Multiple scattering Ionization and δ-rays production Bremsstrahlung Direct (e^+, e^-) pair production Nuclear interaction Generation of Cherenkov radiation
Hadrons	Decay in flight Multiple scattering Ionization and δ-rays production Hadronic interactions Generation of Cherenkov radiation

Table 3.1: Processes served by the GEANT original code in our simulator.

region of $p_\pi \leq 500$ MeV/c, we have developed a custom program [84] based on experimental data of $\pi-^{16}$O scattering [85] and $\pi - p$ scattering [86].

Some processes involving Cherenkov photons are simulated by our custom code, such as scattering and absorption in the detector water, reflection and absorption on detector material, and detection by PMTs including responses from frontend electronics. Below is the brief explanation of each.

As for the attenuation of a Cherenkov photon in water, Rayleigh scattering, Mie scattering and absorption are considered. For shorter wavelength photons ($\lambda \lesssim 450$ nm), the dominant interaction is Rayleigh scattering which is caused by H_2O molecules or other tiny particles ($r \ll \lambda$, with r being the particle's radius) in water. The cross section of this process has power dependence of λ^{-4} and becomes larger at shorter wavelength. For photons with longer wavelength ($\lambda \gtrsim 450$ nm), absorption process by H_2O molecules dominates. The amplitude of absorption are taken from experimental data. Mie scattering is caused by relatively large particles ($r \gg \lambda$) and characterized by a sharp peak in the forward direction. Figure 2.17 shows attenuation coefficients used in our simulation. The absolute factor of each coefficient is tuned to reproduce measurement results of the laser system (Section 2.3.5). Validity of these factors is confirmed by cosmic ray muon measurement (Section 2.3.4).

Light reflection and absorption on detector material are simulated using angular probability functions estimated from the direct measurement.

To simulate photon detection by PMT, we use measured quantum efficiency. The amount of p.e.s detected in each PMT is derived summing up the individual p.e. with weights by measured single p.e. distribution. For the simulation of PMT timing resolution, hit time information of each PMT is smeared using measured timing resolution according to detected p.e.s. Behavior of frontend electronics, ATM (Section 2.2.3), such as charge collecting time window and signal threshold, is also taken into account.

Simulated data are written in a ZEBRA based format [87]. Since it is the same format as used for the observed data, all reduction and reconstruction programs can be run on both.

Chapter 4

Data Reduction

4.1 Overview

Super-Kamiokande triggers $\sim 10^6$ events/day excluding the SLE triggered events (for trigger types, see Section 2.2.3). Among them are ~ 10 atmospheric neutrino events/day. By applying appropriate reduction processes to the data, we must eliminate backgrounds such as cosmic ray muon events or radioactivity-induced low energy events.

Atmospheric neutrino events observed in Super-Kamiokande are classified into four classes, fully contained (FC), partially contained (PC), upward stopping muons (StopMu) and upward through-going muons (ThruMu), as shown in Figure 4.1. FC events have no activity in the OD. In a FC event, the event vertex is contained inside the fiducial volume and no visible particle exits the ID. PC events have also their vertices inside the fiducial volume, but at least one visible particle exits the ID, leaving some activities in the OD. Muons produced by neutrino interactions in the rock surrounding the detector sometimes enter the ID. Among these neutrino-induced entering muons, downward going muons cannot be distinguished from cosmic ray muons by nature. Therefore only upward going muons are studied. In StopMu events, entering muons stop inside the ID, while in ThruMu events, muons entering muons pass through the ID.

For the analysis in this thesis, only FC events are used. The data reduction process for FC

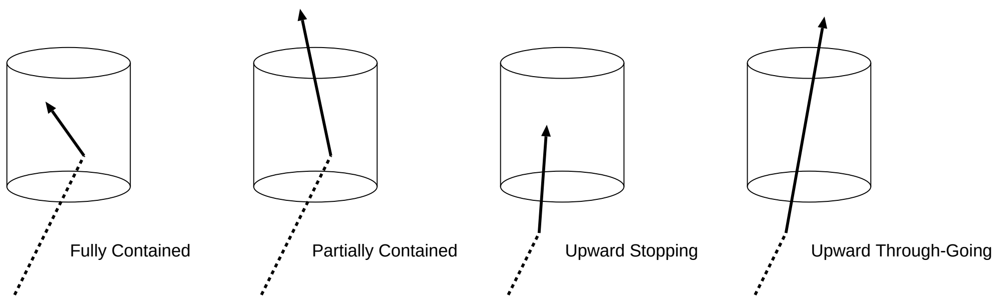

Figure 4.1: Event categories for Super-Kamiokande atmospheric neutrino events. Dashed lines show trajectories of primary neutrinos, and solid arrows show those of secondary charged particles.

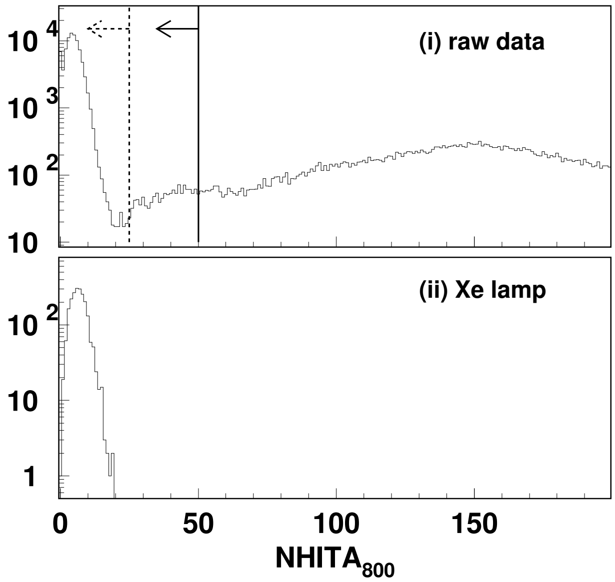

Figure 4.2: The $NHITA_{800}$ distributions for (i) the raw data and (ii) the Xe lamp data. A solid (dashed) arrow shows a FC selection criterion in the first (second) reduction stage.

events is done in five stages.

4.2 First Reduction

This is a collection of simple cuts to quickly reduce the data to a manageable size. First, events where the number of hit OD PMTs in a fixed 800 nsec time window ($NHITA_{800}$) is greater than 50 are rejected. This removes a large part of the cosmic ray muon events without endangering FC events. Figure 4.2-(i) shows the $NHITA_{800}$ distribution for the raw data. A solid arrow shows this selection criterion. Figure 4.2-(ii) shows the $NHITA_{800}$ distribution for the Xe lamp data. In a Xe calibration run (see Section 2.3.1), the light source is placed at the center of the inner tank and the total charge in each event amounts to 370000 p.e. corresponding to 40 GeV. This figure shows that the light leak from the ID to the OD is negligible.

Next, events where the maximum of the total p.e.s over all ID PMTs in a sliding 300 nsec time window (PE_{300}) is less than 200, which corresponds to a visible energy of 23 MeV, are also rejected. Since events with visible energy below 30 MeV are not used for the analysis in this thesis, this cut is safe. Figure 4.3 shows the PE_{300} distribution for the raw data. The raw data contains cosmic ray muon events (hatched region), low energy radioactivity events (peak around 60 p.e.) and Michel electron events from the decay of cosmic ray muons (peak around 500 p.e.). Among these backgrounds, cosmic ray muon events are largely rejected by the $NHITA_{800}$ cut explained above, and low energy radioactivity events are removed by this PE_{300} cut.

In addition, events whose time interval from the previous event (TDIFF) is less than 100 μsec are rejected. Figure 4.4 shows the TDIFF distribution for the raw data. The nominal value of 10^{-1} sec corresponds to the trigger rate of ~ 10 Hz. A peak around 10^{-6} sec comes from cable

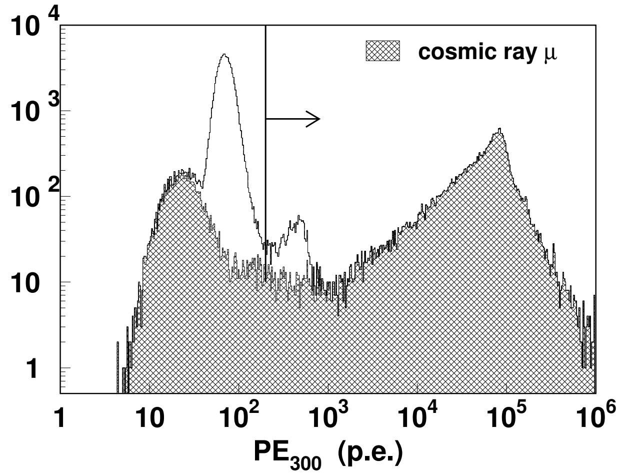

Figure 4.3: The PE_{300} distribution for the raw data. The hatched region shows the contribution from cosmic ray muon events, which are selected by requiring $NHITA_{800} > 25$. The selection criterion in the first reduction stage is shown by a arrow.

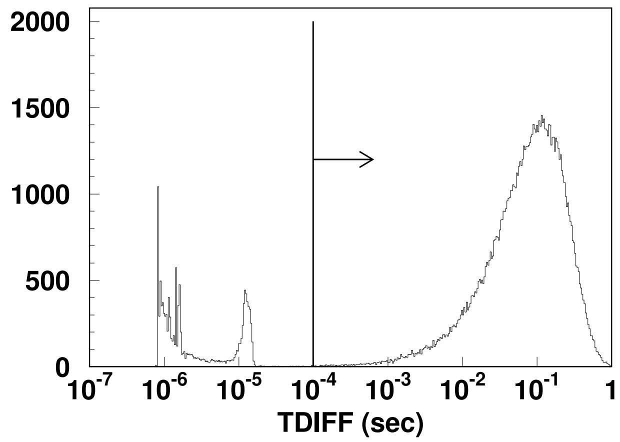

Figure 4.4: The TDIFF distribution for the raw data. The selection criterion in the first reduction stage is shown by a arrow.

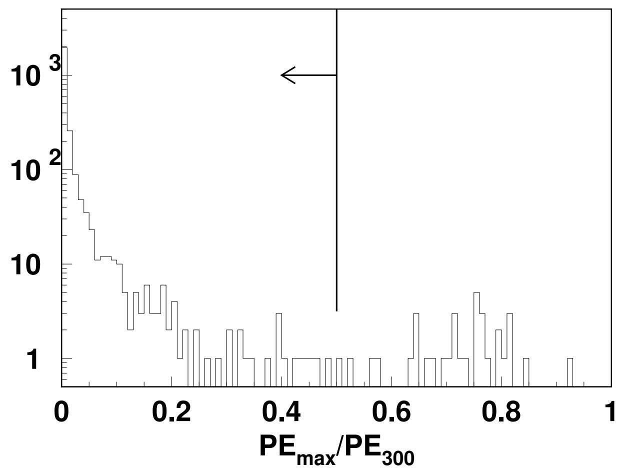

Figure 4.5: The $\mathrm{PE}_{\mathrm{max}}/\mathrm{PE}_{300}$ distribution for data after the first reduction. The selection criterion in the second reduction stage is shown by a arrow.

reflection signals of the ID PMTs, while a peak around 10^{-5} sec is due to after pulsing of the PMTs. The decay curve between 10^{-6} sec and 10^{-5} sec is made by decay electrons from stopping cosmic ray muons. Those unwanted events are eliminated the TDIFF cut shown by a arrow in the figure.

The process reduces $\sim 10^6$ raw events/day to ~ 3000 events/day.

4.3 Second Reduction

Here, the OD cut is tightened in such a way that events with NHITA_{800} greater than 25 are rejected, as shown by a dashed arrow in Figure 4.2. In addition, a simple cut is introduced to get rid of some flasher events. It sometimes occurs that a PMT starts to flash because of a discharge around the dynode structure. The flashing PMT tends to record a very large charge. If the ratio of the maximum p.e.s of a single ID PMT ($\mathrm{PE}_{\mathrm{max}}$) to PE_{300} is greater than 0.5 in an event, the event is discarded as a flasher event. Figure 4.5 shows the $\mathrm{PE}_{\mathrm{max}}/\mathrm{PE}_{300}$ distribution for data after the first reduction.

This reduces ~ 3000 events/day after the first reduction to ~ 200 events/day.

4.4 Third Reduction

This reduction process removes remaining specific types of backgrounds. About 40 events/day are left after the third reduction.

Through-going muon cut

In the first and second reduction stages, cosmic ray muon events are mostly eliminated by the NHITA_{800} cut. Therefore remaining cosmic ray events have only small numbers of hit OD

PMTs. To remove these muons safely, their vertex position and direction are reconstructed and only OD PMT hits close to the estimated muon entrance points and exit points are counted.

Events which satisfy the following criteria are rejected as through-going muons :

- $\mathrm{PE_{max}} > 230\,\mathrm{p.e.}$
- goodness of through-going muon fit > 0.75
- $\mathrm{NHITA_{in}} > 9$ or $\mathrm{NHITA_{out}} > 9$

where $\mathrm{NHITA_{in}}$ ($\mathrm{NHITA_{out}}$) is the number of hit OD PMTs inside the 8 m radius circular region with its center being the reconstructed muon entrance (exit) point. When a through-going muon exits the inner tank, the ID PMTs near the exit point are intensively lit up by Cherenkov light. The ATM channels connected to those PMTs tends to saturate. The fitter for through-going muons reconstructs the entrance and exit points by finding the clusters of earliest hit PMTs and saturated PMTs, respectively. The goodness of through-going muon fit is defined as :

$$goodness \quad = \quad \frac{1}{\sum_i \frac{1}{\sigma_i^2}} \times \sum_i \frac{1}{\sigma_i^2} \exp\left(- \frac{(t_i - T_i)^2}{2(1.5 \times \sigma_i)^2} \right) \tag{4.1}$$

where t_i and σ_i are observed hit time of the i-th PMT and its resolution, and T_i is the hit time expected from the muon entering time and its path. Typical goodness for a reconstructed through-going muon is about 0.9.

Stopping muon cut

Similarly, events satisfying the following criteria are rejected as stopping muons :

- $\mathrm{NHITA_{in}} > 9$
or
$\mathrm{NHITA_{in}} > 4$ if goodness of stopping muon fit > 0.5

The fitter for stopping muons reconstructs the entrance points by finding the clusters of earliest hit PMTs. It also reconstructs the muon direction to maximize the charge inside a cone with 42° of half-angle.

Cable-hole muon cut

Signal cables and HV supply cables of PMTs are fed out of the detector tank through some cable-holes. After several months' data taking from the beginning of the experiment, we found that the PMT cable bundles under cable-holes had obstructed the emitted light from entering muons and had caused the inefficiency of the OD. To eliminate these cable-hole muon events, four plastic scintillation counter measuring $2\,\mathrm{m} \times 2.5\,\mathrm{m}$ are placed on the top of the detector. A schematic view of a cable-hole muon and the veto counter is shown in Figure 4.6. An event, where at least one veto counter is fired and the distance from the counter position to the reconstructed vertex is less than 4 m, is rejected as a cable-hole muon event.

Figure 4.7 shows the reconstructed vertex distribution for the FC 1-ring μ-like sample in the upper half of the detector. Four clusters are clearly seen around cable holes before the veto counter installation, while no cluster is visible after the installation.

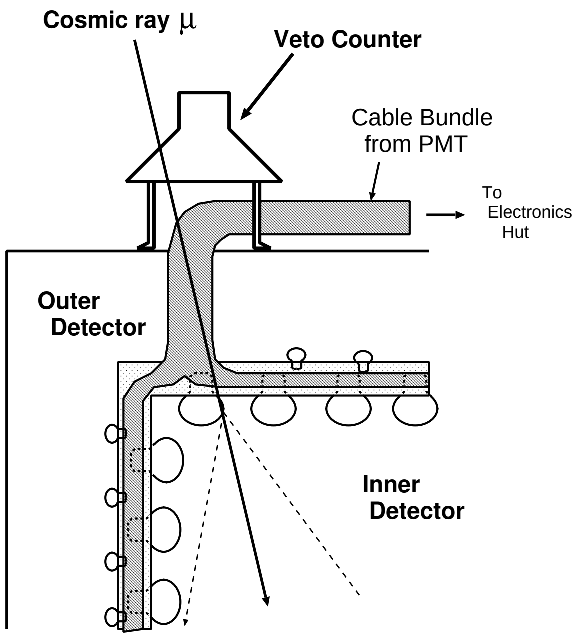

Figure 4.6: A schematic view of a cable-hole muon and the veto counter.

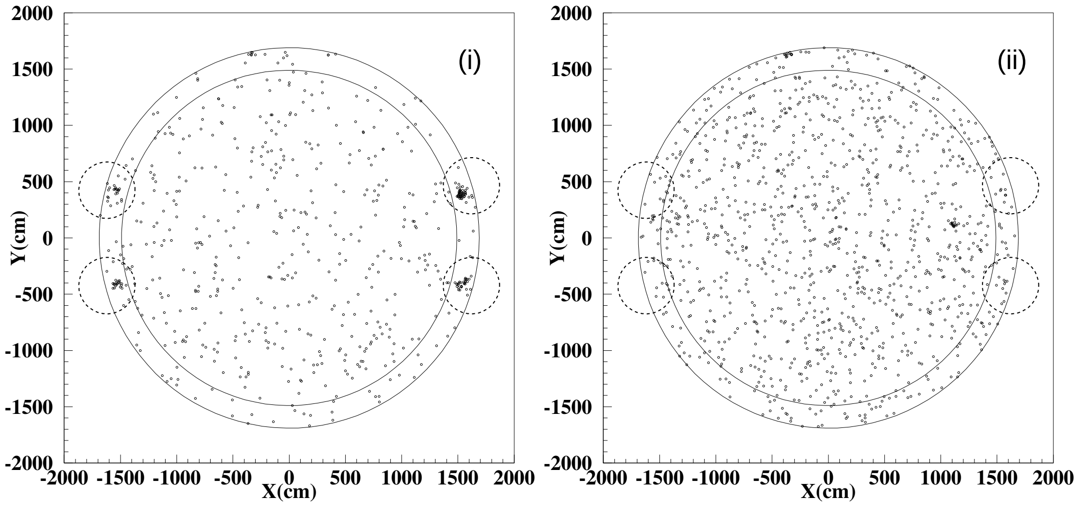

Figure 4.7: The reconstructed vertex distribution for the FC 1-ring μ-like sample before fiducial cut. Only events in the upper half of the detector are shown. The outer solid circle shows the ID wall and the inner solid circle shows the fiducial volume (2 m from the wall). Small dashed circles roughly indicate the positions where the veto counters are installed. Four clusters are clearly seen around cable holes (i) before the veto counter installation, while no cluster is visible (ii) after the installation.

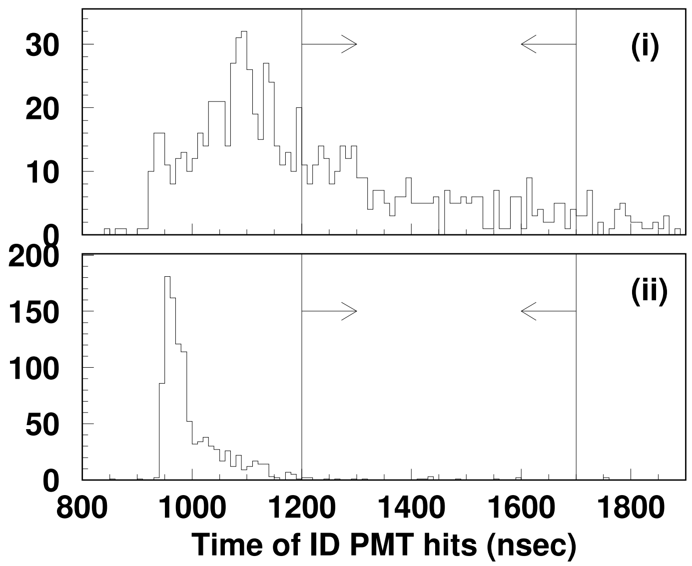

Figure 4.8: The timing distribution of (i) a typical long-tail flashing PMT event and (ii) a typical FC neutrino event. The arrows show the region to count NMIN_{100} (see text).

Low energy event cut

There are still low energy events which might be caused by radioactivities in the detector or flashing PMTs. A mimimum energy cut is applied to remove these remaining backgrounds. If the maximum number of hit ID PMTs in a sliding 50 nsec time window after subtracting TOF (NHIT_{50}) is less than 50, which corresponds to $\sim$ 9 MeV in visible energy, the event is discarded.

Flasher event cut

As described in the second reduction part, it sometimes occurs that a PMT starts to flash because of a discharge around the dynode structure. Events caused by these flashing PMTs usually have broader hit PMT timing distribution than neutrino events, as shown in Figure 4.8. We reject events which satisfy the following criteria as flashers :

- $\mathrm{NMIN}_{100} > 14$
  or
  $\mathrm{NMIN}_{100} > 9$ if the number of hit ID PMTs ≤ 800

where NMIN_{100} is the minimum number of hit ID PMTs in a sliding 100 nsec time window. This time window is slid between 1200 nsec and 1700 sec, as shown by arrows in Figure 4.8. Note that the TDC time of event trigger is always about 950 nsec because this is determined by the design of the logical circuit for the trigger signal generation. Therefore the time of 1200 nsec corresponds to about 250 nsec after the trigger timing and is completely off-timing in the case of neutrino events.

Accidental coincidence event cut

More than one event sometimes occurs within a single trigger gate by accident. Usually, a low energy event is followed by a cosmic ray muon event to form one event. The cut criteria to eliminate these events are :

- the number of hit OD PMTs in a fixed 500 nsec off-timing window from 1300 nsec to 1800 nsec is greater than 19
- the total number of p.e.s of the ID PMTs in a fixed 500 nsec off-timing window from 1300 nsec to 1800 nsec is greater than 5000 p.e.

Events which satisfy the both criteria are removed as accidental coincidence events.

Calibration event cut

Some of the calibration data are taken automatically during normal data taking. Lasers provide PMT timing and water attenuation length calibration, while a Xe lamp is used for PMT gain calibration (see Section 2.3). These calibration sources flash at given time intervals. The signals of monitoring PMTs in each calibration system are fed into assigned channel of ATMs. Events where at least one calibration channel is on are removed in this reduction stage.

4.5 Fourth Reduction

In this stage, an intelligent pattern matching algorithm is used for rejecting the remaining flasher events. Since the flashing is an instrumental problem with a PMT, it is likely to repeat. PMTs in the same region of the detector will be hit with the similar charge, several times over the course of hours or days. Neutrino events, of course, are unlikely to repeat in such a way.

The algorithm of the pattern matching is as follows :

(1) Divide the ID wall into 1450 $2\,\mathrm{m}\times 2\,\mathrm{m}$ square patches.

(2) Compute the total charge in the i-th patch.

(3) Two events, A and B are compared, and their correlation is calculated as :

$$r = \frac{1}{N}\sum_{i}\frac{\left(Q_i^A - \langle Q^A\rangle\right)\times\left(Q_i^B - \langle Q^B\rangle\right)}{\sigma_A \times \sigma_B} \tag{4.2}$$

where $\langle Q^{A(B)}\rangle$ and $\sigma_{A(B)}$ is the average and the standard deviation of $Q_i^{A(B)}$, respectively. N is the number of patches.

(4) If r exceeds the threshold r_{th} as a function of total charge, events A and B are recognized as 'matching' events.

(5) Calculate r over all events, and count the number of matching events (N_{match}).

(6) Reject events with large r or large N_{match}.

A detailed description of this intelligent flasher cut can be found in Ref.[88].

After the fourth reduction, ~ 18 events/day are left.

4.6 Fifth Reduction

The fifth reduction process consists of some ramified cuts. Finally, after the fifth reduction, ~ 15 events/day are left as FC events.

Invisible muon cut

An invisible muon event is caused by a decay electron from a muon with momenta below the Cherenkov threshold. These events are characterized by a low energy signal in the ID and some activity in the OD whose timing is earlier than that of the ID. Events satisfying all the cuts below are removed :

- the total p.e.s of hit ID PMTs < 1000
- $\mathrm{NHITA_{early}} > 4$
- $\mathrm{NHITA_{early}} + \mathrm{NHITA_{800}} > 9$ if $\mathrm{DIS_{clust}} < 500\,\mathrm{cm}$ and $\mathrm{NHITA_{800}} > 1$
  $\mathrm{NHITA_{early}} > 9$ otherwise

where $\mathrm{NHITA_{early}}$ is the maximum number of hit OD PMTs in a 200 nsec time window slid from -8000 nsec to 800 nsec. $\mathrm{DIS_{clust}}$ is distance between two clusters consist of the OD PMTs hit in a time window for $\mathrm{NHITA_{early}}$ and the OD PMTs hit in a time window for $\mathrm{NHITA_{800}}$.

Coincidence muon cut

Events which satisfy the following criteria are removed as accidental coincidence of a low energy event and a muon event :

- the total number of p.e.s of the ID PMTs in a fixed 500 nsec time window from 800 nsec to 1300 nsec is less than 300 p.e.
- the maximum number of hit ID PMTs in a 200 nsec late-timing window slid from 1300 nsec to 2500 nsec is greater than 19

Electronics noise event cut

These events are usually caused by electrical interference from a flashing fluorescent light in one of four electronics huts. They are characterized by a strange peak around 0.5 p.e. in the charge distribution. Events satisfying both of the cuts below are rejected :

- $\mathrm{NHIT_{<1pe}} > 250$
- $\mathrm{NHIT_{<1pe}} > \mathrm{NHIT_{>1pe}} + 100$

where $\mathrm{NHIT_{<1pe}}$ ($\mathrm{NHIT_{>1pe}}$) shows the number of hit ID PMTs with detected charge below (above) 1 p.e..

Dead hut cut

All the PMT signal cables are connected to the electronics (ATMs) placed in four electronics huts. Reject events if any of the huts had no hit PMTs.

Long tail flasher cut

This is a stricter version of the flasher cut in the third reduction stage, especially for those events with small goodness in the vertex fitter. Events satisfying the following criterion are removed :

- $\mathrm{NMIN}_{100} > 5$ if the goodness in the simple vertex fitter < 0.4

where the definition of NMIN_{100} is same as that used in the third reduction.

Chapter 5

Event Reconstruction

We apply reconstruction algorithms to events which pass data reduction processes. The following five stages are proceeded in this order :

(1) Vertex Fitting

(2) Ring Counting

(3) Particle Identification

(4) Precise Vertex Fitting

(5) Momentum Determination

Physics measurement of an event such as the vertex position, the number of Cherenkov rings, particle types and momentum vectors are automatically determined by these algorithms. The same programs are run both on observed data and on Monte Carlo.

Each of these stages are explained in the following sections.

5.1 Vertex Fitting

The first stage of the reconstruction procedure is the vertex fitting. The vertex position is estimated to the point at which the timing residual distribution of hit PMTs is most peaked. This algorithm consists of three steps. During these three steps, an event is assumed to be single-ring.

Pfit

Pfit roughly estimates the vertex position by assuming a point-like light source. The goodness of the fitting is calculated by :

$$G_p = \frac{1}{N}\sum_i \exp\left(-\frac{(t_i - t_0)^2}{2\,(1.5\times\sigma)^2}\right) \tag{5.1}$$

where N is the number of hit PMTs, t_i is the time residual of the i-th PMT, t_0 is the mean of t_i, σ is the PMT timing resolution (2.5 nsec) and the factor 1.5 is chosen to optimize the fitter

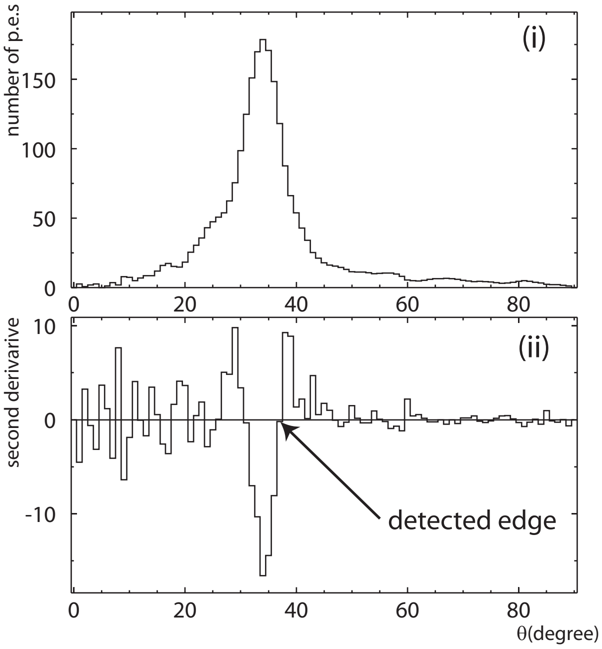

Figure 5.1: (i) The typical PE(θ) distribution and (ii) its second derivative.

performance. According to the assumed vertex position, t_i (and t_0) has a different value. The fitter searches for the vertex which gives the maximum value of G_p.

After finding the rough vertex position, the ring direction is also roughly estimated by summing up the charge-weighted vector to each PMT.

Ring Edge Search

In this step, the direction and the outer edge of a Cherenkov ring are selected to maximize the estimator $Q(\theta_{\text{edge}})$ defined as :

$$Q(\theta_{\text{edge}}) = \frac{\int_0^{\theta_{\text{edge}}} \text{PE}(\theta) d\theta}{\sin\theta_{\text{edge}}} \times \left(\left. \frac{d\text{PE}(\theta)}{d\theta} \right|_{\theta=\theta_{\text{edge}}} \right)^2 \times \exp\left(- \frac{(\theta_{\text{edge}} - \theta_{\text{exp}})^2}{2\sigma_\theta^2} \right) \tag{5.2}$$

where θ_{exp} is the Cherenkov opening angle expected from the charge within the cone, and σ_θ is its resolution. PE(θ) is the angular distribution of the detected p.e.s as a function of the polar angle θ from the charged particle direction. Each detected p.e. is corrected for water transparency and PMT acceptance. Figure 5.1-(i) shows the typical PE(θ) distribution. The ring edge position θ_{edge} is determined to satisfy :

- $\left. \dfrac{d^2\text{PE}(\theta)}{d^2\theta} \right|_{\theta_{\text{edge}}} = 0$
- $\theta_{\text{edge}} > \theta_{\text{peak}}$ (θ_{peak} is the angle where PE(θ) takes a maximum)

Figure 5.1-(ii) shows the second derivative of PE(θ).

TDCfit

Unlike Pfit, which assumes a point-like light source, TDCfit handles track lengths of charged particles and scattered Cherenkov photons.

The time residual of the i-th PMT is calculated by :

$$t_i = \begin{cases} t_i^0 - \dfrac{1}{c} \times |\overrightarrow{X_i} - \overrightarrow{O}| - \dfrac{n}{c} \times |\overrightarrow{P_i} - \overrightarrow{X_i}| & \text{for PMTs inside the Cherenkov ring} \\ t_i^0 - \dfrac{n}{c} \times |\overrightarrow{P_i} - \overrightarrow{O}| & \text{for PMTs outside the Cherenkov ring} \end{cases} \tag{5.3}$$

where t_i^0 is the hit time of the i-th PMT, $\overrightarrow{O}$ is the assumed vertex position, $\overrightarrow{P_i}$ is the position of the i-th PMT, $\overrightarrow{X_i}$ is the estimated position at which Cherenkov photons are emitted toward the i-th PMT and n is the refractive index of water. In Equation (5.3), the light speed is used as speeds of charged particles, because we cannot determine them accurately at this stage.

We define the fitting estimator G_I for the hit PMTs inside the cone, as follows :

$$G_I = \sum_i \frac{1}{\sigma_i^2} \exp\left(-\frac{(t_i - t_0)^2}{2\,(1.5 \times \sigma)^2}\right) \tag{5.4}$$

where σ_i is the timing resolution of the i-th PMT as a function of detected p.e.s, σ is the timing resolution for the average p.e.s over all hit PMTs and t_i is the time residual of the i-th PMT calculated by Equation (5.3).

For hit PMTs outside the cone, we consider scattered Cherenkov photons, like :

$$G_{O1} = \sum_i \frac{1}{\sigma_i^2} \left(\max\left[\exp\left(-\frac{(t_i - t_0)^2}{2\,(1.5 \times \sigma)^2}\right) \;,\; G_{\text{scatt}}(t_i, t_0)\right] \times 2 - 1\right) \qquad (\text{ for } t_i > t_0 \text{ }) \tag{5.5}$$

$$G_{O2} = \sum_i \frac{1}{\sigma_i^2} \left(\exp\left(-\frac{(t_i - t_0)^2}{2\,(1.5 \times \sigma)^2}\right) \times 2 - 1\right) \qquad (\text{ for } t_i \leq t_0 \text{ }) \tag{5.6}$$

where

$$G_{\text{scatt}}(t_i, t_0) = \frac{R_q}{1.5^2} \times \exp\left(-\frac{(t_i - t_0)^2}{2\,(1.5 \times \sigma)^2}\right) + \left(1 - \frac{R_q}{1.5^2}\right) \times \exp\left(-\frac{t_i - t_0}{60\text{nsec}}\right) \tag{5.7}$$

R_q is the fraction of the p.e.s detected inside the Cherenkov cone. Numerical factors in the equations are results of the optimization.

Then total estimator of TDCfit is :

$$G_T = \frac{G_I + G_{O1} + G_{O2}}{\displaystyle\sum_i \frac{1}{{\sigma_i}^2}} \tag{5.8}$$

TDCfit finds the vertex position and the ring direction giving the maximum value of G_T.

The resolution of the fitting algorithm described in this section is estimated to be 61cm and 51cm for single-ring and multi-ring events, respectively. This is the final reconstructed vertex for multi-ring events. In case of single-ring events, the further fitting algorithm is applied (see Section 5.4).

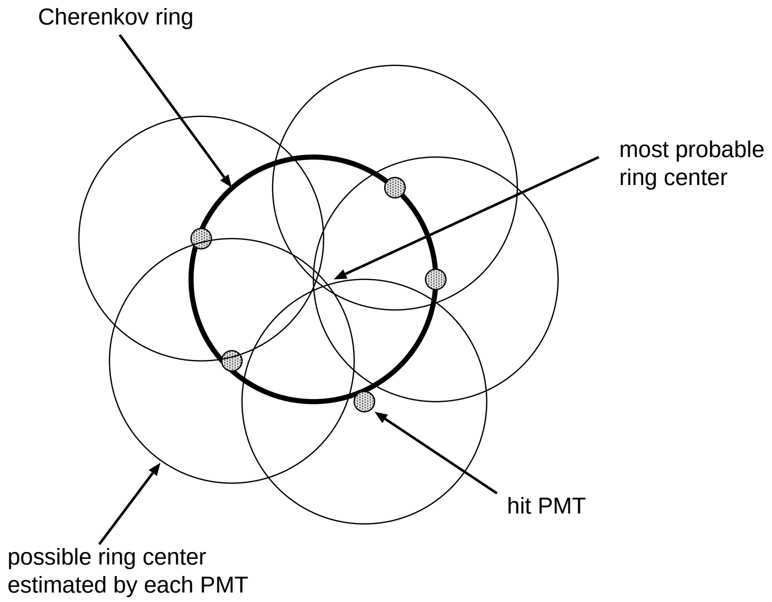

Figure 5.2: The basic idea of the ring candidate search. The most intersecting point is recognized as the direction of a Cherenkov ring.

5.2 Ring Counting

With the knowledge of the vertex position, the Ring Counting algorithm determines the number of Cherenkov rings and the direction of each ring.

This algorithm starts from the ring candidate search. First, the expected charge from the Cherenkov ring found by the vertex fitting (see Section 5.1) is subtracted for each PMT. Then we use a pattern recognition method called "Hough transformation" [89]. Figure 5.2 illustrates the basic idea of the ring candidate search. Here, we consider a spherical coordinate centered on the vertex position so that we can represent a directions of each Cherenkov ring or PMT as a point on a sphere. Assuming that the Cherenkov opening angle is 42°, possible ring direction estimated by a certain PMT draws the virtual circle with its center being at this PMT and its radius corresponding to 42° opening angle (thin circles in Figure 5.2). The most intersecting point is recognized as the direction of a Cherenkov ring.

In practice, the Hough space is made by using the polar angle Θ and the azimuthal angle Φ which are measured from the reconstructed vertex. Then, instead of drawing virtual circles, the charge of a hit PMT is mapped onto points (Θ, Φ). If the opening angle of the point from the PMT is θ, this point is given the charge with the weight by the expected p.e.s distribution function $f(\theta)$. Actually, the p.e.s distribution simulated for a 500 MeV/c electron are used as $f(\theta)$. This operation is done about all hit PMTs. By this Hough transformation, ring center candidates are visible as the peaks on the charge map. Figure 5.3 shows a typical charge map.

Next, the ring candidates are tested using a likelihood method. Suppose N rings are already found in an event, the test of the $(N+1)$-th ring candidate is carried out by comparing the likelihood (L_{N+1}) for the assumption of the event having $N+1$ rings including this ring candidate

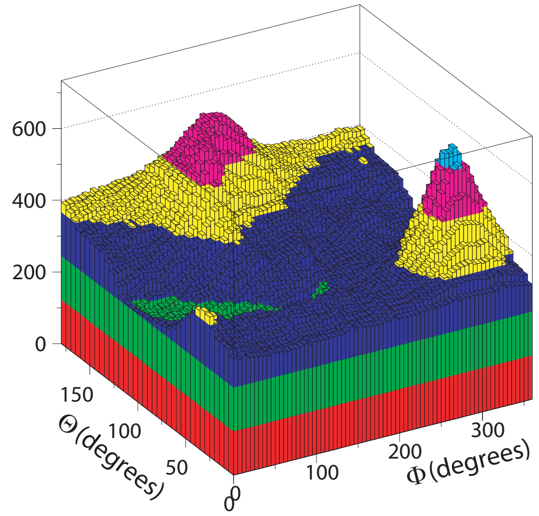

Figure 5.3: A typical charge map. Peaks correspond to the directions of Cherenkov rings from the vertex position.

with the likelihood (L_N) for the assumption of the event having only N rings already found. The likelihood function for the $N+1$ rings assumption is defined as :

$$L_{N+1} = \sum_i \log \left(prob \left(q_i^{\mathrm{obs}} \, , \, \textstyle\sum_{n=1}^{N+1} \alpha_n \cdot q_{i,n}^{\mathrm{exp}} \right) \right) \tag{5.9}$$

where summation is made over the PMTs inside $N+1$ Cherenkov rings. q_i^{obs} is the observed p.e.s of i-th PMT, $\alpha_n \cdot q_{i,n}^{\mathrm{exp}}$ is the expected p.e.s of the i-th PMT from the n-th ring and scale factors α_n (n=1 , $\cdots$, $N+1$) are selected to maximize L^{N+1}. The probability function is defined as :

$$prob \left(q_{\mathrm{obs}} \, , \, q_{\mathrm{exp}} \right) = \begin{cases} \dfrac{1}{\sqrt{2\pi}\,\sigma} \exp \left(- \dfrac{(q_{\mathrm{obs}} - q_{\mathrm{exp}})^2}{2\,\sigma^2} \right) & (\text{for } q_i^{\mathrm{exp}} > 20 \text{ p.e.}) \\ \text{convolution of single p.e. distribution} & \\ \text{and a Poisson distribution} & (\text{for } q_i^{\mathrm{exp}} < 20 \text{ p.e.}) \end{cases} \tag{5.10}$$

where σ is the resolution for q_{exp}.

If there are no candidate which satisfies $L^{N+1} \geq L^N$, the number of rings of this event is finally determined to N. For the ring candidates with $L^{N+1} \geq L^N$, the following four evaluation functions are calculated :

F_1 : The difference $L(N+1) - L(N)$ corrected for the total p.e.s.

F_2 : The average of the expected p.e.s from (N+1)-th ring, Q_{edge} , calculated over the PMTs which are located on the (N+1)-th ring but off the others.

F_3 : The average of the expected p.e.s from $(N+1)$-th ring, Q_{out} , calculated over the PMTs which are located outside the $(N+1)$-th ring and off the others. The difference $Q_{\text{edge}} - Q_{\text{out}}$ is used.

F_4 : The residual p.e.s from the expected p.e.s with the N rings assumption are used. The total amount of the residual p.e.s is calculated as $|\sum q_i^{\text{res}} \cdot \overrightarrow{e_i}|$, where $\overrightarrow{e_i}$ is a unit vector from the reconstructed vertex to the i-th PMT.

These evaluation functions have large values if the candidate is probable. The final evaluation function F is the linear sum of F_1, F_2, F_3 and F_4 with some weights. If there are no candidate which satisfies $F \geq 0$, the number of rings of this event is finally determined to N. If there exists a ring candidate which satisfies $F \geq 0$, it is regarded as the $(N+1)$-th ring and the ring candidate search starts for the $(N+2)$-th ring.

The performance of our Ring Counting algorithm is examined by applying it to atmospheric neutrino Monte Carlo events. The efficiency of single-ring identification for the quasi-elastic scattering events producing a lepton with 1.0 GeV/c momentum is estimated to be 96%.

The efficiency of two-rings identification for the NC induced FC events producing a π^0 and no charged particle is estimated to be 59%. It depends strongly on the produced π^0 momentum as described in Section 6.2.

5.3 Particle Identification

The Particle Identification (PID) program classifies Cherenkov rings into two types, a showering type (e-like) and a non-showering type (μ-like). The Cherenkov ring from an electron or a gamma-ray has a diffuse edge, because such a ring is made of Cherenkov photons from multiple particles produced in an electro-magnetic shower. On the other hand, a muon or a pion produced a sharper ring caused by a single charged particle. The PID program uses this difference of Cherenkov ring patterns. In addition, as a muon or a pion has a lower momentum, its β gets smaller apart from 1, resulting in a smaller the opening angle. In case of electrons or gamma-rays, the same thing does not occur until very low energies. The PID program also uses this difference of opening angles.

Expected Charge Distribution for an Electron

The expected charge distribution for an electron is made by the Monte Carlo simulation. In practice, we create the angular distribution of the expected p.e.s in the 50cm-diameter circular area on the 16.9m-radius virtual spherical surface centered on the vertex position, which is given as a function of the opening angle and the electron momentum, $Q^{\text{exp}}(p, \theta)$.

Using the $Q^{\text{exp}}(\theta, p)$, expected p.e.s for the i-th PMT from the n-th ring is calculated as :

$$q_{i,n}^{\text{direct}}(e) = \alpha_n(e) \times Q^{\text{exp}}(p_n, \theta_{i,n}) \times \left(\frac{R}{r_i}\right)^{1.5} \times \frac{1}{\exp(r_i/L)} \times f(\Theta_i) \qquad (5.11)$$

where

$q_{i,n}^{\text{direct}}(e)$: expected p.e.s for the i-th PMT from the n-th ring with assumption that the particle producing the n-th ring is an electron

$\alpha_n(e)$: normalization factor

$\theta_{i,n}$: opening angle between the i-th PMT direction and the n-th ring direction

r_i : distance from the vertex to the i-th PMT

R : radius of the virtual sphere, 16.9 m

L : light attenuation length in water

$f(\Theta_i)$: correction function for the PMT acceptance as a function of the photon incident angle Θ_i

The factor $(R/r_i)^{1.5}$ comes from the distance dependence of the light intensity.

Expected Charge Distribution for a Muon

The expected p.e.s distribution for a muon can be analytically calculated by :

$$q_{i,n}^{\text{direct}}(\mu) = \left(\alpha_n(\mu) \times \frac{\sin^2 \theta_{i,n}}{r_i \left(\sin\theta_{i,n} + r_i \cdot \frac{d\theta}{dx}\big|_{x=x_i} \right)} + q_{i,n}^{\text{knock}} \right) \times \frac{1}{\exp(r_i/L)} \times f(\Theta_i) \qquad (5.12)$$

where

$q_{i,n}^{\text{direct}}(\mu)$: expected p.e.s for the i-th PMT from the n-th ring with assumption that the particle producing the n-th ring is a muon

$\alpha_n(\mu)$: normalization factor

$q_{i,n}^{\text{knock}}$: expected p.e.s. for the i-th PMT from knock-on electrons

x : distance from the initial vertex position along the muon trajectory

$x_{i,n}$: distance from the initial vertex position to the muon position where Cherenkov photons are emitted toward the i-th PMT

θ : Cherenkov opening angle of the muon traversing at x

$\theta_{x_{i,n}}$: Cherenkov opening angle of the muon traversing at $x = x_{i,n}$

Here, the term $\sin^2\theta$ comes from the angular dependence of the Cherenkov light intensity. The term $r(\sin\theta + r(d\theta/dx))$ comes from the area where Cherenkov photons are emitted to. As shown in Figure 5.4, Cherenkov photons are emitted to the area of $2\pi r \sin\theta(dx \sin\theta + r d\theta)$ while a muon travels the distance of dx with the Cherenkov angle decreasing due to the ionization loss.

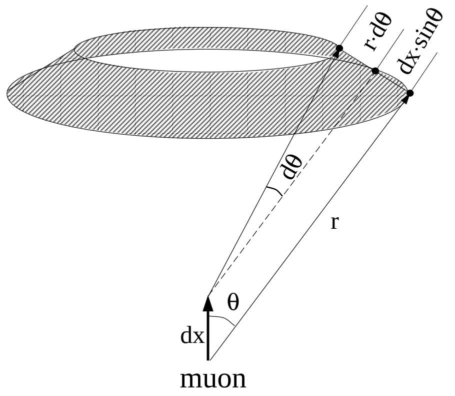

Figure 5.4: Schematic view of the Cherenkov radiation from a muon. Cherenkov photons are emitted to the area of $2\pi r\sin\theta(dx\sin\theta + rd\theta)$ while a muon travels the distance of dx.

Expected Charge Distribution for Scattered Lights

Scattered photons are distinguished from direct photons by using their arrival times :

$$\begin{array}{rcl} t_0 - 30\,\mathrm{nsec} < t_i < t_0 + 2\sigma_i + 5\,\mathrm{nsec} & : & \mathrm{directphotons} \\ t_0 + 2\sigma_i + 5\,\mathrm{nsec} < t_i & : & \mathrm{scatteredphotons} \end{array} \tag{5.13}$$

where t_i is the TOF subtracted hit time of the i-th PMT, t_0 is the peak position in the TOF subtracted hit time distributions for all PMTs and σ_i is the measured timing resolution as a function of detected p.e.s. Thus $q_{i,n}^{\mathrm{scatt}}$, the expected p.e.s distribution from scattered lights, is estimated.

Finally, the expected total p.e.s for the i-th PMT from an electron or a muon producing the n-th ring are calculated by :

$$q_{i,n}^{\mathrm{exp}}(e \text{ or } \mu) = q_{i,n}^{\mathrm{direct}}(e \text{ or } \mu) + q_{i,n}^{\mathrm{scatter}} \tag{5.14}$$

Estimation of the Particle Types

The likelihood definition of the n-th ring using the Cherenkov ring patterns is :

$$L_n(e \text{ or } \mu) = \prod_i prob\left(q_i^{\mathrm{obs}}\ ,\ q_{i,n}^{\mathrm{exp}}(e \text{ or } \mu) + \sum_{n'\neq n} q_{i,n'}^{\mathrm{exp}}\right) \tag{5.15}$$

where the product is made over the PMTs inside the n-th ring. q_i^{obs} is the observed p.e.s of i-th PMT, $q_{i,n}^{\mathrm{exp}}(e \text{ or } \mu)$ is the expected p.e.s from the n-th ring with an electron assumption or a muon assumption (Equation (5.14)), $q_{i,n'}^{\mathrm{exp}}$ is the expected p.e.s from the n'-th ring without the particle type assumption and *prob* is the same probability function as used in the Ring Counting procedure (Equation (5.10)). $q_{i,n}^{\mathrm{exp}}(e)$ ($q_{i,n}^{\mathrm{exp}}(\mu)$) is selected to maximize the $L_n(e)$ ($L_n(\mu)$) by changing the direction and the opening angle of the n-th Cherenkov ring. Then the likelihood using the ring pattern informations is translated into a χ^2 parameter :

$$\chi_n^2(e \text{ or } \mu) = -2 \log L_n(e \text{ or } \mu) - \text{constant} \tag{5.16}$$

The probability of the q_i^{obs} detection is calculated as :

$$P_n^{\mathrm{pattern}}(e \text{ or } \mu) = \exp\left(-\frac{\left(\chi_n^2(e \text{ or } \mu) - \min\left[\chi_n^2(e)\,,\, \chi_n^2(\mu)\right]\right)^2}{2\,\sigma_{\chi_n^2}^2}\right) \tag{5.17}$$

The resolution of the χ^2 distribution is approximated by $\sigma_{\chi_n^2} = \sqrt{2N}$, where N is the number of PMTs used for the likelihood calculation (Equation (5.15)).

The probability using the Cherenkov opening angle is calculated as :

$$P_n^{\mathrm{angle}}(e \text{ or } \mu) = \exp\left(-\frac{\left(\theta_n^c - \theta_n^{\mathrm{exp}}(e \text{ or } \mu)\right)^2}{2\,(\delta\theta_n)^2}\right) \tag{5.18}$$

where $\theta_n^c \pm \delta\theta_n$ is the reconstructed opening angle of n-th ring. $\theta_n^{\mathrm{exp}}(e \text{ or } \mu)$ is the expected opening angle of n-th ring , which is calculated from the estimated momentum with an electron assumption or a muon assumption.

Finally, the total probability is :

$$P_n(e) = P_n^{\mathrm{pattern}}(e) \times P_n^{\mathrm{angle}}(e) \tag{5.19}$$

$$P_n(\mu) = P_n^{\mathrm{pattern}}(\mu) \times P_n^{\mathrm{angle}}(\mu) \tag{5.20}$$

For a single-ring event, the ring with $P_1(e) > P_1(\mu)$ ($P_1(e) < P_1(\mu)$) is identified as e-like (μ-like). However, for a multi-ring event, we use the probability by the ring pattern information (P_n^{pattern}) only. This is because the estimation of the opening angle works relatively worse in case of a multi-ring event.

The performance of our Particle Identification algorithm is examined by applying it to atmospheric neutrino Monte Carlo events. In Figure 5.5, the distributions of the PID parameter $P \equiv \sqrt{-\log P_1(\mu)} - \sqrt{-\log P_1(e)}$ are shown for FC single-ring events. The peaks in the μ-like region and the e-like region are clearly separated, and misidentifying probabilities are estimated to be 1.2 % for ν_μ CCq.e. events and 0.6 % for ν_e CCq.e. events.

Figure 5.6 shows the PID parameter distributions for the FC two-ring events from the NC interactions with a π^0 and no charged particle in the final states. Both rings of two gamma-rays as decay products of a π^0 are well identified as e-like. The misidentifying probability for the first ring and the second ring is estimated to be 2.9 % and 1.9 %, respectively.

5.4 Precise Vertex Fitting

The vertex fitting algorithm described in Section 5.1 uses only timing information, resulting in a relatively worse resolution in the longitudinal direction for single-ring events. This is because a vertex shift along the particle direction changes TOFs evenly for all the hit PMTs, and the goodness of the fitting doesn't change so much.

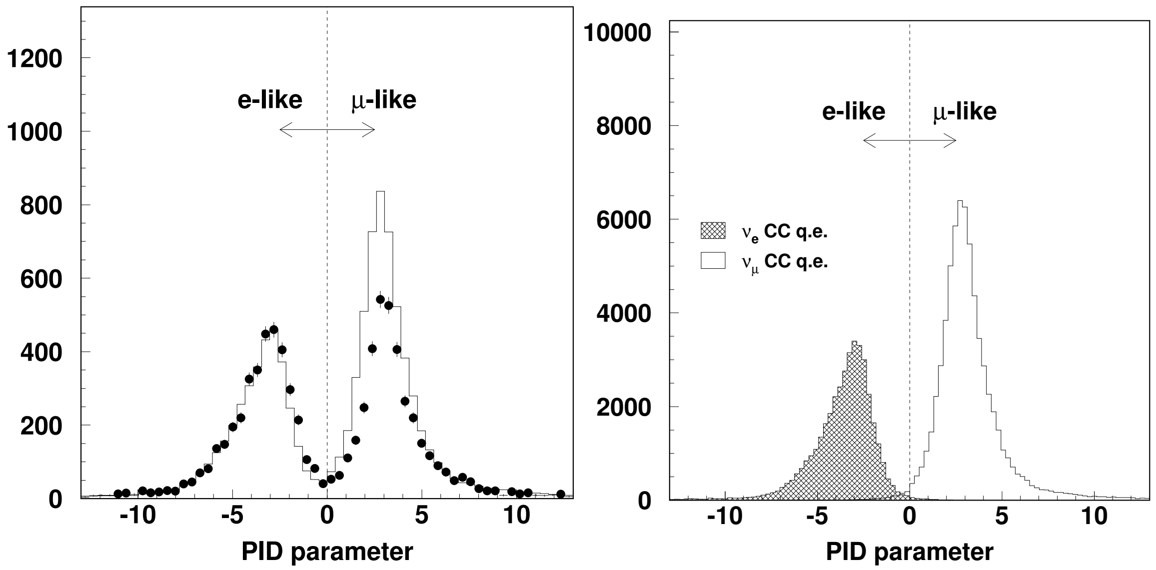

Figure 5.5: The distribution of the PID parameter for FC single-ring events. The dots in the left figure represent the data with statistical error, the histogram in the left figure represents the atmospheric neutrino MC expectation, and the right figure is for MC events of CC quasi-elastic scatterings.

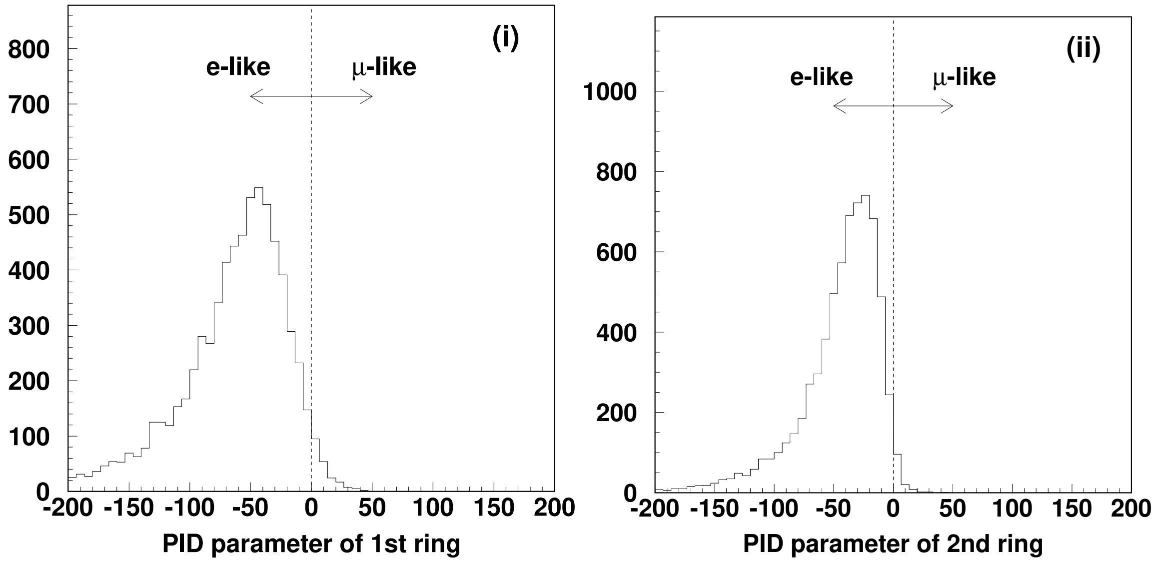

Figure 5.6: The PID parameter distributions of the FC two-ring events from the NC interactions with a π^0 and no charged particle in the final states, (i) for the first ring and (ii) for the second ring in case the first ring is e-like.

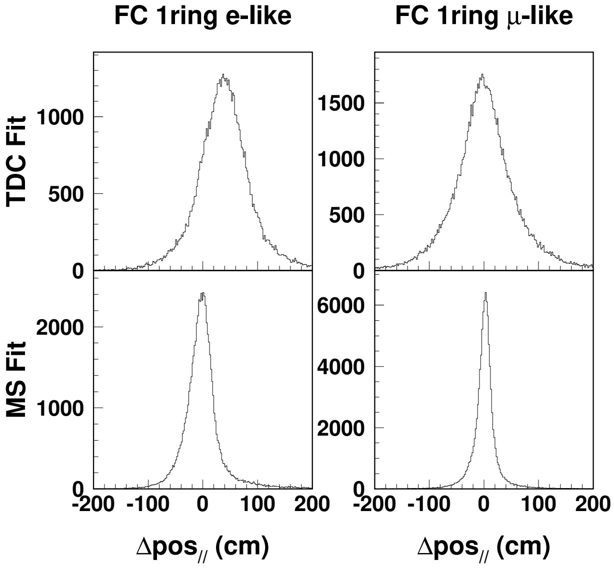

Figure 5.7: The vertex resolution along the particle direction after applying MS fitter (MS Fit), compared with that of the first stage fitter (TDC Fit).

To obtain a more precisely fitted vertex position, we use another fitting program called MS fitter. First, MS fitter modifies the vertex position in the longitudinal direction by comparing the observed photon distribution with the photon distribution expected from a particle type determined in the PID algorithm. The ring direction is also reconstructed again in this step. After a new vertex position and direction are found, the vertex position is then moved perpendicularly to the particle direction and selected to maximize the estimator G_T used in the TDCfit (Equation (5.8)). This process is iterated until the changes in the vertex position and ring direction become less than 5 cm and $0.5°$, respectively.

The performance of MS fitter is examined by applying it to FC single-ring events in our atmospheric neutrino Monte Carlo sample. Figure 5.7 shows the vertex resolution along the particle direction after applying MS fitter (MS Fit), compared with that of the first stage fitter (TDC Fit). It is clear that MS fitter gives the much better vertex resolutions. As shown in Figure 5.8, after applying MS fitter, the vertex resolution becomes 31cm for single-ring e-like events and 24cm for single-ring μ-like events. The angular resolution is estimated to be $3.4°$ and $1.9°$ for e-like events and μ-like events.

5.5 Momentum Determination

The momentum of each ring is determined by the total charge detected inside a cone with $70°$ of half-angle. Actually, the total observed charge is corrected for the light attenuation in

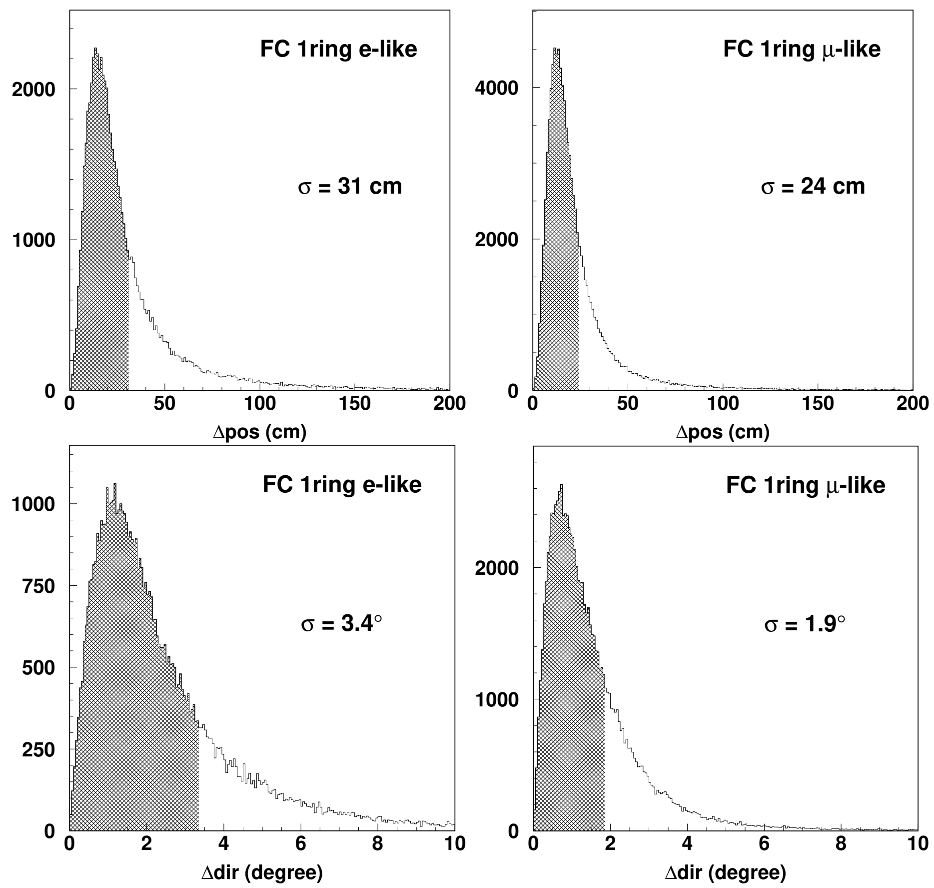

Figure 5.8: The resolution of the reconstructed vertex (upper figures) and direction (lower figures) after applying MS fitter, which is estimated by atmospheric neutrino Monte Carlo.

water and the PMT angular acceptance, like :

$$RTOT_n = \frac{G_{\rm MC}}{G_{\rm data}} \left[\alpha \times \sum_{\substack{\theta_{i,n}<70^\circ \\ -50{\rm nsec}<t_i<250{\rm nsec}}} \left(q_{i,n}^{\rm obs} \times \exp\left(\frac{r_i}{L}\right) \times \frac{\cos\Theta_i}{f(\Theta_i)} \right) - \sum_{\theta_{i,n}<70^\circ} S_i \right] \tag{5.21}$$

where

α	: normalization factor
$G_{\rm data}\,, G_{\rm MC}$	: relative PMT gain parameter for data and MC
$q_{i,n}^{\rm obs}$	: observed p.e.s for the i-th PMT form the n-th ring
$\theta_{i,n}$	: opening angle between the i-th PMT direction and the n-th ring direction
t_i	: TOF subtracted hit time of the i-th PMT
L	: light attenuation length in water
r_i	: distance from the vertex position to the i-th PMT
$f(\Theta_i)$	: correction function for the PMT acceptance as a function of the photon incident angle Θ_i
S_i	: expected p.e.s of scattered light for the i-th PMT

Summation is made by the observed p.e.s inside the time window, from -50 nsec to +250 nsec with the peak of the TOF subtracted hit time distribution set to 0 nsec. This is for rejecting the effect of Michel electrons. As for L in Equation (5.21), in case of momentum reconstruction for observed events, we use the water attenuation length continuously measured using cosmic ray through-going muons to correct the time variation (see Section 2.3.4).

The relations between RTOT and the momentum for electrons and muons are calculated using the Monte Carlo simulation, as shown in Figure 5.9. Using these relationships, RTOT is translated to the momentum of an electron for e-like ring and that of a muon for μ-like ring.

The reconstructed momentum resolution for single-ring electrons is approximately described as ($0.5 + 2.5/\sqrt{P_e({\rm GeV/c})}$) % and that for single-ring muons is about 3 %.

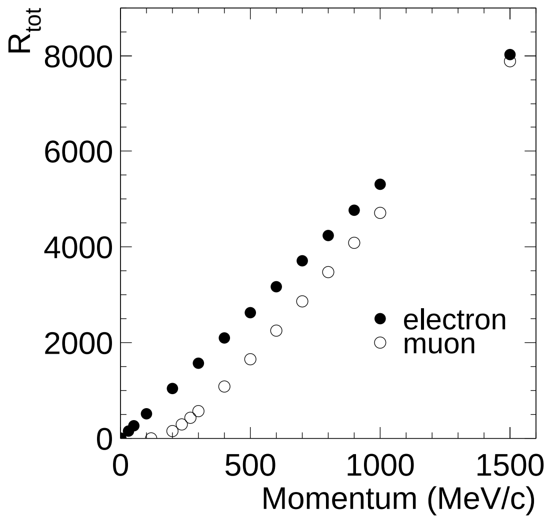

Figure 5.9: The relations between RTOT and the momentum for electrons and muons made by the Monte Carlo simulation.

Chapter 6

π^0/μ Measurement in Super-Kamiokande

6.1 Fully Contained Sample

The analysis in this thesis uses fully contained events observed in a 1489.2 live days exposure of Super-Kamiokande. A full-detector Monte Carlo simulation of atmospheric neutrino events equivalent to 70.3 live years is processed by the same data reduction and event reconstruction steps.

The final sample of FC events is made by the following criteria :

(1) Visible energy (E_{vis}) > 30 MeV

(2) Number of hit PMTs in the largest OD hit cluster (N_{hitac}) < 10

(3) Distance from the reconstructed vertex to the nearest wall (D_{wall}) > 200 cm

(4) $p_e > 100$ MeV/c for 1-ring e-like events, $p_\mu > 200$ MeV/c for 1-ring μ-like events

Criterion (1) is required to eliminate low energy background. E_{vis} is defined as the sum of the energy assuming that all rings are e-like. Criterion (2) makes sure that FC events have no clear entering/exiting point of charged particles in the outer detector region. Criterion (3) is used to reduce possible contamination from entering events, and also to avoid using events of worse reconstruction quality. The fiducial volume determined by this cut is 22.5 kt. Figure 6.1 shows vertex distributions for FC events which satisfy the cuts (1)-(2). The dots represent the data with statistical errors, and the histograms show the atmospheric neutrino Monte Carlo expectation for no oscillations normalized to the live time. The arrows in each figure show the fiducial cut (3). We can see that the contamination from cosmic ray muons into the fiducial volume is negligible.

A total of 11872 FC events is obtained after these cuts. Expected number of FC events normalized to the live time is 14349.9. Table 6.1 summarizes the number of events in the final FC sample. Note that neutrino oscillations are not taken into account for all the Monte Carlo predictions in this chapter.

The number of Cherenkov rings distribution and the visible energy (E_{vis}) distributions for the final FC sample are shown in Figure 6.2 and Figure 6.3, respectively.

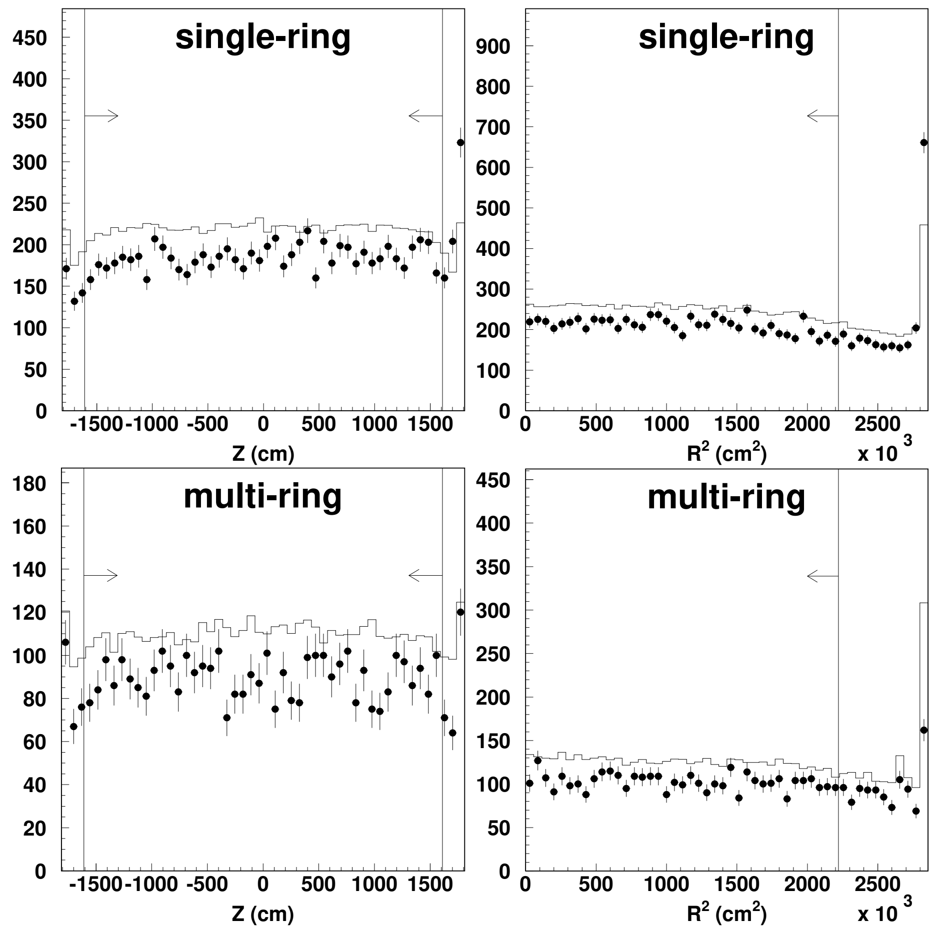

Figure 6.1: Vertex distributions for FC events which satisfy the cuts (1)-(2) (see text). Z distributions of the events with $R < 14.9$m are shown for single-ring events and multi-ring events (left). R^2 distributions of the events with $|Z| < 16.1$m are shown for single-ring events and multi-ring events (right). Here, R $(= \sqrt{X^2 + Y^2})$ is the distance from the tank axis to the reconstructed vertex. The arrows show the fiducial cut (3).

	Data	Monte Carlo
1 ring	7883	9460.8
e-like	4038	3788.8
μ-like	3845	5672.0
2 rings	2284	2738.7
$\geq$3 rings	1705	2150.4
Total	11872	14349.9

Table 6.1: Summary of observed FC events and the Monte Carlo prediction normalized to the livetime.

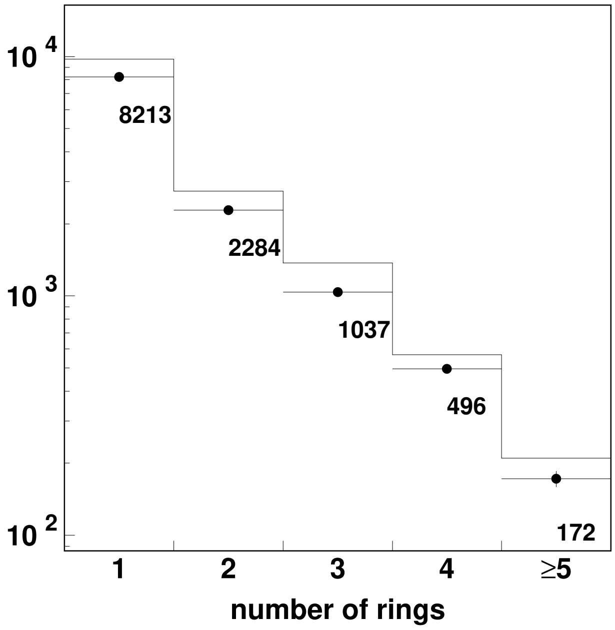

Figure 6.2: The number of rings distribution for observed FC events (dots and numbers) and the Monte Carlo prediction (histogram) normalized to the livetime.

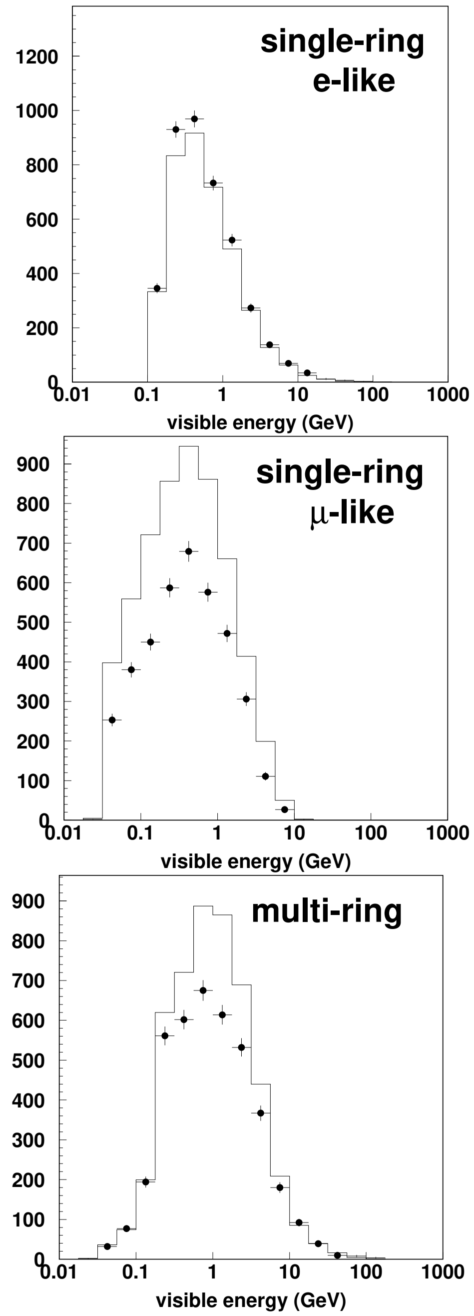

Figure 6.3: The visible energy (E_{vis}) distributions for observed FC events (dots) and Monte Carlo predictions (histograms) normalized to the livetime.

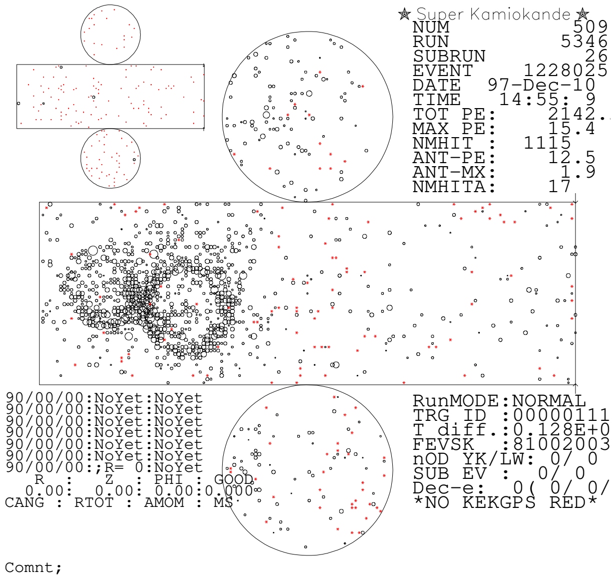

Figure 6.4: A typical event in the π^0 sample.

6.2 π^0 Events Selection

To extract the π^0 events from the final FC sample, the following selection criteria are used :

(A) the number of rings is 2

(B) both rings have a showering type (= e-like) particle identification

(C) no decay electron

(D) 85 MeV/c^2 < the invariant mass of 2 e-like rings ($M_{\gamma\gamma}$) < 185 MeV/c^2

Figure 6.4 shows a typical event in this π^0 sample. Criteria (A) and (B) are to select two γ-rays as decay products of π^0s. Criterion (C) is used to reject the events with the invisible muons and charged pions below the Cherenkov thresholds. Figure 6.5 shows the invariant mass distribution of events after the cuts (A)-(C). We can see a clear π^0 mass peak.

The MC peak position of 141.2 ± 0.2 MeV/c^2 is shifted relative to the data peak position of 145.6 ± 0.8 MeV/c^2. This 3 % difference is used for quoting our systematic uncertainty of the energy scale (see Section 2.3.6). In addition, both peaks are shifted with respect to the nominal value of the π^0 mass, 135.0 MeV/c^2. This shift is mainly due to the following two reasons. First, when a π^0 is produced in ^{16}O nucleus, the remaining nucleus is often left in an excited state and then emit de-excitation γ-rays which add light (*i.e.* energy) to an event. Second, the two γ-rays as decay products of a π^0 do not convert into electromagnetic showers right after the decay. Therefore the reconstructed vertex tends to be pulled toward the particle direction. This causes the reconstructed opening angle of the two γ-rays to be slightly larger than the true opening angle, resulting in the larger π^0 invariant mass.

Figure 6.6 shows the number of events after applying each selection criterion for data and neutrino MC. The detection efficiency by the above criteria is estimated to be about 50 % for the

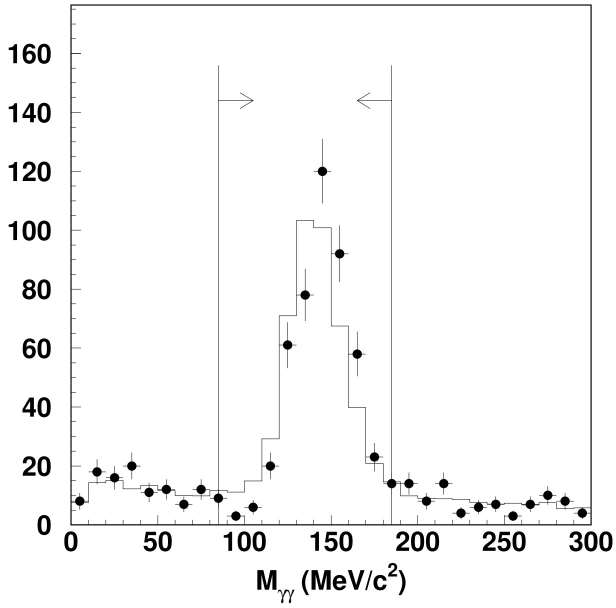

Figure 6.5: The invariant mass distribution of 2 e-like rings ($M_{\gamma\gamma}$) for events which satisfy the cuts (A)-(C) (see text). The dots represent the data with statistical errors. The histogram shows the atmospheric neutrino Monte Carlo expectation for no oscillations normalized to the live time. The arrows show the invariant mass cut (D).

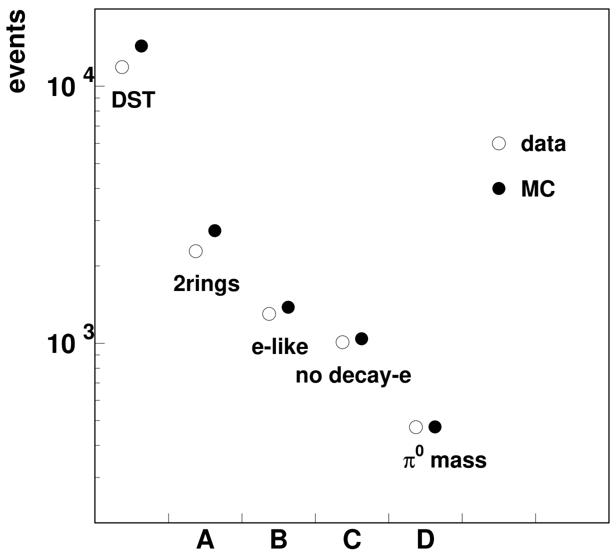

Figure 6.6: The number of events after each selection criterion (see text) for π^0 sample. The open circles represent the data. The numbers for the neutrino MC (filled circles) are normalized to the livetime. DST means the final FC sample.

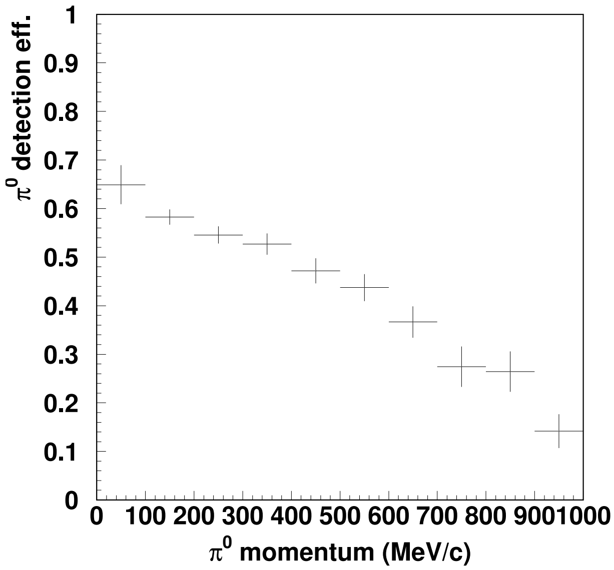

Figure 6.7: The π^0 detection efficiency as a function of its momentum. As the momentum of the produced π^0 becomes larger, the angle of two γ-rays becomes smaller resulting in a the smaller detection efficiency.

		(i) π^0 events		(ii) μ events	
ν_e, $\overline{\nu}_e$ CC		824	(10.1 %)	374	(0.4 %)
	q.e.	332	(4.1 %)	222	(0.2 %)
	single π	311	(3.8 %)	93	(0.1 %)
	coherent π	67	(0.8 %)	10	(0.0 %)
	multi π	109	(1.3 %)	46	(0.0 %)
ν_μ, $\overline{\nu}_\mu$ CC		331	(4.1 %)	93890	(96.0 %)
	q.e.	16	(0.2 %)	66336	(67.8 %)
	single π	215	(2.6 %)	18908	(19.3 %)
	coherent π	9	(0.1 %)	2262	(2.3 %)
	multi π	85	(1.0 %)	5961	(6.1 %)
NC		6987	(85.8 %)	3516	(3.6 %)
	single π	3871	(47.5 %)	1852	(1.9 %)
	coherent π	1726	(21.2 %)	22	(0.0 %)
	multi π	1175	(14.4 %)	1193	(1.2 %)
Total		8142		97780	

Table 6.2: The fraction of the each interaction channel for (i) the π^0 sample and (ii) the μ sample. All the numbers are from the 70.3 live years equivalent Monte Carlo with no oscillations.

neutral current interaction events which have a single π^0 and no charged particles in the final state. The relation between the detection efficiency and π^0 momentum is shown in Figure 6.7. As the momentum of the produced π^0 becomes larger, the angle of two γ-rays becomes smaller resulting in a the smaller detection efficiency.

Table 6.2-(i) shows the fraction of the each interaction channel for the MC π^0 sample. 86 % of the sample is from NC interactions. In particular, NC resonant single π productions make a large (48 %) contribution. In these interactions, a π^0 is produced directly by a decay of a Δ resonance, or by a charge exchange of a produced charged π in a ^{16}O nucleus. 13 % of the π^0 events comes from NC multi π productions where accompanying charged πs are below Cherenkov threshold or absorbed in the nucleus. The CC interaction induced events are mainly from CC single π productions with a charged lepton below Cherenkov threshold, or from ν_e, $\overline{\nu}_e$ CC q.e. interactions which are identified as 2 rings due to a large scatter or a mis-reconstruction.

The distributions of the reconstructed π^0 momentum and zenith angle are shown in Figure 6.8 and Figure 6.9. It can be said that the data distributions are well reproduced by the neutrino MC.

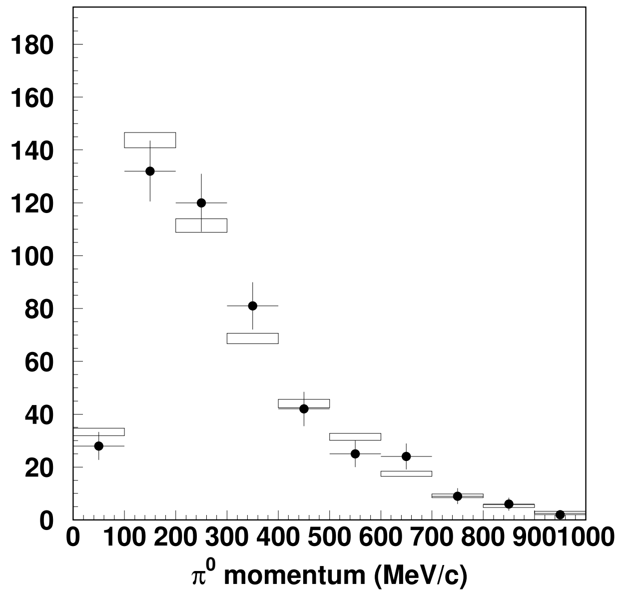

Figure 6.8: The reconstructed π^0 momentum distribution. The dots represent the data with statistical errors. The boxes show the atmospheric neutrino Monte Carlo expectation normalize to the live time. The size of boxes shows statistical errors.

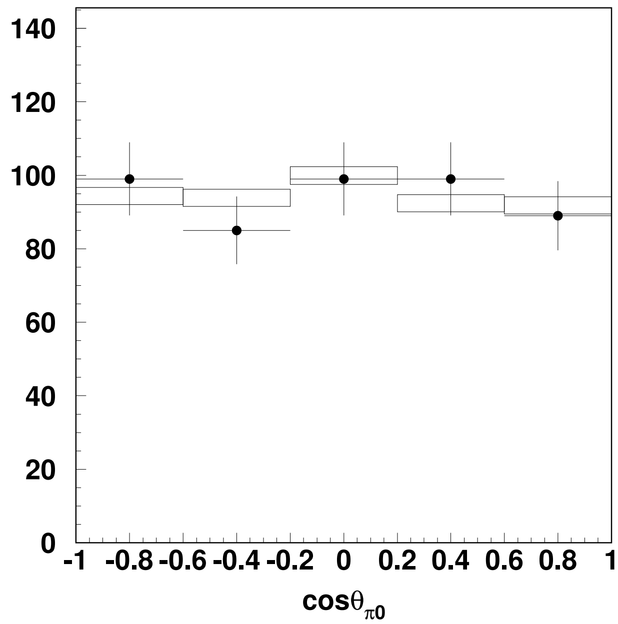

Figure 6.9: The reconstructed π^0 zenith angle distribution. $\cos\theta_{\pi^0} = -1$ ($\cos\theta_{\pi^0} = 1$) indicates upward-going (downward-going) direction.

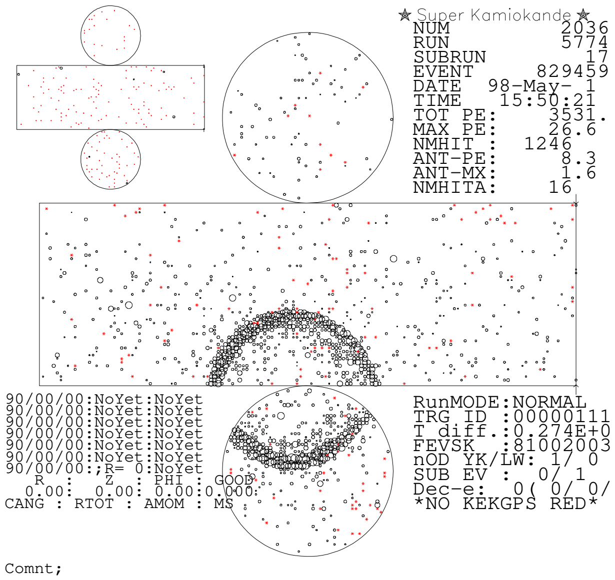

Figure 6.10: A typical event in the μ sample.

6.3 μ Events Selection

The criteria to extract μ events from the final FC sample are :

(a) the number of rings is 1

(b) the ring has a non-showering type (= μ-like) particle identification

Note that this sample contains no events with reconstructed μ momenta less than 200 MeV/c because those events are already rejected in making the final FC sample (see Section 6.1). A typical μ event is shown in Figure 6.10. Figure 6.11 shows the number of events after applying each selection criterion for data and neutrino MC with no oscillations. The main reason for the significantly small numbers of observed μ events is supposed to be neutrino oscillation.

For this μ sample, the MC estimated fraction of the each interaction channel are listed on Table 6.2-(ii). 96 % of the sample comes from CC interactions of ν_μ or $\overline{\nu}_\mu$, where 68 % is due to CC q.e. scatterings and the rest 28 % is from CC π production channels where a π(s) is(are) below Cherenkov threshold or absorbed in the nucleus. The NC interaction induced events are from NC π productions accompanying a charged π above Cherenkov threshold.

Figure 6.12 and Figure 6.13 shows the reconstructed μ momentum distribution and zenith angle distribution. The deficits on the observed data are clearly visible.

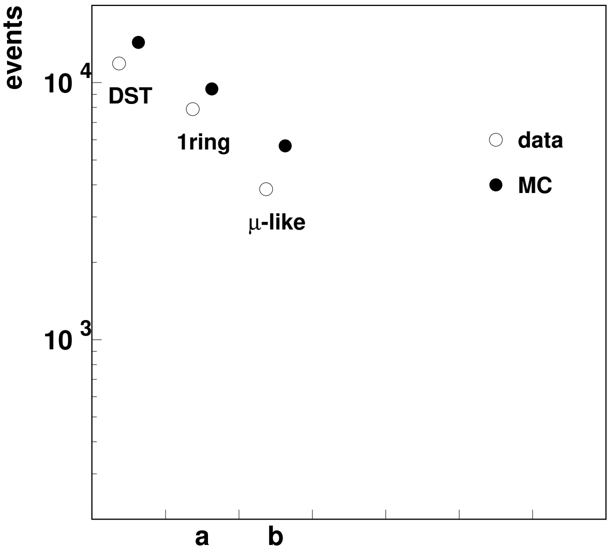

Figure 6.11: The number of events after each selection criterion (see text) for μ sample. Neutrino oscillations are not taken into account for the Monte Carlo prediction.

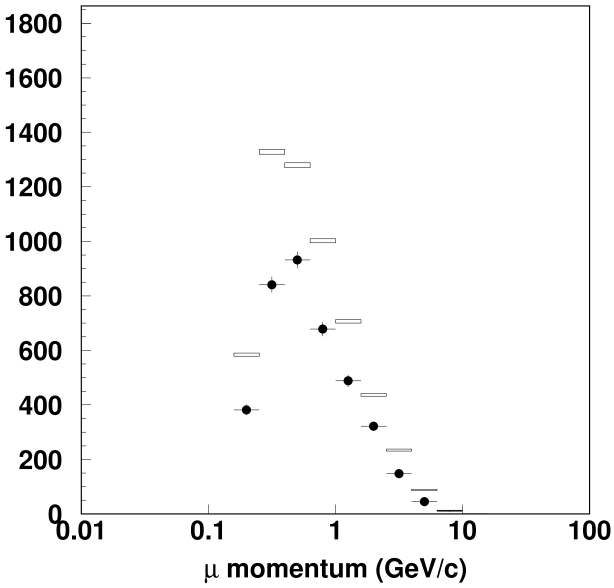

Figure 6.12: The reconstructed μ momentum distribution. The dots represent the data with statistical errors. The boxes show the atmospheric neutrino Monte Carlo expectation normalize to the live time. The size of boxes shows statistical errors.

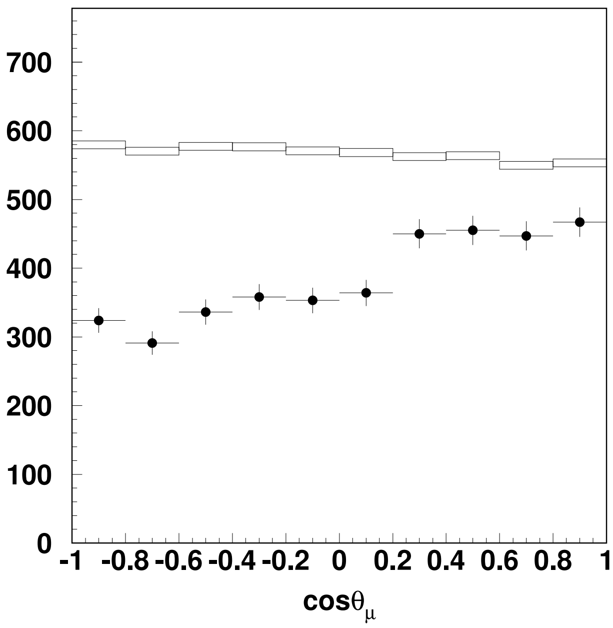

Figure 6.13: The reconstructed μ zenith angle distribution. $\cos\theta_\mu = -1$ ($\cos\theta_\mu = 1$) indicates upward-going (downward-going) direction.

	Data	Monte Carlo
π^0	471	472.3
μ	3845	5672.1

Table 6.3: The number of observed π^0 events and μ events compared with the Monte Carlo prediction normalized to the live time.

6.4 Results

We define the double ratio R_{π^0}, which is defined as :

$$R_{\pi^0} \equiv \frac{(\pi^0/\mu)_{\mathrm{Data}}}{(\pi^0/\mu)_{\mathrm{MC_{no\,osc}}}} \tag{6.1}$$

where π^0 represents the number of π^0 events described in Section 6.2 and μ represents the number of μ events described in Section 6.3. The subscripts " Data " and " $\mathrm{MC_{no\,osc}}$ " indicate the observed data and the Monte Carlo prediction with no oscillations, respectively.

In Table 6.3, the numbers of observed events are shown with the corresponding Monte Carlo predictions. From the real data and the MC with no oscillations, we obtain :

$$R_{\pi^0} = 1.47 \pm 0.07\ (data\ stat.) \pm 0.32\ (sys.) \tag{6.2}$$

The systematic uncertainty on R_{π^0} is estimated to be 20 %. The details of the systematic uncertainty are discussed in the next section.

6.5 Systematic Uncertainty

atmospheric neutrino flux	2 %
cross section	
(neutrino interaction	17 %)
(nuclear effect	7 %)
$\rightarrow$ combined	18 %
event reconstruction	7 %
energy scale	1.4 %
reduction	$<$ 1 %
MC statistics	1 %
total	20 %

Table 6.4: The systematic uncertainties on R_{π^0}

Table 6.4 lists the systematic uncertainties on R_{π^0} due to various sources. First of all, we must consider the uncertainty of the atmospheric neutrino flux. As described in Section 1.1, the flux ratios $(\nu_\mu + \overline{\nu}_\mu)/(\nu_e + \overline{\nu}_e)$, $\nu_\mu/\overline{\nu}_\mu$ and $\nu_e/\overline{\nu}_e$ have 5 % uncertainties. The first one has little effect on the number of π^0 events because the cross section of neutral current interaction is independent of neutrino flavors. However, the number of μ events is sensitive to this flavor ratio uncertainty. The effect on R_{π^0} is estimated to be 1.8 %. The second and the last affect both samples little, giving 0.5 % and 0.3 % uncertainties on R_{π^0}, respectively. The three combined are about 2 %.

The dominant systematic uncertainty on R_{π^0} is due to the cross section uncertainty for neutrino interactions producing π^0 events. The absolute cross sections for quasi-elastic scatterings, single-pion productions, coherent pion productions and multi-pion productions are only known with accuracy of 10 %, 30 %, 30 % and 40 % around 1 GeV neutrino energy region, respectively. There also exists the 20 % uncertainty on the NC/CC cross section ratio for each pion production channel. The error on R_{π^0} is calculated for each by varying the absolute cross section or the cross section ratio by the nominal uncertainty, and listed in Table 6.5. The largest error comes from the uncertainty of the single-pion production cross section due to its largest fraction among the π^0 production channels (see Table 6.2). The combined error is about 17 %.

As for the uncertainties related to the event reconstruction and the pion nuclear effect, we can take over the values calculated in the early stage of this type of analysis [90] because the simulation programs related to those items haven't largely been changed. Simulated events were manually fitted for each ring and compared with the vertices, rings and particle identifications determined by the automatic algorithm, resulting in about 7 % uncertainty on R_{π^0}. The systematic error due to the uncertainty of the pion nuclear effect was estimated to be about 7 % by changing the π^0 mean free path in oxygen by 50 %.

interaction channel	uncertainty		error on R_{π^0}
quasi-elastic	CC	10 %	6.7 %
single π	CC+NC	30 %	10.5 %
	CC/NC	20 %	7.8 %
coherent π	CC+NC	30 %	6.0 %
	CC/NC	20 %	3.1 %
multi π	CC+NC	40 %	3.9 %
	CC/NC	20 %	2.2 %
total			16.8 %

Table 6.5: The cross section uncertainties for each interaction channel and their effect on R_{π^0}

The uncertainty on the absolute energy scale also affects R_{π^0}. Since the energy scale is uncertain to $\pm 3\,\%$, the reconstructed momenta for MC events are scaled by $\pm 3\,\%$ and the change on R_{π^0} is estimated. The assigned error is 1.4 %.

Finally, the total systematic uncertainty is estimated to be about 20 %. As discussed later in Chapter 9, the uncertainty of 20 % is of the same order of the predicted difference between $\nu_\mu \leftrightarrow \nu_\tau$ assumption and $\nu_\mu \leftrightarrow \nu_s$ assumption at the Super-Kamiokande's best fit oscillation parameters $(\sin^2 2\theta, \Delta m^2) = (1.00,\ 2.5{\times}10^{-3}\ \mathrm{eV}^2)$.

In order to reduce the systematic uncertainty on R_{π^0} for a $\nu_\mu \leftrightarrow \nu_\tau$ vs. $\nu_\mu \leftrightarrow \nu_s$ analysis of Super-Kamiokande atmospheric neutrinos, we have made a measurement of R_{π^0} at the 1kt water Cherenkov detector using the K2K neutrino beam. We report on this measurement in the following chapters.

Chapter 7

K2K Experiment and 1kt Water Cherenkov Detector

7.1 K2K Experiment

7.1.1 Overview

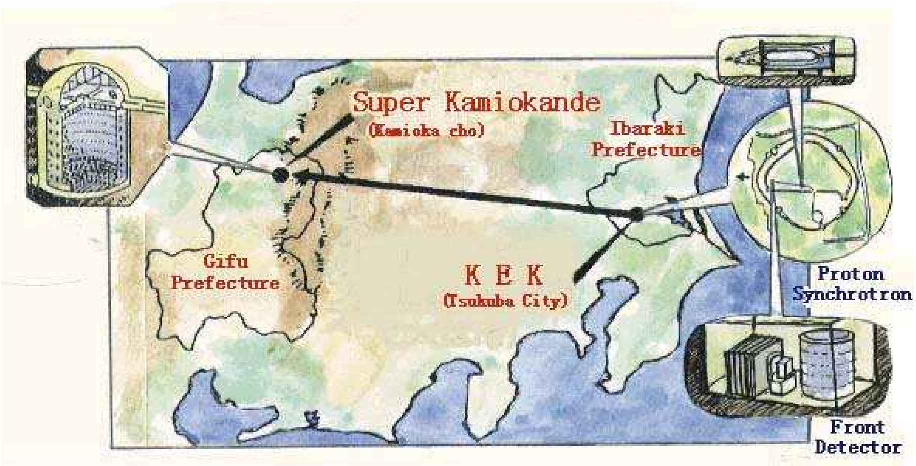

Figure 7.1: A schematic view of the K2K experiment.

The KEK to Kamioka long baseline neutrino oscillation experiment (K2K) is the first earth-scale baseline experiment using accelerator-produced neutrinos. The K2K experiment aims to confirm the existence of neutrino oscillations discovered by atmospheric neutrino experiments, and to measure oscillation parameters more accurately.

A schematic view of the K2K experiment is shown in Figure 7.1. K2K uses almost pure ν_μ beam created using the 12GeV proton synchrotron accelerator at the High Energy Accelerator Research Organization (KEK) in Tsukuba City, Ibaraki Prefecture, Japan. Neutrinos are generated by decay in flight of many charged pions, which arise in collisions between accelerated protons and a target. The beam is steered through the earth toward Super-Kamiokande at a

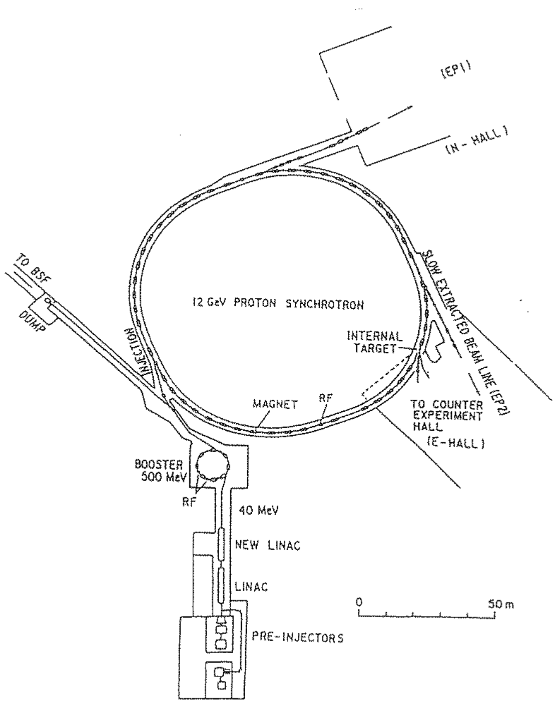

Figure 7.2: A schematic view of the KEK 12 GeV Proton Synchrotron.

distance of 250 km. Since the mean energy of beam neutrinos is about 1.3 GeV, K2K has the sensitivity to Δm^2 of $10^{-2} \sim 10^{-3}\mathrm{eV}^2$ assuming the large mixing.

In order to measure the flux of neutrinos before oscillations, some near detectors are placed at 300 m downstream of the target. Given a plenty of neutrino events, these near detectors are also useful for us to study neutrino interactions.

7.1.2 Neutrino Beam Line

KEK 12 GeV Proton Synchrotron

A schematic view of the KEK 12 GeV Proton Synchrotron (KEK-PS) is shown in Figure 7.2. More than 6×10^{12} protons per cycle are accelerated up to 12 GeV. Accelerated protons are then extracted in a fast extraction mode using kicker, septum and bump magnets. Each beam spill has 9 bunches in 1.1 μsec spill length, and the repetition cycle is 2.2 sec. A detailed description can be found in Ref.[91].

Primary Proton Beam Transport Line

Figure 7.3 shows a schematic view of a neutrino beam-line after 12 GeV-PS. The extracted proton beam going in the north direction is bent about 90° to the west by north, toward Super-Kamiokande, through the arc section of the beam-line containing 61 quadrupole magnets and 44 dipole magnets.

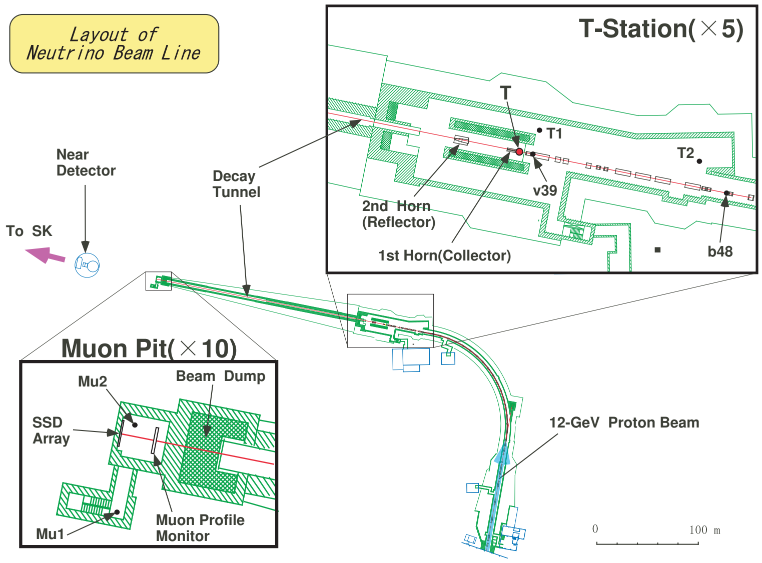

Figure 7.3: A schematic view of a neutrino beam-line after 12 GeV-PS.

Target and Focusing Horn Magnet

The target station is located at the rear end of the arc section. A steering magnet placed just before the target is used for pointing the proton beam toward the Super-Kamiokande direction, about 1° downward from the horizontal level.

Figure 7.4 shows a schematic view of the magnetic horn system. Two magnetic horns are employed to focus π^+'s as parent particles of ν_μ's. The first horn, like a cylinder of 0.70 m in diameter and 2.37 m in length, is equipped with the target for the proton beam. The second horn, also like a cylinder of 1.65 m in diameter and 2.76 m in length, is placed at 8 m downstream from the first horn. The target and the horns are made of aluminum alloy. The target is also cylindrical shaped with a diameter of 30 mm and a length of 66 cm.

The horns are driven with 250 kA pulsed current of 2 msec width at regular intervals of 2.2 sec, which is synchronized with the proton beam extraction. The strength of the magnetic field created by the first horn is calculated as :

$$B(\text{kGauss}) = \frac{I(\text{kA})}{5.0 \cdot R(\text{cm})} \tag{7.1}$$

where I is the horn current and R is a distance from the beam center. This magnetic field focuses the positive charged particles, mostly π^+'s, and sweeps out the negative charged particles. The capability of the horn system is shown in Figure 7.5. The simulated neutrino flux at the SK site with 250 kA horn current is more than 22 times as large as that with zero horn current.

Protons are also focused by the magnetic field of the first horn, resulting in higher targeting efficiency.

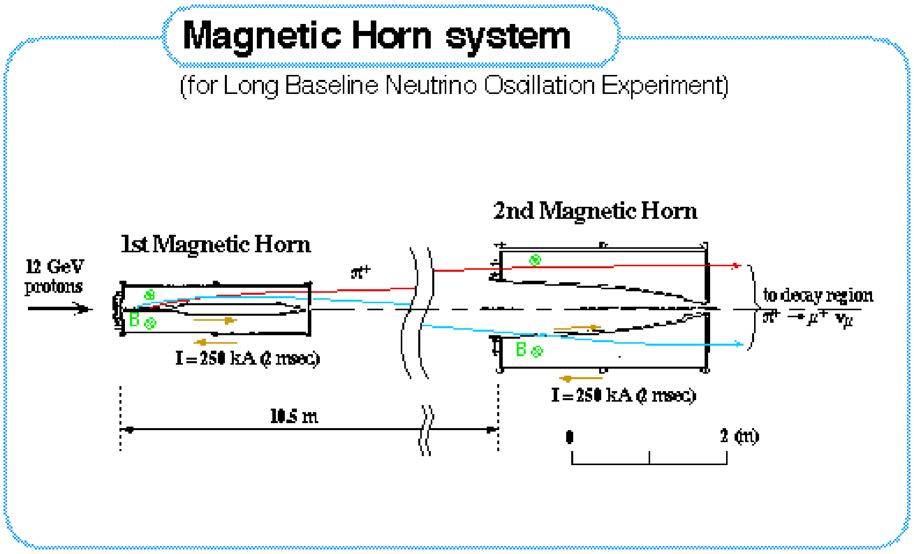

Figure 7.4: The magnetic horn system.

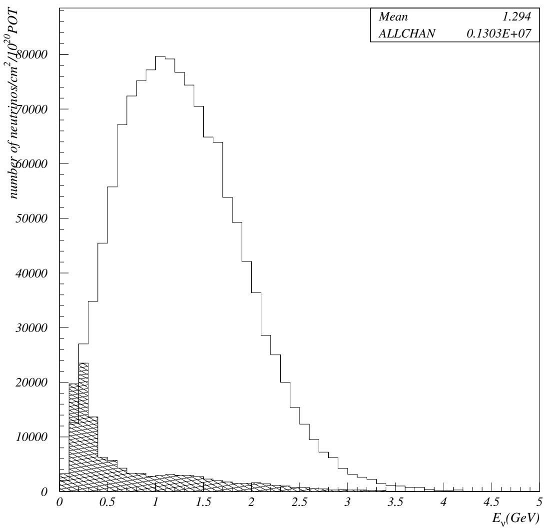

Figure 7.5: The simulated neutrino flux at the SK site with 250 kA horn current (open histogram) and that with zero horn current (hatched histogram).

Decay Tunnel and Beam Dump

Generated pions fly into a cylindrical decay tunnel of 200 m in length. The diameter of the decay tunnel is 1.5 m in the most upstream 10 m region, 2.0 m in the following 90 m region, and 3.0 m in the last 100 m region. In this decay tunnel, a pion decays in flight into a muon and a neutrino :

$$\pi^+ \to \mu^+ + \nu_\mu \tag{7.2}$$

The tunnel is filled with helium gas at 1 atm to reduce the interactions of pions with particles in the tunnel.

Finally, all the secondary particles other than neutrinos are stopped at the beam dump. The dump is consists of 3.5 m thick iron block, 2 m thick concrete, and about 60 m thick soil.

Primary Beam Monitors

The proton beam-line is equipped with two types of primary beam monitors, Current Transformer (CT) and Segmented Plates Ionization Chamber (SPIC).

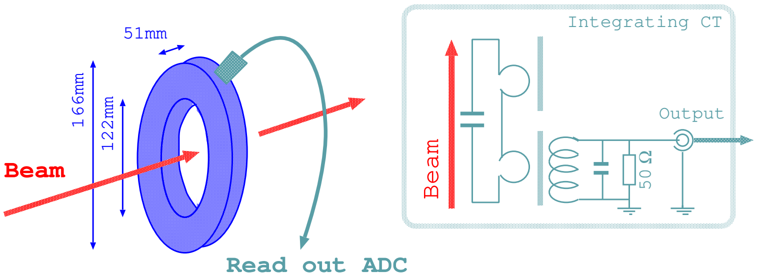

Figure 7.6: Current Transformer (CT).

A schematic view of CT is shown in Figure 7.6. CT is a kind of pick-up coil sensitive to electric current. There are 13 CTs set in the primary beam-line to monitor the proton beam intensity at various points. One of CTs is placed just before the target to monitor the number of protons on the target (p.o.t.) delivered to generate the neutrino beam. Each CT is calibrated using pulse current and beam as well. The proton beam intensity can be measured with small uncertainty less than 10 %.

Figure 7.7 shows a schematic view of SPIC. SPIC is an ionization chamber consist of three copper foiled capton sheets with 1 cm gaps. The central one is a cathode, and the others are horizontal and vertical segmented anodes with 32 × 32 channels readout. The gap is filled with helium gas. There are 28 SPICs set in the beam-line for profile monitoring of beam protons and secondary pions.

Secondary Beam Monitors

The pion monitor (PIMON) measures the momentum and the divergence of pions just behind the second horn. Figure 7.8 shows a schematic view of PIMON. Cherenkov photons generated in fluorine gas (R-C318) are reflected by the pie-shaped spherical mirror set onto the beam-line,

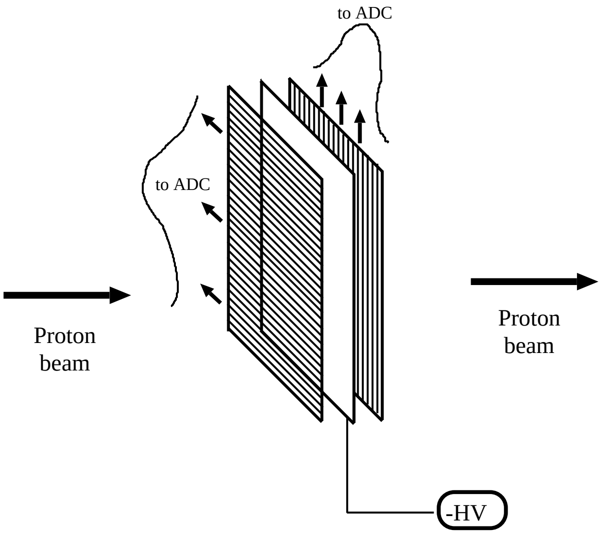

Figure 7.7: Segmented Plates Ionization Chamber (SPIC).

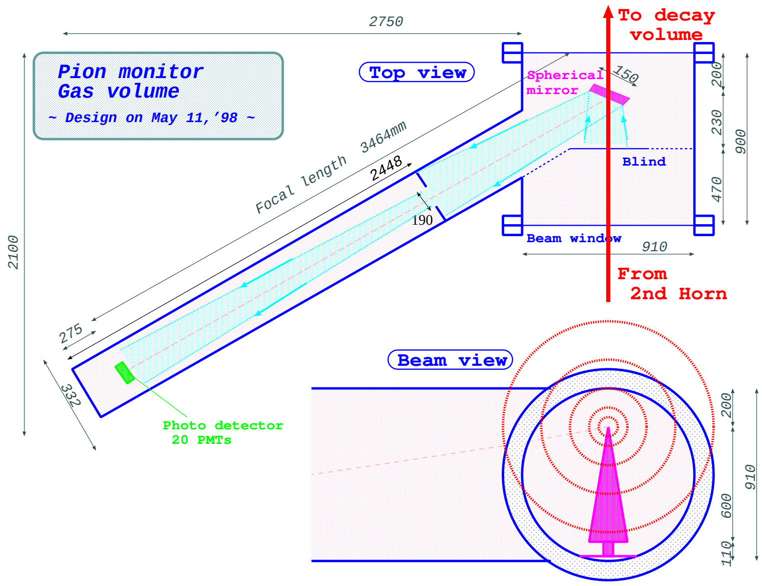

Figure 7.8: A schematic view of the pion monitor (PIMON).

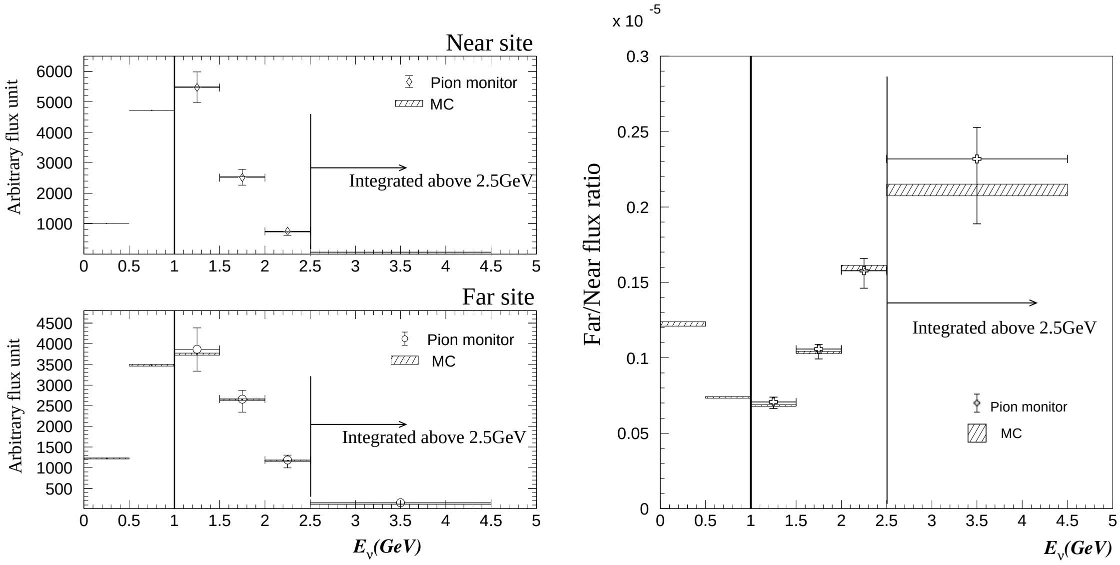

Figure 7.9: The neutrino energy spectrum at the near site (upper-left) and at the SK site (lower-left), and the flux ratio between the SK site and the near site (right). The dots represent the prediction from the PIMON measurement. The boxes show the expectation from the beam Monte Carlo simulation.

and then go to a photo device composed of 20 PMTs. To avoid being a disturbance of the beam, PIMON is set back in the escape zone during normal run.

From the measured pion momentum distribution, we can estimate the energy spectrum of the neutrino beam both at the near site and at the far site, Super-Kamiokande. Figure 7.9 shows the neutrino energy spectra and the far/near neutrino flux ratio predicted from the PIMON measurement. The beam Monte Carlo reproduce the prediction from the PIMON measurement very well. A detailed description of PIMON measurement and analysis can be found in Ref.[92].

The muon monitor (MUMON) is placed about 200 m downstream from the target. Figure 7.10 shows a schematic view of MUMON and its location. MUMON consists of two detectors, the Ionization Chamber (ICH) and the Silicon Pad Detector (SPD) array. ICH is a segmented ionization chamber similar to SPIC. Its cross section is 190 cm $\times$ 175 cm square to measure broad muon profile at the beam dump. ICH contains three planes with 1 cm gaps inside the gas vessel filled with Ar gas. Each readout plane is segmented into 5 cm $\times$ 180 cm strip lines to measure the muon profile. In addition, SPDs are arranged in the muon dump room. The SPD array also measures the muon profile for confirmation of the ICH measurement. There are 17 small SPDs (1 cm$\times$2 cm) and 9 large SPDs (3.4 cm$\times$3.05 cm).

The muon profile monitored by MUMON gives us the directional information of the neutrino beam spill by spill. The position resolution of MUMON is 5cm for the muon profile.

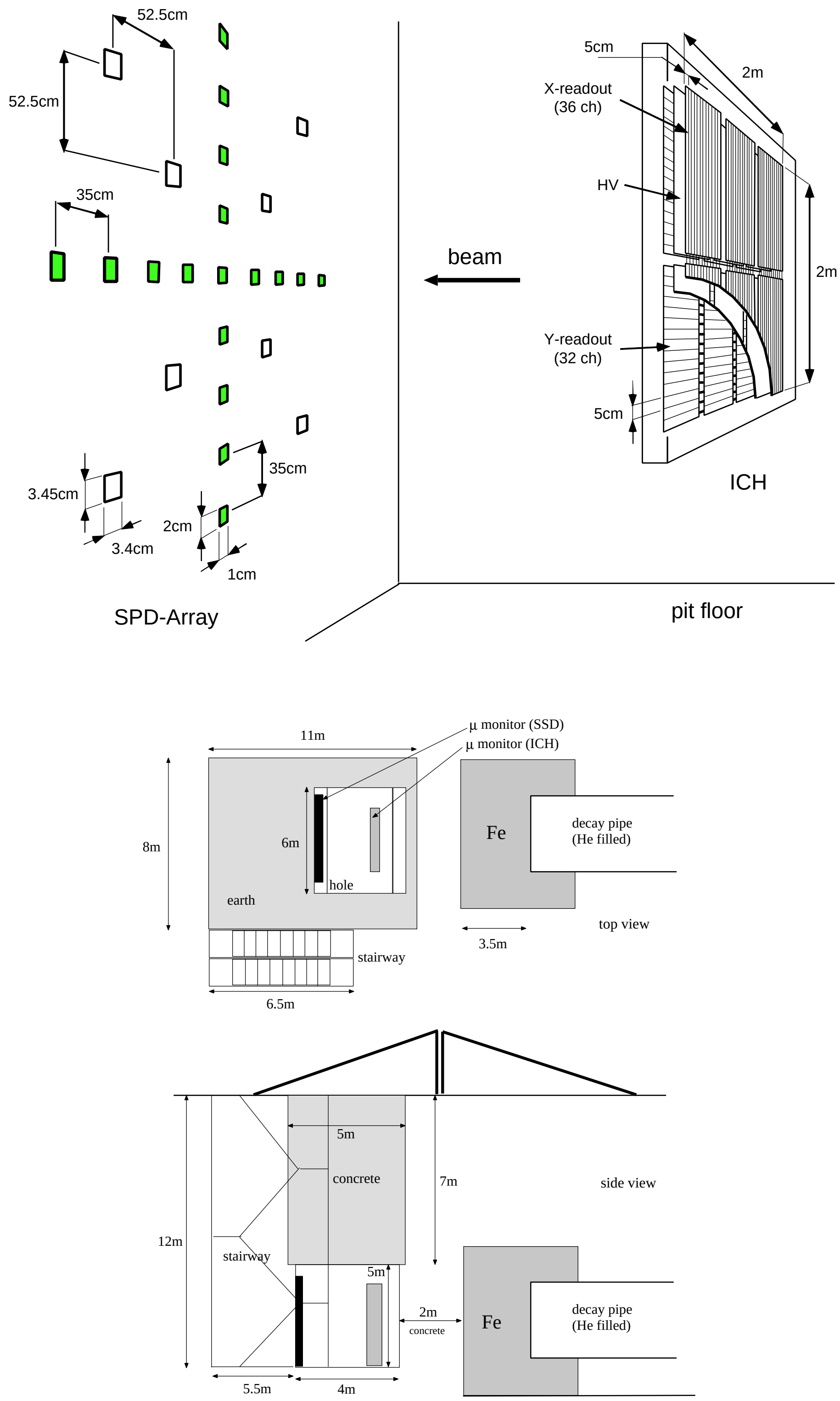

Figure 7.10: A schematic view of the muon monitor (MUMON) and its location.

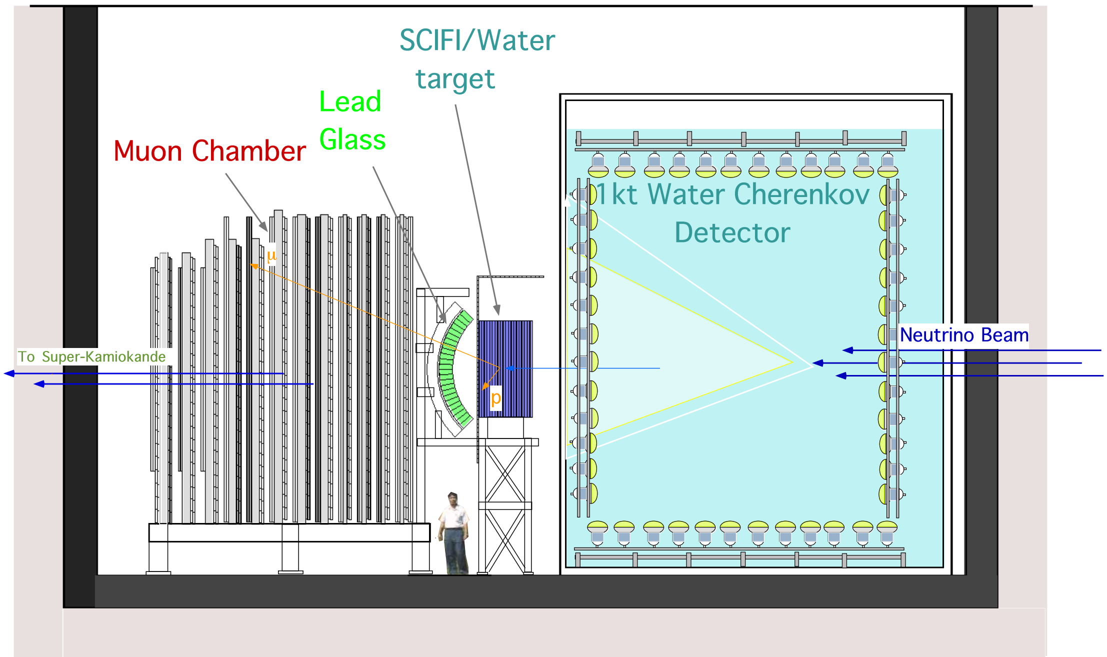

Figure 7.11: A schematic view of the near detectors.

7.1.3 Near Neutrino Detectors

The near neutrino detectors are placed about 300 m downstream of the target in the underground cylindrical hall of 24 m in diameter and 16 m in depth. A schematic view of the near detectors is shown in Figure 7.11. There are 6 detectors in total, the 1kt water Cherenkov detector, the veto counter, the scintillating fiber tracker (Sci-Fi), the trigger counter, the lead glass calorimeter (LG) and the muon range detector (MRD) from upstream to downstream.

The chief aim of the 1kt water Cherenkov detector is measuring the neutrino interaction rate and the energy spectrum at the near site to predict those at Super-Kamiokande. The purpose of the veto counter is to veto the events due to outgoing charged particles generated by neutrino interactions in the 1kt detector. The scintillating fiber tracker is useful for the neutrino interaction study with its fine granularity. The trigger counter is used to give the trigger timing to Sci-Fi, LG and MRD. The lead glass calorimeter measures electromagnetic component in an event. The muon range detector has an ability to measure the neutrino interaction rate, the neutrino beam profile and the neutrino energy spectrum.

The details of the 1kt detector are described later in this chapter. The detailed descriptions of other detectors can be seen in Ref.s [92], [93] and [94].

7.1.4 Far Neutrino Detector

Super-Kamiokande is used as the far detector of the K2K experiment. Even during the K2K beam running period, SK goes on with its normal observation for atmospheric neutrinos, solar neutrinos, nucleon decays and so on. Among a lot of events, the events induced by the K2K neutrino beam are extracted using their timing information. Events in SK are stamped with their triggered time using the GPS (Global Positioning System) clock and the local 50 MHz clock. At KEK, the proton extraction time is recorded for each spill in the same method. Thanks to GPS, clocks at both sites are synchronized within the 200 nsec accuracy. Using this synchronized timing information, the K2K induced events are selected by the offline process.

GPS was also utilized to measure the precise direction of Super-Kamiokande in designing the neutrino beam-line. The error of the beam direction is estimated to be less than 0.1 mrad, which is 10 times better than the physics requirement.

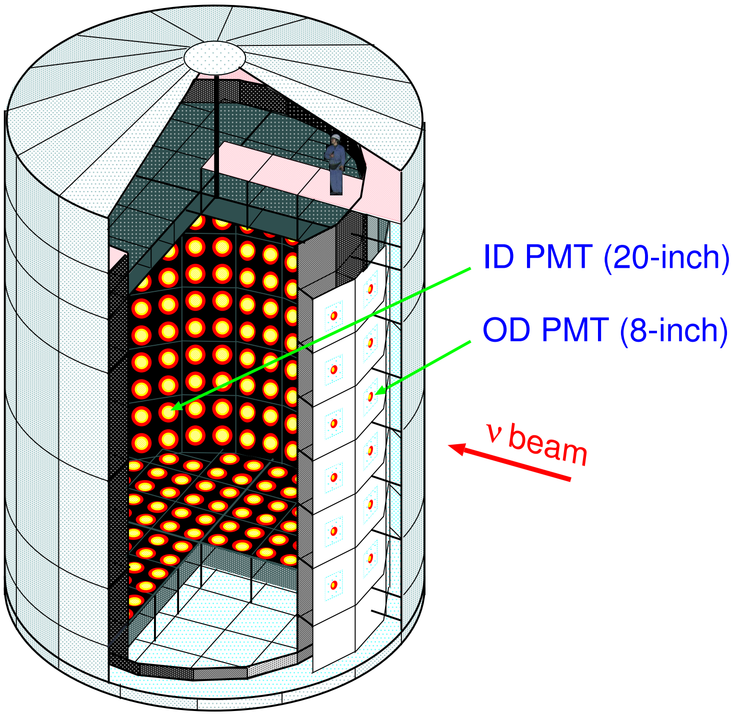

Figure 7.12: A schematic view of the 1kt water Cherenkov detector.

7.2 1kt Water Cherenkov Detector

The 1kt water Cherenkov detector is located about 300 m downstream of the pion production target. As one of the near detectors, its primary purpose is to measure the interaction rate and energy spectrum of neutrinos before oscillations. In addition, it provides an opportunity to study large samples of neutrino interactions in the energy range important for atmospheric neutrino analyses. Since the 1kt detector uses the same detection mechanism, analysis algorithm and interaction Monte Carlo as used in Super-Kamiokande, it is useful for reducing systematic uncertainties on SK analyses.

Many features of the 1kt detector are common to Super-Kamiokande. Only the differences from SK are described in this section.

7.2.1 Detector Tank

Figure 7.12 shows a schematic view of the 1kt water Cherenkov detector. The 1kt detector is quite similar to Super-Kamiokande except for its size. The cylindrical tank, 10.8 m in diameter and 10.8 m in height, holds approximately 1000 tons of pure water. The tank itself was originally used for the KEK-PS E261A experiment which was carried out to check the performance of the e/μ identification program employed in Kamiokande [95].

The inner detector (ID) and the outer detector (OD) are optically separated by black sheets and Tyvec sheets. Figure 7.13 shows a photograph of the ID before filling water. The cylindrical

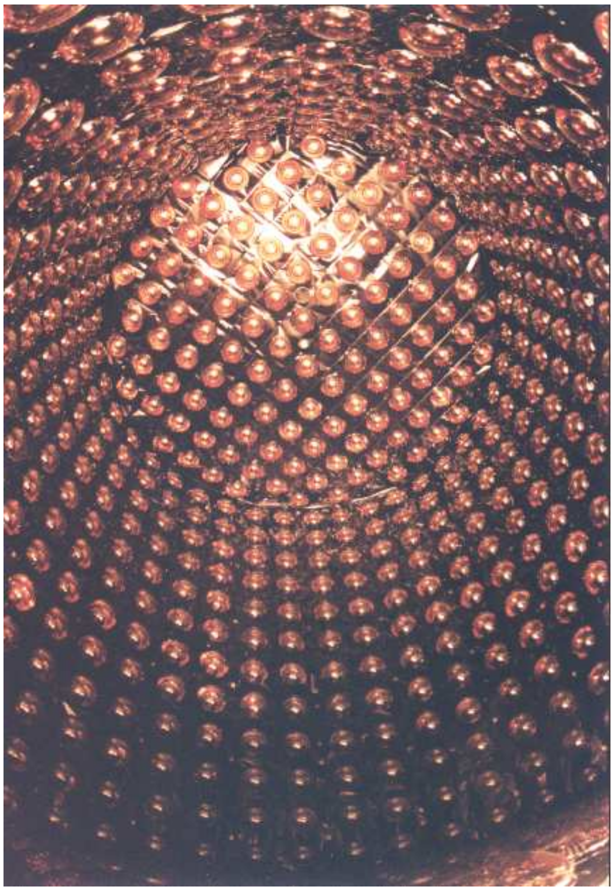

Figure 7.13: A photograph of the inner detector viewed from the bottom before filling water. The photocathode coverage is about 40 % and the rest of the surface is covered by black sheets.

Figure 7.14: The upstream OD of the 1kt tank looked down from the top before filling water. The OD PMTs, the wavelength shifter plates and white Tyvec sheets are seen.

inner region is 8.6 m in diameter and 8.6 m in height and viewed by 680 inward facing 50 cm PMTs, 456 on the barrel wall and 112 each on the top and the bottom. The PMTs and their arrangement are identical to those of Super-Kamiokande, resulting in the same photocathode coverage, $\sim 40\,\%$. One of the differences between SK and the 1kt is the OD. In the SK tank, the ID is completely surrounded by the OD. However, the 1kt OD only covers the upstream 1/3 of the barrel part and the whole of the bottom part, in order to enlarge the ID volume as much as possible. As such, the whole inner volume is offset by about 0.5 m in the downstream direction, allowing more space between the upstream wall and the surface of the OD PMTs (see Figure 7.11). Figure 7.14 shows a photograph of the upstream OD before filling water. The thickness of the OD volume is 1 m for the upstream barrel and 0.6 m for the bottom. The barrel has 42 20 cm PMTs while the bottom has 26 PMTs. Each OD PMT is equipped with the same wavelength shifter plate 60 cm square as used in Super-Kamiokande.

To compensate the geomagnetic field which affects the PMT response, 9 horizontal Helmholtz coils and 7 vertical Helmholtz coils are arranged surrounding the water tank. The residual magnetic field is kept below 100 mG in every position of the detector.

7.2.2 Water Purification System

As shown in Figure 7.15, the water purification system for the 1kt detector is slightly more simple than that for SK because the Radon reduction is not necessary in the 1kt. About 20 ton/hour of water is being processed.

The temperature of the detector water is kept at 11 °C. By virtue of insulators surrounding the tank, the fluctuation of the water temperature is less than $\pm\,1.5$ °C over a whole year. Water purity is always monitored by the measurement of the electrical resistance ($\sim 10\,\mathrm{M\Omega/cm}$).

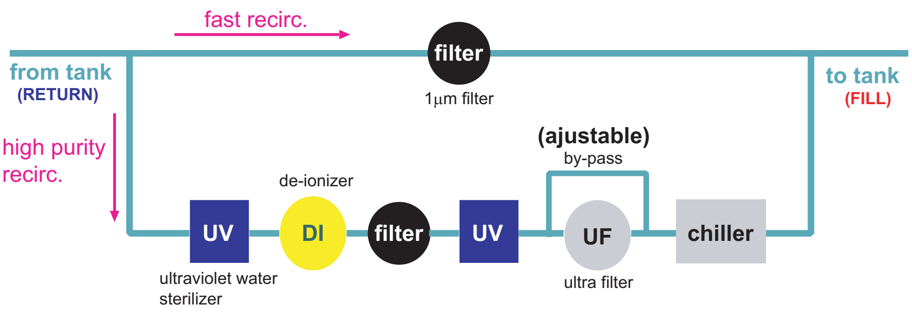

Figure 7.15: The water purification system for the 1kt detector.

7.2.3 Data Acquisition System

The data acquisition system of the 1kt is also quite similar to those of SK. 66 ATMs are used as the frontend electronics for the ID PMTs and the OD PMTs, and the trigger signal is generated from ATM hit information. The trigger threshold is about 40 hits of the ID PMTs. In the 1kt, the event trigger is only permitted during four time-gates per beam cycle (2.2 sec). One is the main gate opened for beam neutrino events (on-spill gate), another is for events succeeding neutrino events, such as an electron from decay of a neutrino-induced muon (delayed gate), another is for measurement of the background event rate (off-spill gate) and the other is for collecting cosmic ray muon events which are used for some calibrations (cosmic-μ gate).

One major difference between the SK data acquisition system and the 1kt data acquisition system is ID-PMTSUM. The trigger signal generation using ATM hit information has a deadtime of 500 nsec. In the 1kt, due to intense neutrino flux, it sometimes occurs that more than one event happens within 500 nsec in a spill. We cannot correctly count the number of events in such a spill. It means that we cannot accurately measure the neutrino flux. In order to solve this problem, we record ID-PMTSUM every spill. Each ATM board generates a PMTSUM signal, a attenuated analog-sum of 12 PMTs signal connected to the ATM, with no deadtime. These PMTSUM signals are analog-summed over all the ATMs to produce the ID-PMTSUM signal. Therefore ID-PMTSUM is a attenuated analog-sum of all 680 ID PMTs' signals. ID-PMTSUM is recorded using a 500 MHz 8-bit FADC. To count peaks in the ID-PMTSUM signal, we can find the number of events in a spill. Figure 7.16 shows a typical ID-PMTSUM of one spill recorded by FADC. Two high peaks and one low peak are seen. We set a threshold for peak searching to the level corresponding to 1000 p.e.s ($\sim$ 100 MeV electron), in order to eliminate the signals from μ-decay electrons such as the third peak in the figure.

7.2.4 Calibration

The relative gain and the relative timing of PMTs in the 1kt are calibrated using the same methods as used in SK [96]. The energy scale is calibrated using cosmic ray through-going muons, cosmic ray stopping muons, and single π^0 events produced by beam neutrino interactions. As for the cosmic ray through-going muon, the ratio of the total number of p.e.s to the muon track length ($\sim$ 22 p.e.s/cm) is compared between data and MC. This ratio is also used for checking the time variation of the energy scale. The other methods using cosmic ray stopping muons and

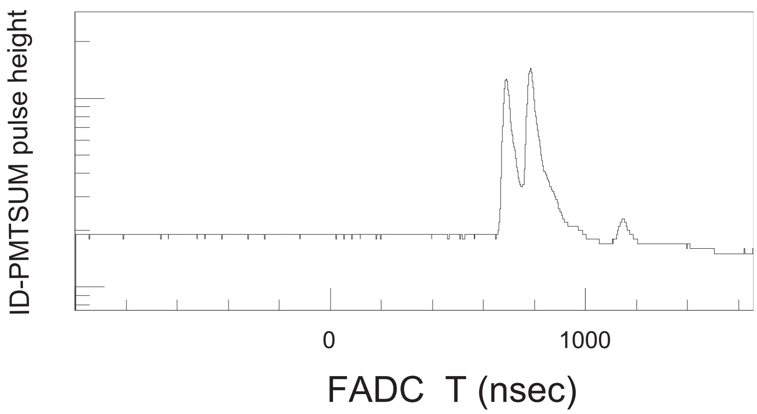

Figure 7.16: A typical ID-PMTSUM recorded by FADC.

neutrino-induced π^0 events are explained in Section 2.3.6. The discrepancy between the energy scales from the three analyses is below 5 % and adopted as the systematic uncertainty of the energy scale.

7.2.5 Data Reduction

Since SK and the 1kt detect different source of events, the data reduction procedure is completely different. The reduction steps of the 1kt data are as follows :

- **good beam selection**
  The spills during the machine study, the beam tuning, the PIMON measurement or the beam line component trouble are rejected. The spills with proton intensity below 1.0×10^{12} ppp (protons per pulse) or with horn current below 240 kA are also rejected.

- **on-spill data selection**
  Only events in on-spill gates are selected.

- **with no pre-activity**
  The spills with detector activities during 1.2 μsec before the spill are rejected to prevent cosmic rays from occupying electronics. The fraction the spills with pre-activities is about 1.3 %.

- **single event selection**
  The spills which contain more than one event are rejected. The number of events in a spill is counted from ID-PMTSUM signal recorded on the FADC. This cut effectively reject events with low charge below about 1000 p.e. as described in Section 7.2.3. Figure 7.17 shows the timing distribution of detected ID-PMTSUM peaks and the distribution of the number of peaks in a spill. It is found that the number of spills with multiple events is about a tenth of the number of spills containing a single event.

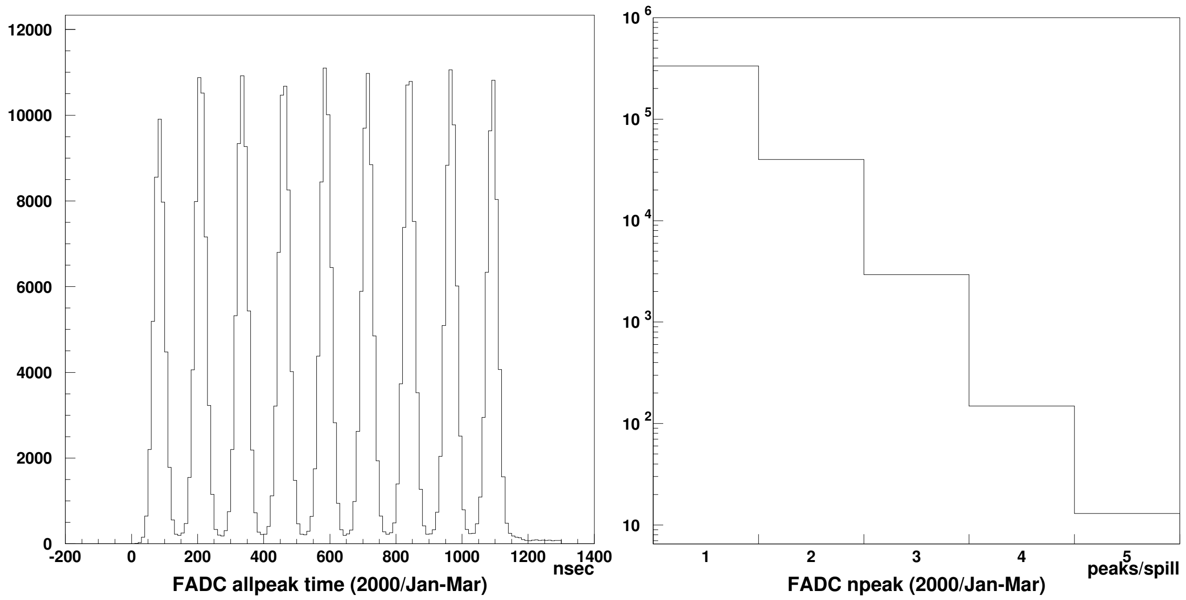

Figure 7.17: The timing distribution of detected ID-PMTSUM peaks (left) and the distribution of the number of peaks in a spill (right).

Chapter 8

π^0/μ Measurement in 1kt Detector

8.1 Fully Contained Sample

The π^0 events and the μ events are extracted from the fully contained sample. In Super-Kamiokande, since the inner tank is completely surrounded by the outer detector, FC events can be easily selected using the OD hit information. However, in the 1kt detector, the OD is only instrumented on the bottom and on the side wall in the upstream direction as already described in Section 7.2.1. We adopt another method to identify FC events using the charge information of the ID PMTs. When a charged particle exits the inner tank, the ID PMTs near the exit point are intensively lit up by Cherenkov light. The ATM channels connected to those PMTs tends to saturate. In practice, we look in a cone with a 20° opening angle along the direction of the most energetic ring to find the PMT with the most charge. The charge (the number of p.e.s) on that PMT is referred to as "pomax20deg". Figure 8.1 shows the pomax20deg distribution for events in the 50t fiducial volume. The definition of the fiducial volume is described later. The peak due to the ATM channel saturation is seen in the region of $220 \sim 300$ p.e.. We classify the event with pomax20deg below 200 p.e. as a FC events.

The final sample of FC events is made by the following criteria :

(1) Visible energy (E_{vis}) $>$ 30 MeV

(2) Pomax20deg $<$ 200 p.e.

(3) The reconstructed vertex is in the fiducial volume

Criterion (1) is required to eliminate low energy background. Criterion (2), as described above, makes sure that FC events have no clear exit point of charged particles. As for criterion (3), we define two types of the fiducial volumes shown in Figure 8.2. For multi-ring events, we use the 50t cylindrical region with a diameter of 4 m and a length of 4 m along the beam axis. On the other hand, the fiducial volume for single-ring events is defined as the upstream half of the 50t fiducial volume ($\sim$25t). We abandon the downstream half, since we know the performance of our fitting algorithm is relatively worse in case of the single-ring event whose vertex position is close to the wall in its way.

The results described in this chapter is based on the data taken from January to March, 2000 and from January to July, 2001 corresponding to 3.21×10^{19} protons on target. A total of 71661 (43214) FC events is obtained after these cuts in the 50t (25t) fiducial volume.

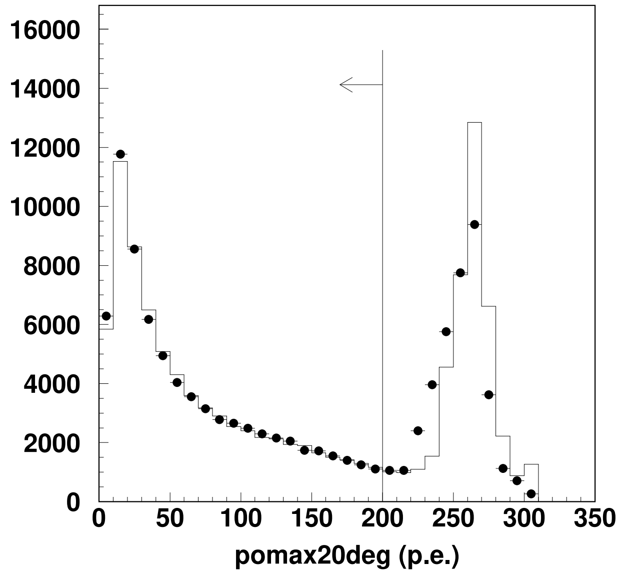

Figure 8.1: The pomax20deg distribution for the data (dots) and the neutrino MC (histogram) in the 50t fiducial volume. The arrow shows the FC selection criterion. The reason for the discrepancy between the data and the MC around the peak of the electronics saturation is that the measured saturation point of each ATM channel is not accurately introduced in our simulation.

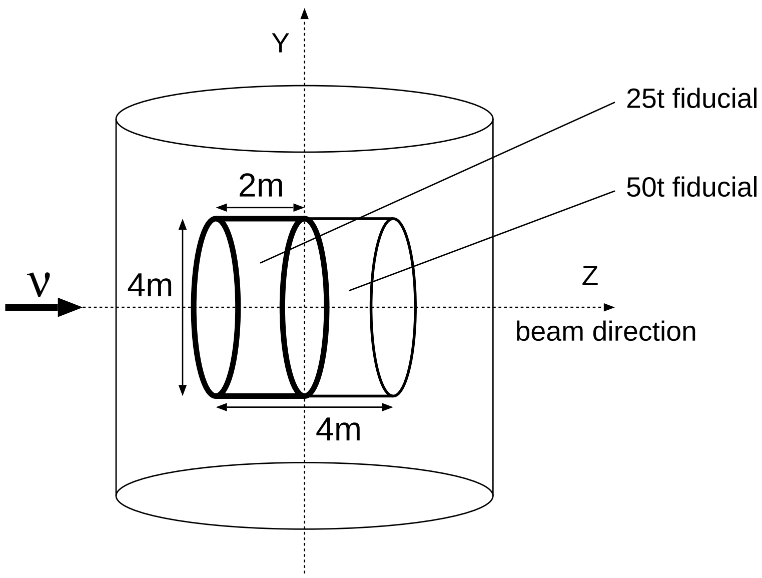

Figure 8.2: The definition of the fiducial volume in the 1kt detector, for single-ring events (25t) and for multi-ring events (50t).

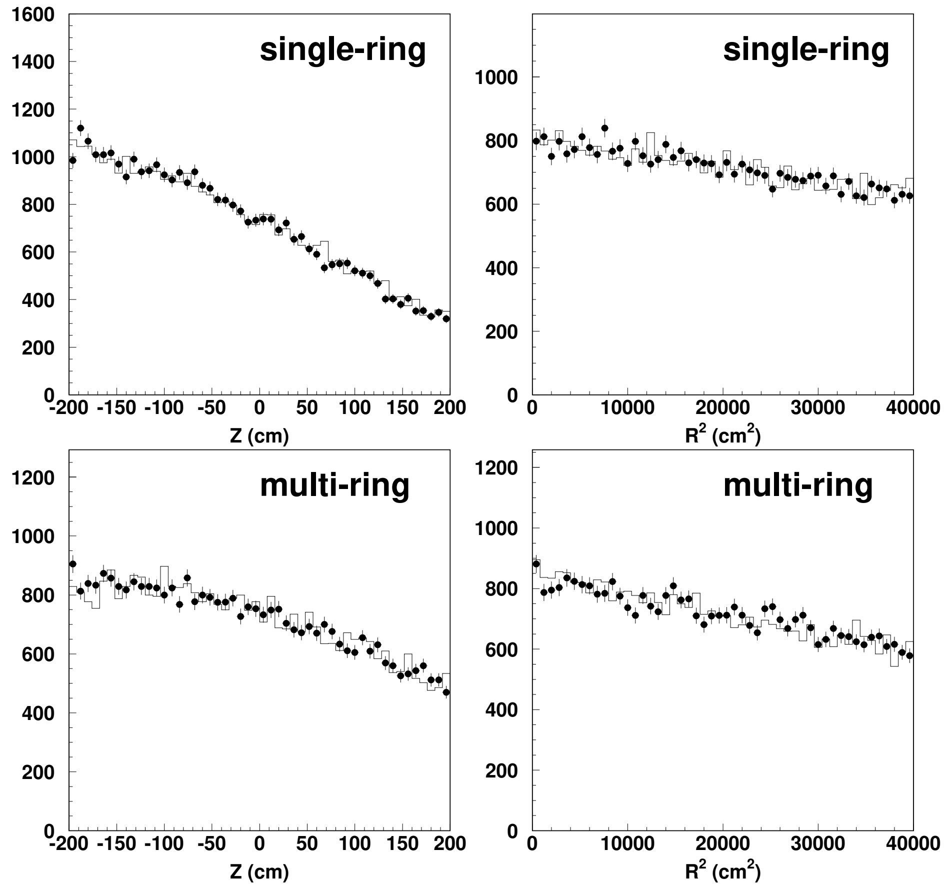

Figure 8.3: Vertex distributions for FC events in the 50t fiducial volume. Z is the beam direction. R $(= \sqrt{X^2 + Y^2})$ is the distance from the beam axis to the reconstructed vertex.

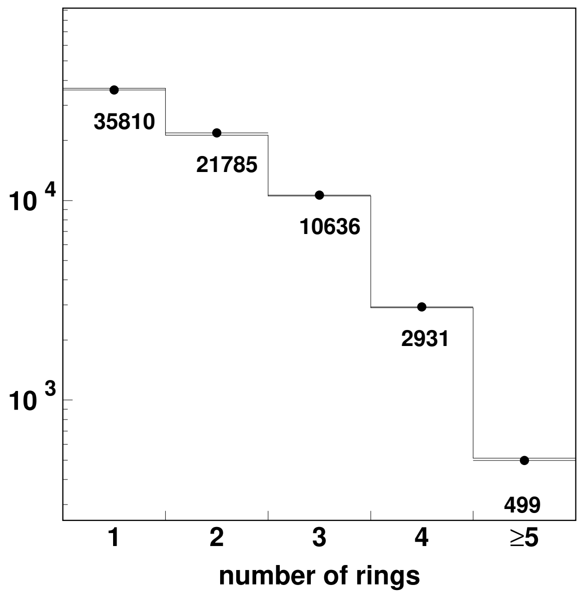

Figure 8.4: The number of rings distribution for observed FC events (dots and numbers) and the Monte Carlo prediction (histogram) normalized by entry.

Figure 8.3 shows vertex distributions for FC events in the 50t fiducial volume. The left two figures show Z distributions. As it goes forward (larger Z), less FC events are observed because produced charged particles have dominantly the similar direction to the neutrino beam way and their acceptance becomes smaller in the downstream region. The right two figures show R^2 distributions, where R $(= \sqrt{X^2+Y^2})$ is the distance from the beam axis to the reconstructed vertex. The dots represent the data with statistical errors, and the histograms show the neutrino Monte Carlo expectation normalized to the data by entry. The number of Cherenkov rings distribution for the FC sample is shown in Figure 8.4. The data distributions are well reproduced by the neutrino MC.

8.2 π^0 Events Selection

The selection criteria for π^0 events in the 1kt detector are almost the same as the criteria used in Super-Kamiokande and are as follows :

(A) FC events in the 50t fiducial volume

(B) the number of rings is 2

(C) both rings have a showering type (= e-like) particle identification

(D) 85 MeV/c^2 < the invariant mass of 2 e-like rings ($\mathrm{M}_{\gamma\gamma}$) < 215 MeV/$c^2$

Figure 8.5 shows the distribution of the invariant mass of 2 e-like rings ($\mathrm{M}_{\gamma\gamma}$) for events after the cuts (A)-(C). A π^0 mass peak is clearly visible both in data and in MC. The 2 % difference

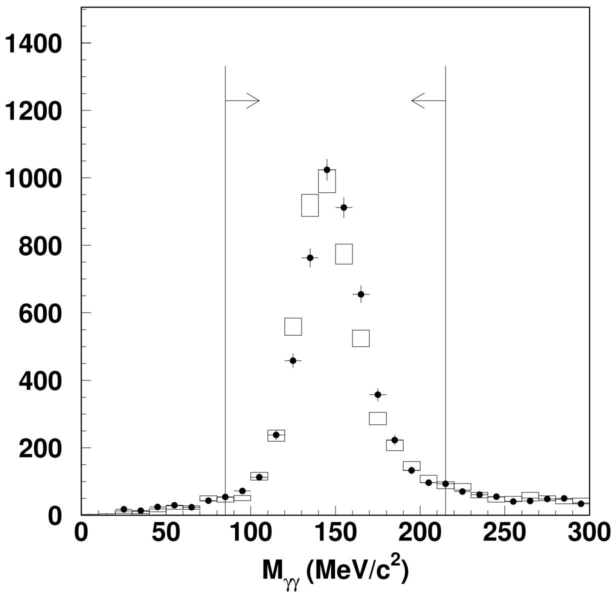

Figure 8.5: The invariant mass distribution of 2 e-like rings ($M_{\gamma\gamma}$) for events which satisfy the cuts (A)-(C) (see text). The neutrino Monte Carlo expectation (boxes) is normalized to the data (dots) by entry.

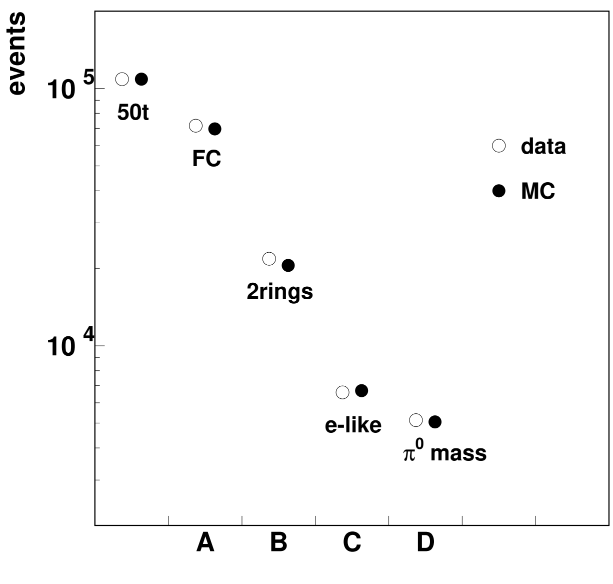

Figure 8.6: The number of events after each selection criterion (see text) for π^0 sample. The open circles represent the data. The numbers for the neutrino MC (filled circles) are normalized using the number of total neutrino events in the fiducial volume (first bin).

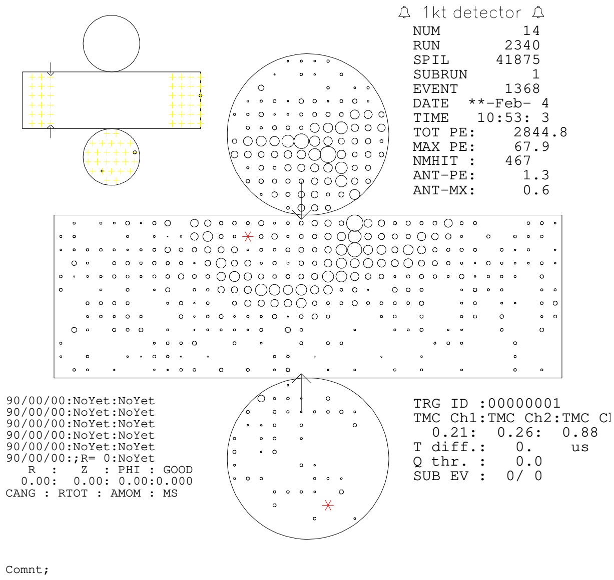

Figure 8.7: A typical event in the 1kt π^0 sample.

between the data peak position of 147.9 ± 0.3 MeV/c^2 and the MC peak position of 144.8 ± 0.4 MeV/c^2 is well within our quoted systematic uncertainty of the absolute energy scale of 5 %. Figure 8.6 shows the number of events after applying each selection criterion for data and neutrino MC. A typical π^0 event in the 1kt detector is shown in Figure 8.7.

Figure 8.8 shows the MC estimated efficiency to reconstruct a single π^0 in the neutral current interaction events which have a single π^0 and no charged particles in the final state. The total efficiency is estimated to be about 47 %. The efficiency drops off as a function of π^0 momentum for the same reason described in Section 6.2.

Figure 8.9 shows vertex distributions for π^0 events in the 50t fiducial volume. There is good agreement between the data and the neutrino MC.

Table 8.1 -(i) shows the production modes of the MC π^0 sample. The π^0 sample has an NC fraction of 83 %. The fraction of each NC interaction channel is similar to that in the Super-Kamiokande π^0 sample (Table 6.2-(i)) except for the NC coherent π fraction of 12.4 % in the 1kt against 21.2 % in SK. This is because the K2K beam has small flux in the neutrino energy region below 500 MeV where the NC coherent π production is dominant channel to make a single π^0. The difference of neutrino energy spectrum producing the π^0 sample at SK and the 1kt detector is discussed later in Section 9.1.

Figure 8.10 shows the π^0 momentum distribution for the data, compared to the neutrino MC expectation shown by each production channel. While it can be said that the data distribution is reproduced fairly well by the MC, there exist small discrepancy in the shape around 200$\sim$400 MeV. It it clear that this shape difference can not completely be compensated with simply changing the mixture of each production channel. One of the possible cause is the uncertainty in the width of a Δ resonance in a ^{16}O nucleus. Kim *et al.*[97], Singh *et al.*[98] and Marteau *et al.*[99] have recently pointed out that the nuclear medium can modify widths of resonances. Further studies are needed to solve this problem.

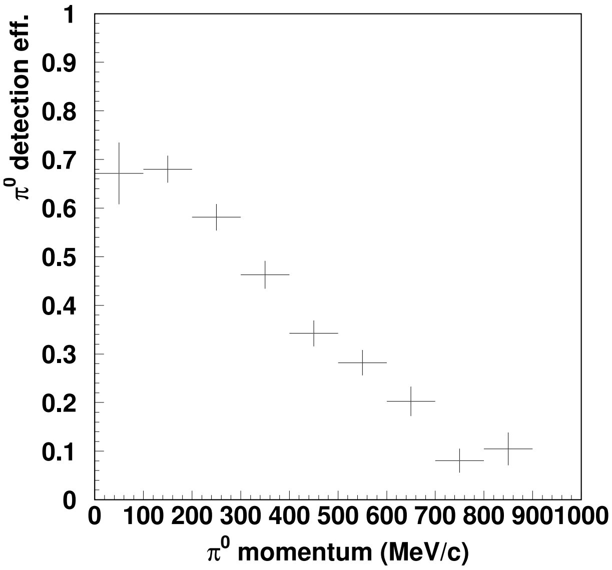

Figure 8.8: The π^0 detection efficiency as a function of its momentum. The total efficiency is about 47 %.

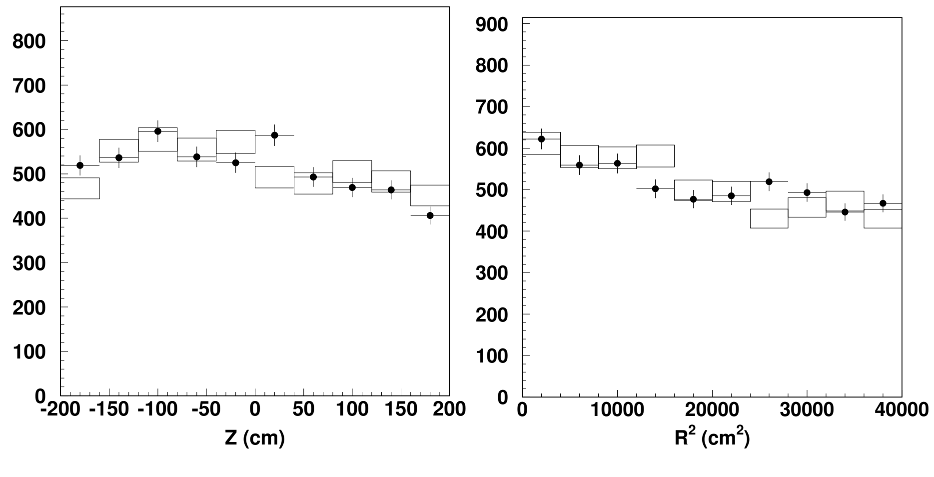

Figure 8.9: Vertex distributions for π^0 events in the 50t fiducial volume.

		(i) π^0 events	(ii) μ events
ν_e CC		0.5 %	0.1 %
	q.e.	0.1 %	0.1 %
	single π	0.3 %	0.0 %
	coherent π	0.0 %	0.0 %
	multi π	0.1 %	0.0 %
ν_μ CC		16.7 %	96.3 %
	q.e.	0.1 %	51.4 %
	single π	8.1 %	34.9 %
	coherent π	0.1 %	1.8 %
	multi π	7.5 %	8.0 %
NC		82.8 %	3.7 %
	single π	46.7 %	2.1 %
	coherent π	12.4 %	0.1 %
	multi π	18.9 %	1.2 %

Table 8.1: The fraction of the each interaction channel for (i) the π^0 sample and (ii) the μ sample in the 1kt detector.

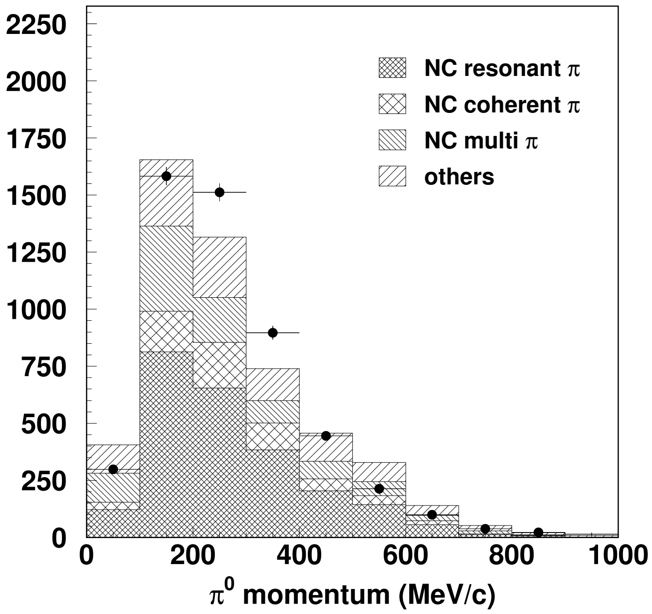

Figure 8.10: The π^0 momentum distribution for the data (dots) and the neutrino MC expectation (histograms) shown by each production channel.

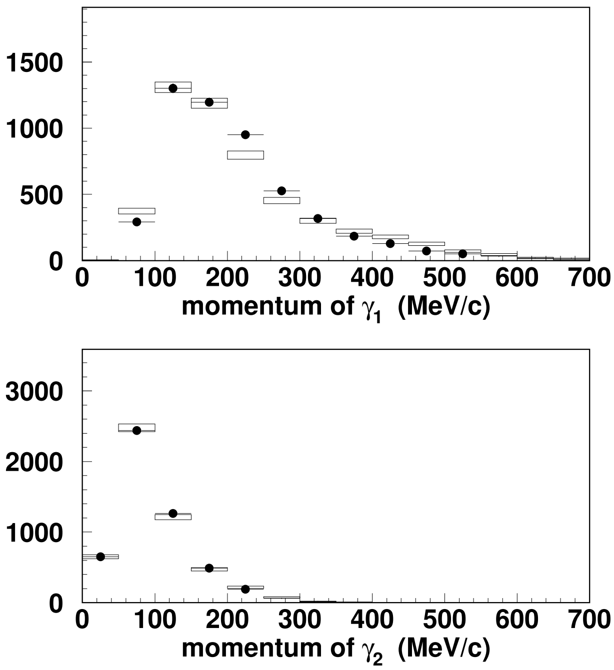

Figure 8.11: The distribution of each showering ring composing π^0 events. γ_1 (γ_2) represents the ring with higher (lower) energy.

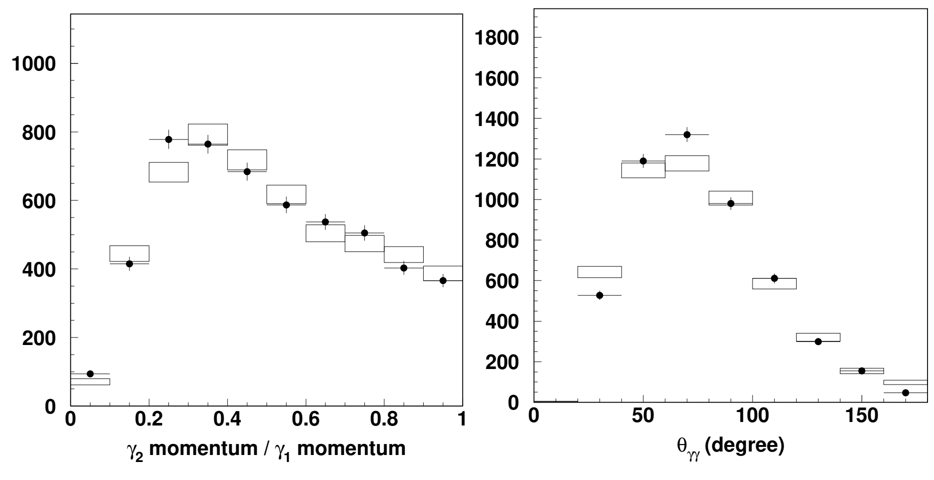

Figure 8.12: The momentum ratio and the opening angle between two gamma-rays composing π^0 events.

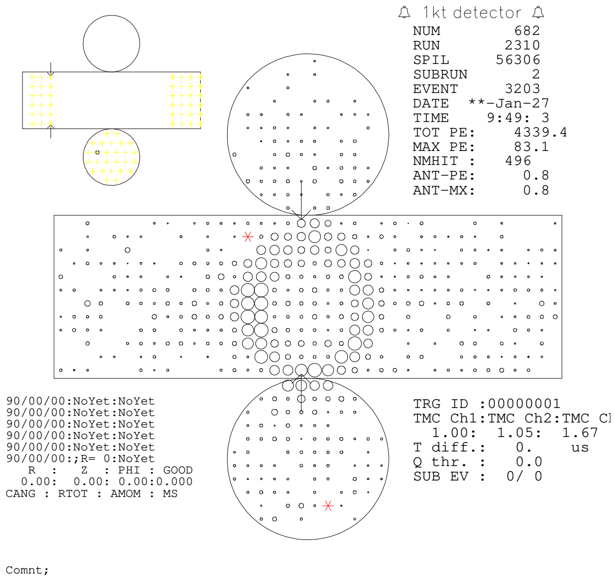

Figure 8.13: A typical event in the 1kt μ sample.

Figure 8.11 shows the momentum distribution of each showering ring composing π^0 events. γ_1 (γ_2) means the ring with higher (lower) energy. The distributions of the momentum ratio and the opening angle between two gamma-rays are shown in Figure 8.12. The data and the MC agree reasonably well. Slight differences on these figures come from the shape difference in the π^0 momentum distribution described above.

8.3 μ Events Selection

The selection criteria for μ events in the 1kt detector are quite similar to those used in the Super-Kamiokande analysis :

(a) FC events in the 25t fiducial volume

(b) the number of rings is 1

(c) the ring has a non-showering type (= μ-like) particle identification

Figure 8.13 shows a typical μ event observed in the 1kt detector. Figure 8.14 shows the number of events after applying each selection criterion for data and neutrino MC.

The fraction of the 1kt μ sample due to each interaction channel is estimated by the neutrino MC and is listed on Table 8.1-(ii). The μ sample has a charged current fraction of 96 %, where 51 % is due to CC q.e. scatterings and the rest 45 % is from CC pion production channels where a pion(s) is(are) below Cherenkov threshold or absorbed in the nucleus. The NC interaction induced events are from NC pion productions accompanying a charged pion above Cherenkov threshold. Figure 8.15 shows the μ momentum distribution. There is a good agreement between the data and the MC.

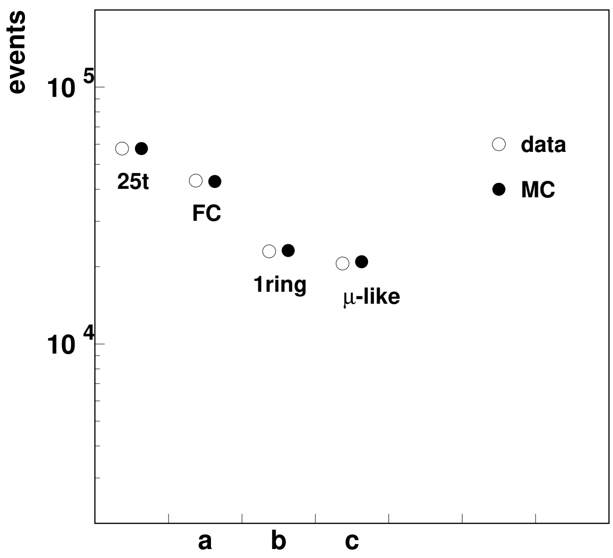

Figure 8.14: The number of events after each selection criterion (see text) for μ sample. The open circles represent the data. The numbers for the neutrino MC (filled circles) are normalized by the number of total neutrino events in the fiducial volume (first bin).

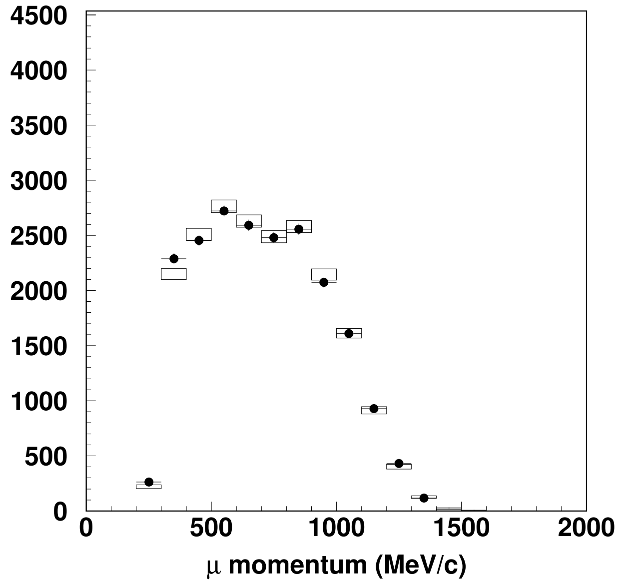

Figure 8.15: The reconstructed μ momentum distribution. The dots represent the data with statistical errors. The boxes show the neutrino Monte Carlo expectation normalize to the data by entry. The size of boxes shows statistical errors.

8.4 Results

According to the above selection criteria, a total of 5133 π^0 events is observed in the 1kt detector during the K2K running period from January to March, 2000 and from January to July, 2001. This means that the 1kt detector has collected more than ten times as many π^0 events as Super-Kamiokande has obtained until now. A total of 20555 FC single-ring μ events is also observed in the 1kt during the same period. From the observed data and the neutrino Monte Carlo, we obtain :

$$R_{\pi^0} \;=\; \frac{(\pi^0/\mu)_{\mathrm{Data}}}{(\pi^0/\mu)_{\mathrm{MC}}} \;=\; 1.00 \pm 0.02\ (data\ stat.) \pm 0.09\ (sys.) \tag{8.1}$$

The systematic uncertainty on the R_{π^0} measurement in the 1kt is estimated to be about 9%. The details of the systematic uncertainty are discussed in the next section.

8.5 Systematic Uncertainty

neutrino beam flux	
energy spectrum	2 %
ν_e contamination	1 %
event reconstruction	
fiducial volume	3 %
ring counting	6 %
particle identification	5 %
energy scale	
FC selection	1.5 %
invariant mass cut	1.5 %
MC statistics	1 %
total	9 %

Table 8.2: The systematic uncertainties on R_{π^0} measurement in the 1kt.

The systematic uncertainties we identify on our measurement of R_{π^0} in the 1kt detector are listed in Table 8.2. Among the measurement uncertainties due to various sources, the uncertainties related to the neutrino beam flux, the fiducial volume determination and the FC event selection are directly evaluated from changes on the double ratio. The others are evaluated for the π^0 sample and the μ sample separately and then combined on the double ratio assuming no correlations.

Neutrino Beam Flux

The uncertainty on the neutrino energy spectrum at the K2K near detectors is estimated for each energy bin above 1 GeV based on the PIMON measurement uncertainty, while the errors on the flux below 1 GeV is derived from the uncertainties of the beam simulation and front detector measurements. The effect on R_{π^0} is evaluated by independently varying the flux values in each neutrino energy bin. The result is 2 %.

In the 1kt Monte Carlo, ν_e events are blended with ν_μ events using the measured ν_e/ν_μ interaction ratio in Sci-Fi, which is one of the near detectors and uses the same interaction target (*i.e.* water) as the 1kt. The ratio is measured to be $\nu_e/\nu_\mu = 1.8 \pm 0.6(stat.)\,^{+0.8}_{-1.0}(sys.)$ (%) [93]. By varying the ν_e contamination rate in the MC within the assigned error, the uncertainty on R_{π^0} is estimated to be 1 %.

Fiducial Volume Determination

The boundaries of the fiducial volume are shifted by $\pm$ 31 cm, which is the vertex resolution of π^0 events by our fitting algorithm, along the beam direction and perpendicular to the beam direction. The maximum change on R_{π^0} is 3 % and adopted as the systematic uncertainty.

FC Events Selection

Since FC events are identified using the charge information of the ID PMTs as described in Section 8.1, the energy scale uncertainty of $\pm$ 5 % affects this selection. The systematic uncertainty is calculated varying the cut value of pomax20deg (see Figure 8.1) by $\pm$ 5 %, resulting in 1.5 % error on R_{π^0}.

Invariant Mass Cut

The invariant mass cut as one of the selection criteria for π^0 events is also influenced by the absolute energy scale uncertainty. Scaling the reconstructed invariant mass for MC events by $\pm$ 5 % changes the number of π^0 events by 1.5 %.

Particle Identification for μ Event Selection

Figure 8.16 shows the PID parameter distribution of FC single-ring events for the data and the neutrino MC. The rings with positive parameters are classified as μ-like (see Section 5.3). In this parameter distribution, while the height of the μ-like peak depends primarily on physical amounts (cross section, flux, etc.), the shape and the position of the peak are sensitive to parameters related to the detector. For example, if the light scattering in water becomes larger, Cherenkov rings have fuzzier edges and their PID parameters are shifted to the e-like direction. Thus, the systematic difference between the actual detector and our detector simulator affects the particle identification algorithm. As one of the ways to evaluate the systematic difference between the data and the Monte Carlo, the μ-like peak in each distribution is fitted with a Gaussian distribution. With the knowledge of fitting parameters, the MC distribution is shifted and then scaled in such a way that the peak of the modified MC distribution has the same position and spread as the data peak. Using this new MC distribution, we can count the number of μ-like events again. Finally, by comparing newly obtained number with the original number, the systematic uncertainty on the number of μ events can be estimated. The result is below 1 %. Therefore, as a more conservative way, we simply calculate the $(R_{\rm MC} - R_{\rm data})/R_{\rm data}$, where R represents the ratio of the number of FC single-ring μ-like events to the number of FC single-ring events. The result is 1.7 % and adopted as the systematic uncertainty.

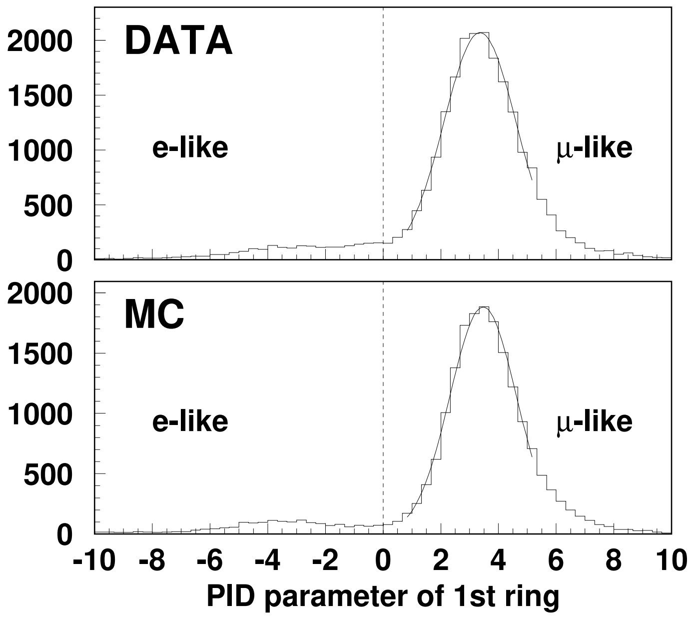

Figure 8.16: The PID parameter distribution of FC single-ring events in the 25t fiducial volume for the data and the neutrino MC. The continuous line shows the fit with a Gaussian distribution.

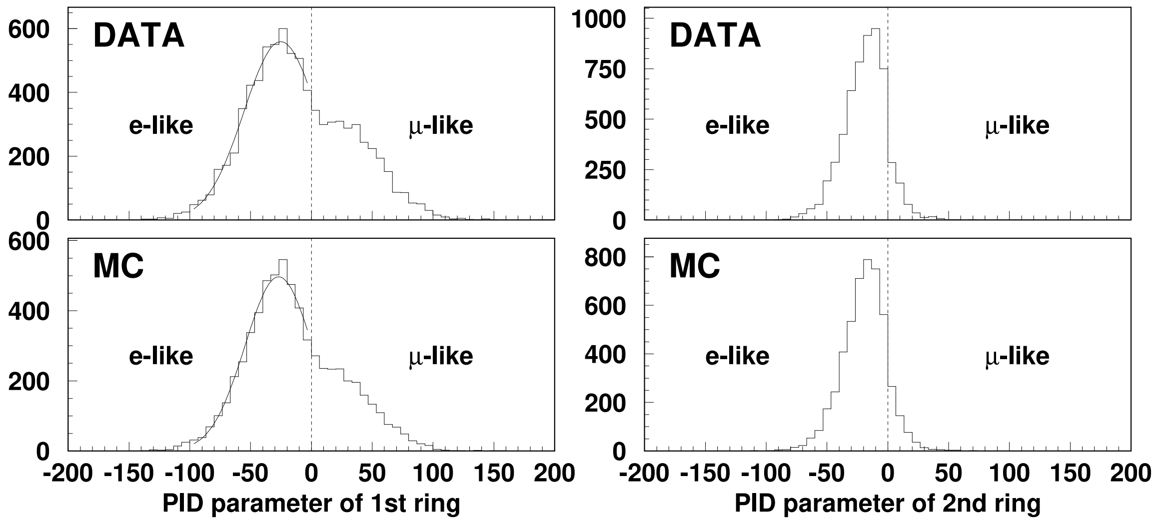

Figure 8.17: The PID parameter distributions of FC two-ring events in the 50t fiducial volume for the data and the neutrino MC. The left (right) figures show the PID parameter distribution of the first (second) ring in each event which has the e-like second (first) ring.

Particle Identification for π^0 Event Selection

Figure 8.17 shows the PID parameter distributions of FC two-ring events for the data and the neutrino MC. The rings with negative parameters are classified as e-like. To estimate the systematic uncertainty due to the PID for π^0 selection, we use the same method as the single-ring μ case. For the distribution of the first ring (left figures), the e-like peak is fitted with a Gaussian distribution. With the knowledge of fitting parameters, the MC distribution is shifted and then scaled in such a way that the peak of the modified MC distribution has the same position and spread as the data peak. In the case of the second ring distribution (right figures), the Gaussian peak fitting is a bit difficult. Therefore MC distribution is simply shifted by the difference between the means of data and MC distributions. The MC distributions of the first ring and the second ring are modified simultaneously. The change on the number of events with two e-like rings is about 5 % and adopted as the systematic uncertainty.

Ring Counting for μ Event Selection

Figure 8.18 shows the likelihood distribution of the most probable second ring candidate in each FC event which has the μ-like first ring. If the most probable candidate has a positive likelihood value, the candidate is adopted as the second ring and the ring candidate search starts for the third ring. If the most probable candidate has a negative likelihood value, the number of rings of this event is determined to one. In this likelihood distribution, while the height of the peak depends primarily on physical amounts (cross section, flux, etc.), the shape and the position of the peak are sensitive to parameters related to the detector. For example, as the light reflection on detector material becomes larger, it is more possible that reflected lights are recognized as Cherenkov rings by mistake, and likelihood values are shifted toward the positive direction. The systematic uncertainty due to the ring counting for μ selection is estimated using the same method as the PID case. The peak in the negative likelihood region is fitted with a Gaussian distribution. With the help of fitting parameters, the MC distribution is shifted and then scaled in such a way that the peak of the modified MC distribution has the same position and spread as the data peak. The change on the number of FC single-ring μ-like events is less than 1 % by this manipulation. Therefore, as a more conservative way, we calculate the $(r_{\rm MC} - r_{\rm data})/r_{\rm data}$, where r represents the ratio of the number of FC single-ring μ-like events to the number of FC events with the μ-like first ring. The result is 4 % and adopted as the systematic uncertainty.

Ring Counting for π^0 Event Selection

Figure 8.19 shows the ring counting distributions for selecting two-ring events. The left figures show the likelihood distribution of the most probable second ring candidate in each FC event which has the e-like first ring. The right figures show the likelihood distribution of the most probable third ring candidate in each FC event which has the e-like first ring and the e-like second ring. Again, the peak fitting and the MC distribution adjustment are carried out to estimate the systematic uncertainty. From the left figures, the error on the multi-ring event extraction from all the events with the e-like first ring is estimated to be 1.8 %. From the right figures, the error on the two-ring e-like event extraction from the multi-ring events is estimated to be 3.1 %. We conservatively define the systematic uncertainty on the ring counting for π^0 events as the linear sum of the two errors (1.8 % and 3.1 %), resulting in $\sim$5 %.

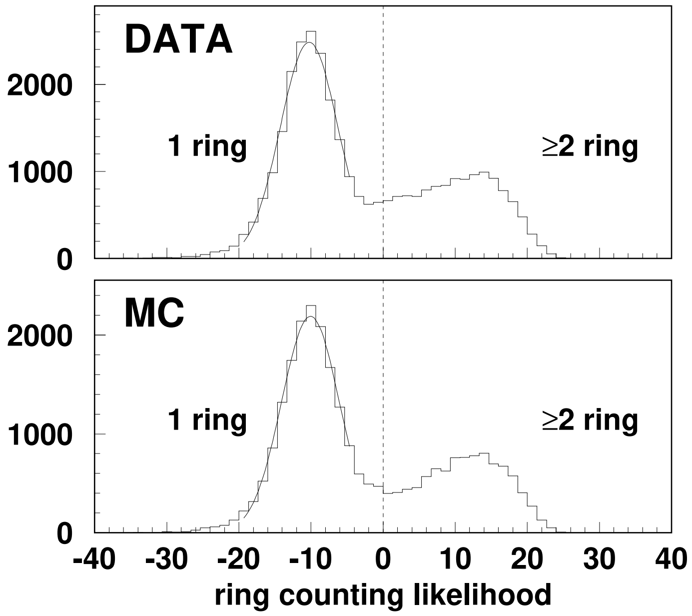

Figure 8.18: The likelihood distribution of the most probable second ring candidate in each FC event which has the μ-like first ring. The continuous line shows the fit with a Gaussian distribution.

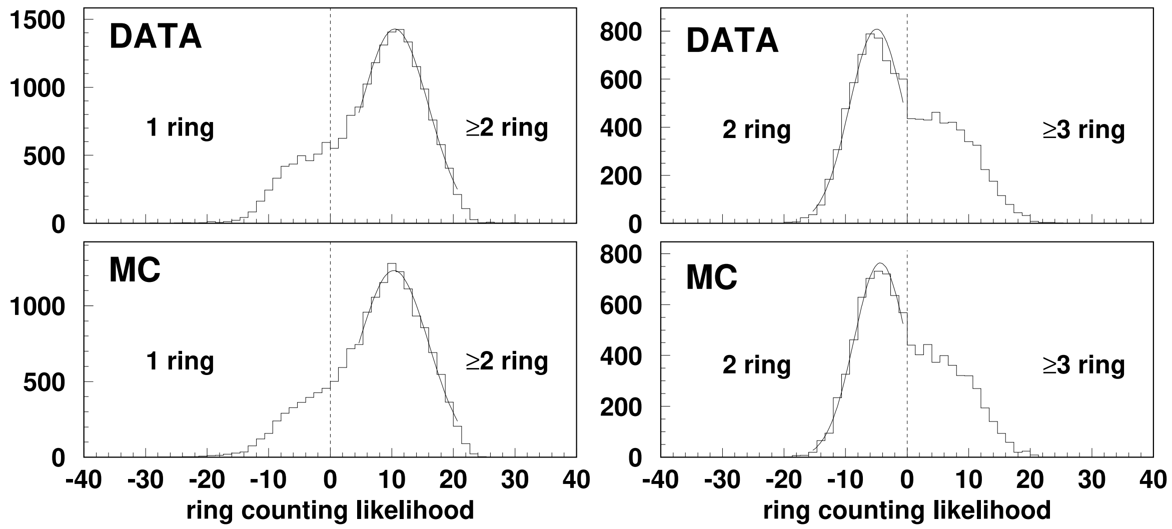

Figure 8.19: Left: The likelihood distribution of the most probable second ring candidate in each FC event which has the e-like first ring. Right: The likelihood distribution of the most probable third ring candidate in each FC event which has the e-like first ring and the e-like second ring.

Chapter 9

Oscillation Analysis

9.1 Application of the 1kt Result to SK

The best way to check the validity of π^0/μ expectation in our atmospheric neutrino Monte Carlo with no oscillations (*i.e.* the denominator of $R_{\pi^0}^{\mathrm{SK}}$) is to measure this ratio by exposing Super-Kamiokande to a neutrino beam having just the same energy spectra and neutrino compositions as those of actual atmospheric neutrinos. Such a plan is, however, very hard to realize. Instead, using the almost pure ν_μ beam before oscillations, we have measured R_{π^0} in the 1kt detector which is a miniature of SK. We have obtained the result very close to unity and its measurement uncertainty has been estimated to be about 9 %.

Since various distributions of the 1kt π^0 and μ samples demonstrate good agreement between data and MC (see the previous chapter), we assume that there is no difference between data and MC for the π^0 and μ detection efficiency. With this assumption,

$$R_{\pi^0}^{\mathrm{1kt}} = \frac{(N_{\pi^0}/N_\mu)_{\mathrm{Data}}}{(N_{\pi^0}/N_\mu)_{\mathrm{MC}}} = \frac{\left(\frac{N_{\pi^0}}{\varepsilon_{\pi^0}} \,/\, \frac{N_\mu}{\varepsilon_\mu}\right)_{\mathrm{Data}}}{\left(\frac{N_{\pi^0}}{\varepsilon_{\pi^0}} \,/\, \frac{N_\mu}{\varepsilon_\mu}\right)_{\mathrm{MC}}} = \frac{\left(N_{\pi^0}^{\mathrm{prod}} \,/\, N_\mu^{\mathrm{prod}}\right)_{\mathrm{Data}}}{\left(N_{\pi^0}^{\mathrm{prod}} \,/\, N_\mu^{\mathrm{prod}}\right)_{\mathrm{MC}}} \tag{9.1}$$

where N_{π^0} is the number of π^0 events, ε_{π^0} is the π^0 detection efficiency, $N_{\pi^0}^{\mathrm{prod}}$ is the number of π^0 productions, and the same definitions for μ. Therefore our measurement result proves that we have a good understanding of neutrino interactions and nuclear effects in the K2K neutrino energy region and the combined uncertainty on our expected production ratio ($= N_{\pi^0}^{\mathrm{prod}}/N_\mu^{\mathrm{prod}}$) due to these two is not more than about 9 %.

The production ratio depends only upon neutrino flux and cross section (including nuclear effects). Thus, if the SK atmospheric neutrino flux has been completely the same as the K2K neutrino beam flux, the π^0/μ production ratio in SK would be just the same as that in the 1kt, because both detectors use the same target (*i.e.* water). In such a case, the 9 % uncertainty due to neutrino interactions and nuclear effects could be used on the production ratio in SK without any change.

In reality, there exist some differences between the SK atmospheric neutrino flux and the K2K neutrino beam flux. Figure 9.1 shows the parent neutrino energy distribution for the π^0 samples extracted from K2K beam events in the 1kt and from atmospheric neutrino events in Super-Kamiokande. While atmospheric neutrinos producing π^0 events have a broad energy spectrum, almost all of beam neutrinos producing π^0 events are in the energy range between

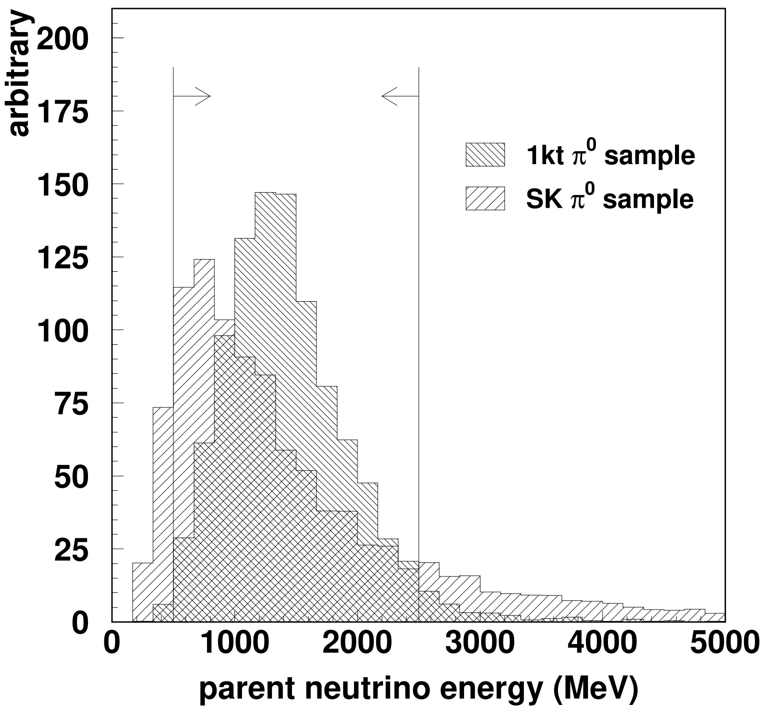

Figure 9.1: The parent neutrino energy distribution for the π^0 samples in the 1kt and SK. Almost all of beam neutrinos producing π^0 events in the 1kt are in the energy range between 500 MeV and 2500 MeV. Therefore we only apply the 1kt result to the SK analysis between these energies.

500 MeV and 2500 MeV. Thus, the $R_{\pi^0}^{\mathrm{1kt}}$ measurement result only indicates the accuracy of our MC prediction in SK between these energies.

As is clear from Figure 9.1, even in the neutrino energy range from 500 MeV to 2500 MeV, the spectra have slightly different shapes. This causes the different composition of π^0 producing interactions between in SK and in the 1kt. Our 1kt measurement can not confirm the validity of the MC simulation for individual interactions. Since it is possible that $R_{\pi^0}^{\mathrm{1kt}}$ is close to unity by accident, we vary the cross section for each interaction within its uncertainty in such a way that $R_{\pi^0}^{\mathrm{1kt}}$ remains equal to the original value. With different mixtures of neutrino interactions, changes on $R_{\pi^0}^{\mathrm{SK}}$ are evaluated. The maximum change is 3.5 %.

Moreover, atmospheric neutrinos contain ν_e, $\overline{\nu}_e$ and $\overline{\nu}_\mu$ as well as ν_μ, while the K2K beam is almost pure ν_μ beam. The 1kt measurement can not directly demonstrate the accuracy of our simulation for ν_e, $\overline{\nu}_e$ and $\overline{\nu}_\mu$ interactions. To consider the effect of this neutrino composition difference, we vary the relative cross section $\sigma(\overline{\nu})/\sigma(\nu)$ and $\sigma_{\mathrm{cc}}(\nu_e+\overline{\nu}_e)/\sigma_{\mathrm{cc}}(\nu_\mu+\overline{\nu}_\mu)$ separately by $\pm$ 10 % with ν_μ cross section being fixed. The maximum change on $R_{\pi^0}^{\mathrm{SK}}$ is about 1 %.

Combining these two additional error (3.5 % and 1 %) with the π^0/μ production ratio uncertainty of 9 %, we estimate the uncertainty on $R_{\pi^0}^{\mathrm{SK}}$ due to neutrino interactions and nuclear effects to be about 10 % for neutrinos of energies between 500 MeV and 2500 MeV. For neutrinos of energies outside the range, we use the original 18 % error (17 % from neutrino interactions

atmospheric neutrino flux	2 %
event reconstruction	7 %
energy scale	1.4 %
reduction	$<$ 1 %
MC statistics	1 %
cross section	
(E_ν: 500 MeV $\sim$ 2500 MeV	10 %)
(E_ν: $\sim$ 500 MeV	18 %)
(E_ν: 2500 MeV $\sim$	18 %)
flux averaged	12 %
total	14 %

Table 9.1: The systematic uncertainties on $R_{\pi^0}^{\mathrm{SK}}$ after application of the 1kt measurement result.

and 7 % from nuclear effects) shown in Table 6.5. The flux weighted uncertainty on $R_{\pi^0}^{\mathrm{SK}}$ due to neutrino interactions and nuclear effects is calculated to be 12 %.

Finally, the revised systematic uncertainty on $R_{\pi^0}^{\mathrm{SK}}$ is shown in Table 9.1. The total uncertainty is reduced from 20 % (see Table 6.5) down to 14 % by using the 1kt R_{π^0} measurement with the neutrino beam.

9.2 Results

As listed in Table 6.3, we have observed 471 π^0 events and 3845 μ events in a 1489.2 live days exposure of Super-Kamiokande. From the observed data and the atmospheric neutrino Monte Carlo with no oscillations, we obtain :

$$R_{\pi^0}^{\mathrm{SK}} = \frac{(\pi^0/\mu)_{\mathrm{Data}}}{(\pi^0/\mu)_{\mathrm{MC}_{\mathrm{no\ osc}}}} = 1.47 \pm 0.07\ (data\ stat.) \pm 0.21\ (sys.) \tag{9.2}$$

using the re-estimated total systematic uncertainty of 14 %. The result is significantly away from unity, indicating neutrino oscillations.

To test $\nu_\mu \leftrightarrow \nu_\tau$ and $\nu_\mu \leftrightarrow \nu_s$ oscillation scenarios, we calculate $R_{\pi^0}^{\mathrm{MC}}$:

$$R_{\pi^0}^{\mathrm{MC}} \equiv \frac{(\pi^0/\mu)_{\mathrm{MC\ osc}}}{(\pi^0/\mu)_{\mathrm{MC}_{\mathrm{no\ osc}}}} \tag{9.3}$$

for both hypotheses. Figure 9.2 shows the expected $R_{\pi^0}^{\mathrm{MC}}$ as a function of Δm^2 assuming the maximal mixing ($\sin^2 2\theta = 1$). Here, the matter effect in the earth is not considered. The result of our measurement is also shown with the estimated total uncertainty, which is a quadratic sum of the statistical error and the systematic error. A hatched area represents the Super-Kamiokande 90 % confidence level allowed range of Δm^2 in case of the maximal mixing [14]. At

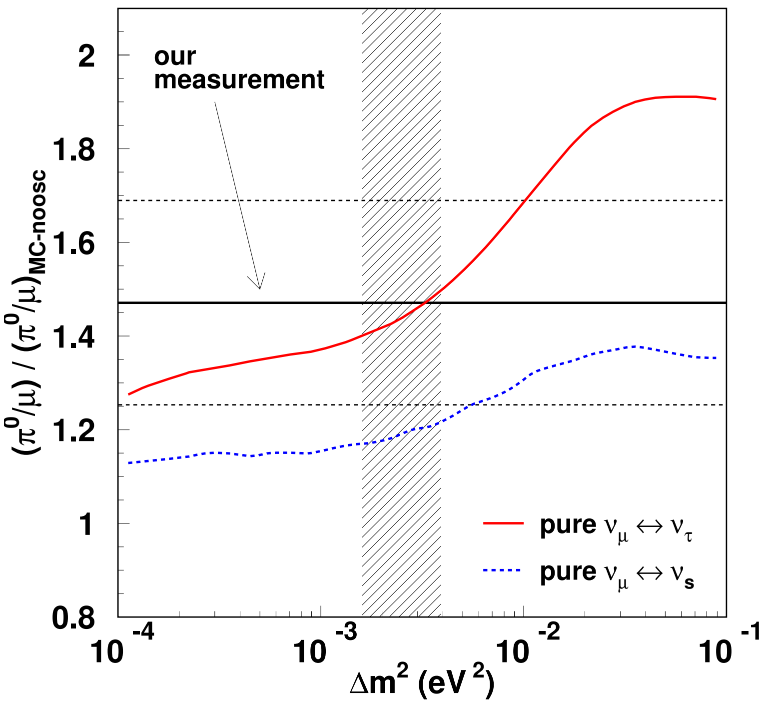

Figure 9.2: $R_{\pi^0}^{\rm MC}$ as a function of Δm^2 for the $\nu_\mu \leftrightarrow \nu_\tau$ case (solid curve) and the $\nu_\mu \leftrightarrow \nu_s$ oscillation case (dashed curve). The maximal mixing ($\sin^2 2\theta = 1$) is assumed. The result of our measurement (solid straight line) is also shown with the estimated error (dashed straight line). A hatched area represents the Super-Kamiokande 90 % confidence level allowed range of Δm^2 in case of the maximal mixing.

the Super-Kamiokande's best fit oscillation parameters $(\sin^2 2\theta, \Delta m^2) = (1.00,\ 2.5\times10^{-3}\ \mathrm{eV}^2)$, the expected values are as follows :

$$R_{\pi^0}^{\rm MC} = 1.44 \qquad \text{for} \quad \nu_\mu \leftrightarrow \nu_\tau \quad \text{oscillations} \tag{9.4}$$

$$R_{\pi^0}^{\rm MC} = 1.19 \qquad \text{for} \quad \nu_\mu \leftrightarrow \nu_s \quad \text{oscillations} \tag{9.5}$$

Our measurement is found to be more consistent with the $\nu_\mu \leftrightarrow \nu_\tau$ oscillation hypothesis, while the $\nu_\mu \leftrightarrow \nu_s$ oscillation hypothesis is about $1.3\,\sigma$ away.

In the test region of Δm^2 above $1.0 \times 10^{-3}\,\mathrm{eV}^2$, this analysis is independent of the matter effect. Even if we include the matter effect into our simulation, this result does not change because neutrinos producing the π^0 sample and the μ sample do not have sufficiently high energies to be affected by the matter in the Earth. This result favoring $\nu_\mu \leftrightarrow \nu_\tau$ oscillations is consistent with the result obtained by the Super-Kamiokande analysis using matter effects on high energy muon neutrinos [27].

Chapter 10

Conclusion

In 1998, Super-Kamiokande reported evidence for oscillations of atmospheric muon neutrinos [13]. However, the data did not distinguish whether muon neutrinos were oscillating into tau neutrinos or sterile neutrinos. To distinguish these two hypotheses, Super-Kamiokande studied the difference in zenith angle distribution due to neutral currents and matter effects. Three complementary data samples which enhance the difference were used, and the $\nu_\mu \leftrightarrow \nu_s$ hypothesis was excluded at the 99 % confidence level, in 2000 [27].

As another way to distinguish between $\nu_\mu \leftrightarrow \nu_\tau$ and $\nu_\mu \leftrightarrow \nu_s$, we have measured a double ratio $R_{\pi^0} = (\pi^0/\mu)_{\rm Data} \,/\, (\pi^0/\mu)_{\rm MC}$ for the atmospheric neutrino sample in Super-Kamiokande. Since the single π^0 sample has a large NC fraction, the two scenarios make a difference in R_{π^0}. The estimated total systematic uncertainty on R_{π^0} is about 20 %, which mainly comes from pion production cross sections and nuclear effects in oxygen nuclei. The 20 % uncertainty is the same order as the expected attenuation of neutral current events in the $\nu_\mu \leftrightarrow \nu_s$ case.

To test our Monte Carlo simulation and reduce the systematic uncertainty on R_{π^0}, we have made a measurement of R_{π^0} in the 1kt water Cherenkov detector using K2K beam neutrinos before oscillations. A total of 5133 π^0 events was observed in the 1kt detector during the K2K running period from January to March, 2000 and from January to July, 2001. The result is :

$$R_{\pi^0}^{\rm 1kt} \;=\; \frac{\left(\pi^0/\mu\right)_{\rm Data}}{(\pi^0/\mu)_{\rm MC}} \;=\; 1.00 \pm 0.02 \ (data\ stat.) \pm 0.09 \ (sys.)$$

indicating very good agreement between the observed data and our Monte Carlo expectation. Our measurement uncertainty on R_{π^0} in the 1kt detector is estimated to be about 9 %.

We carefully apply this result to SK R_{π^0} in the neutrino energy region from 500 MeV to 2500 MeV, over which neutrinos producing 1kt π^0 events are distributed. The total systematic uncertainty on SK R_{π^0} is reduced from 20 % to 14 %. Using the events observed in a 1489.2 live days exposure of Super-Kamiokande, we obtain :

$$R_{\pi^0}^{\rm SK} \;=\; \frac{\left(\pi^0/\mu\right)_{\rm Data}}{(\pi^0/\mu)_{{\rm MC}_{\rm no\ osc}}} \;=\; 1.47 \pm 0.07 \ (data\ stat.) \pm 0.21 \ (sys.)$$

indicating disagreement between the observed data and the prediction with no oscillations. The expectations with the two oscillation hypotheses, $\nu_\mu \leftrightarrow \nu_\tau$ and $\nu_\mu \leftrightarrow \nu_s$, are :

$$R_{\pi^0}^{\mathrm{MC}} = 1.44 \qquad \text{for} \ \ \nu_\mu \leftrightarrow \nu_\tau \ \ \text{oscillations}$$

$$R_{\pi^0}^{\mathrm{MC}} = 1.19 \qquad \text{for} \ \ \nu_\mu \leftrightarrow \nu_s \ \ \text{oscillations}$$

at the Super-Kamiokande's best fit oscillation parameters $(\sin^2 2\theta, \Delta m^2) = (1.00,\ 2.5\times10^{-3}$ eV$^2)$ [14]. The measured $R_{\pi^0}^{\mathrm{SK}}$ is found to be more consistent with the $\nu_\mu \leftrightarrow \nu_\tau$ oscillation hypothesis, while the $\nu_\mu \leftrightarrow \nu_s$ oscillation hypothesis is about $1.3\,\sigma$ away.

Though this analysis is independent of matter effects in the test region of Δm^2 above $1.0 \times 10^{-3}\,\mathrm{eV}^2$, our result favoring $\nu_\mu \leftrightarrow \nu_\tau$ oscillations is consistent with the result obtained by the SK analysis using matter effects on high energy muon neutrinos [27].

Appendix A

Neutrino Beam Simulation

The K2K neutrino beam flux is simulated using the following procedure :

(1) Protons are injected into the target according to the measured beam emittance.

(2) Secondary pions and kaons are generated at the target using hadronic interaction models.

(3) Generated particles are tracked through magnetic fields of the horns.

(4) Pions, kaons and muons are made to decay into neutrinos.

The beam simulation program is based on the GEANT tool [82]. Below is the brief explanation of each stage.

A.1 Proton Injection into the Target

In the first stage of the neutrino beam simulation, protons are injected into the target according to the measured beam emittance. As illustrated in Figure A.1, the proton emittance at the target is estimated with the extrapolation of beam profiles measured by two SPICs between the last magnet and the target. Here, we assume that beam profiles have two-dimensional Gaussian distributions and protons do not cross over. The simulated beam emittance at the target is shown in Figure A.2.

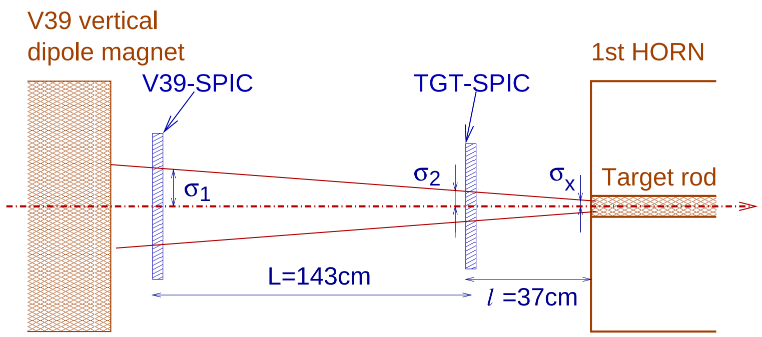

Figure A.1: A schematic view of the proton beam emittance measurement.

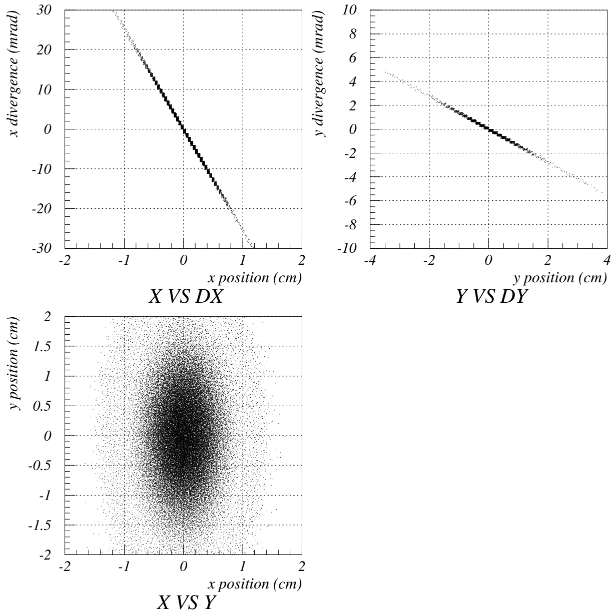

Figure A.2: The simulated beam emittance at the target. The upper figures show the beam divergence and the lower figure shows the beam profile.

A.2 Production of Secondary Pions and Kaons at the Target

This part gives the largest ambiguity in our beam simulation. Various pion production experiments have been carried out in the K2K beam energy region, but some of their results are inconsistent with one another. Therefore, there exist some possible hadronic interaction models to simulate secondary particle production at the target. We compare the following two models.

1. **GCALOR/FLUKA Model**
   GCALOR/FLUKA is one of the hadronic interaction interfaces for GEANT simulation package [83, 100]. This model gives the larger p-Al cross section and produces higher energy secondary pions than other models.

2. **Cho Model**
   This model is an experimental parameterization of Sanford-Wang formula, which describes the differential yield of secondary particles as follows [101] :

$$\frac{d^2n}{d\theta dp} = C_1 \cdot p^{C_2} \left(1 - \frac{p}{p_B}\right) \exp\left(-\frac{C_3 \cdot p^{C_4}}{p_B^{C_5}} - C_6 \cdot \theta \cdot \left(p - C_7 \cdot p_B \cdot \cos^{C_8} \theta\right)\right) \qquad \text{(A.1)}$$

   where p_B is primary proton momentum, p is secondary particle momentum and θ is an angle between the secondary particle direction and the initial beam direction. Cho *et al.* determined the eight constants $C_1 \sim C_8$ by the global fit using their own measurement results and other experimental results [102, 103, 104, 105]. The result of the fit by Cho

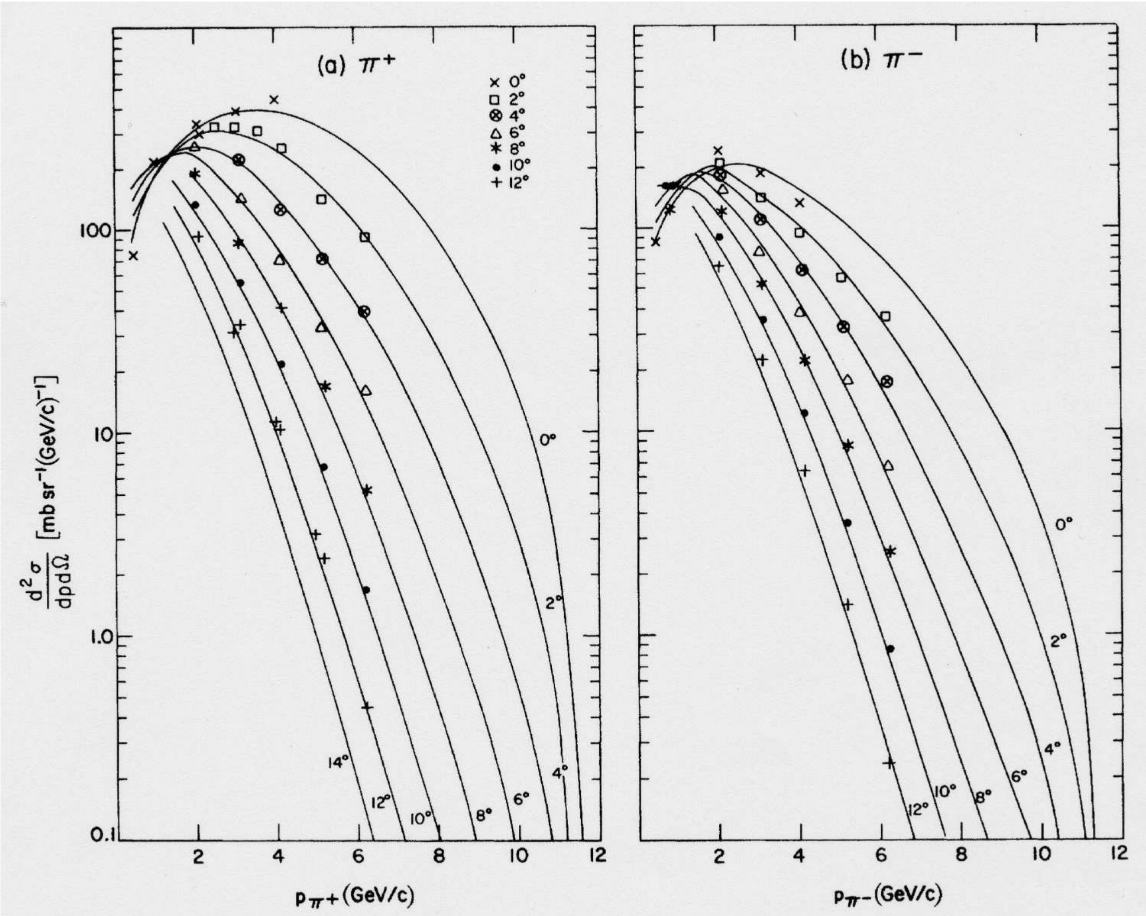

Figure A.3: The cross sections for (a) π^+ production and (b) π^- production [102]. The dots represent the experimental data. The lines represent the result of the fit by Cho *et al.* using Sanford-Wang Formula (Equation (A.1)).

	C_1	C_2	C_3	C_4	C_5	C_6	C_7	C_8
π^+	196	1.08	2.15	2.31	1.98	5.73	0.137	24.1
π^-	161	0.90	1.55	1.68	1.19	5.09	0.149	29.2

Table A.1: The parameters in Sanford-Wang Formula (Equation (A.1)) for pion production as the result of the fit by Cho *et al.* [102].

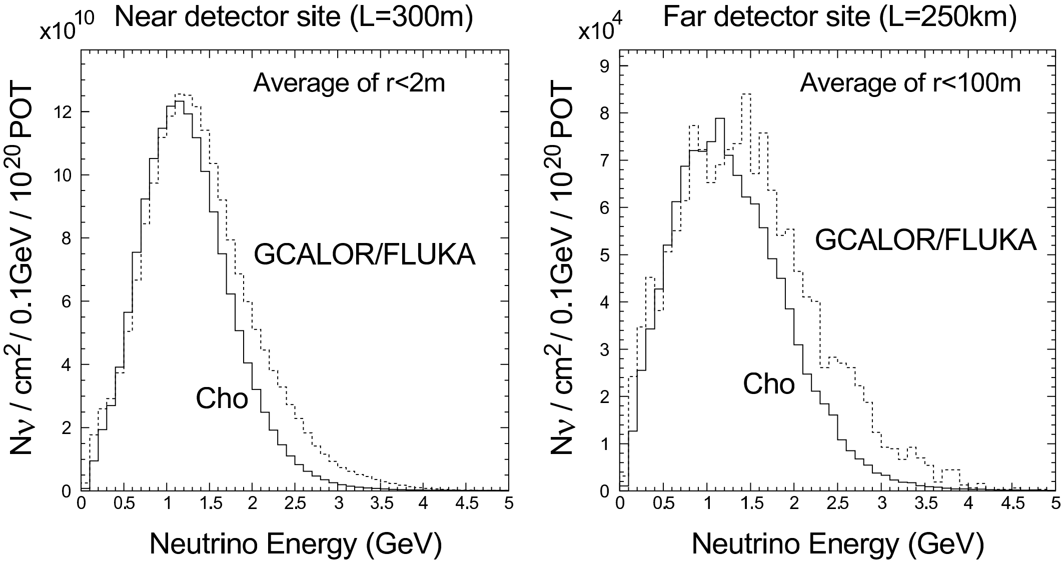

Figure A.4: The simulated ν_μ flux at the near site (left) and at the far site (right) with GCALOR/FLUKA model (dashed histograms) and Cho model (solid histograms).

et al. for pion production are shown in Figure A.3 and Table A.1. Note that this model is used only for simulation of primary interaction of protons. For simulation of secondary interaction of hadrons, GCALOR/FLUKA is always used. In addition, Ref.[106] is referred to for simulation of kaon production.

Figure A.4 shows the dependence of the expected ν_μ flux on hadronic interaction models. We adopt Cho model because the measured photon distribution in PIMON is reproduced very well by the beam simulation using Cho model [92].

A.3 Particle Tracking through Magnetic Fields of the Horns

Generated secondary particles are tracked through magnetic fields created by the horns. As for the strength of fields, calculated values are inputted to the program (see Equation (7.1)). The reliability of the calculation is confirmed by measurement using pickup coils [107].

A.4 Decay of Particles into Neutrinos

GEANT simulates particle decay with isotropic angular distribution in the center-of-mass system [82]. Therefore, for the three-body weak decay of kaons or muons, energies and directions of decay products are simulated by our custom code based on the V-A theory.

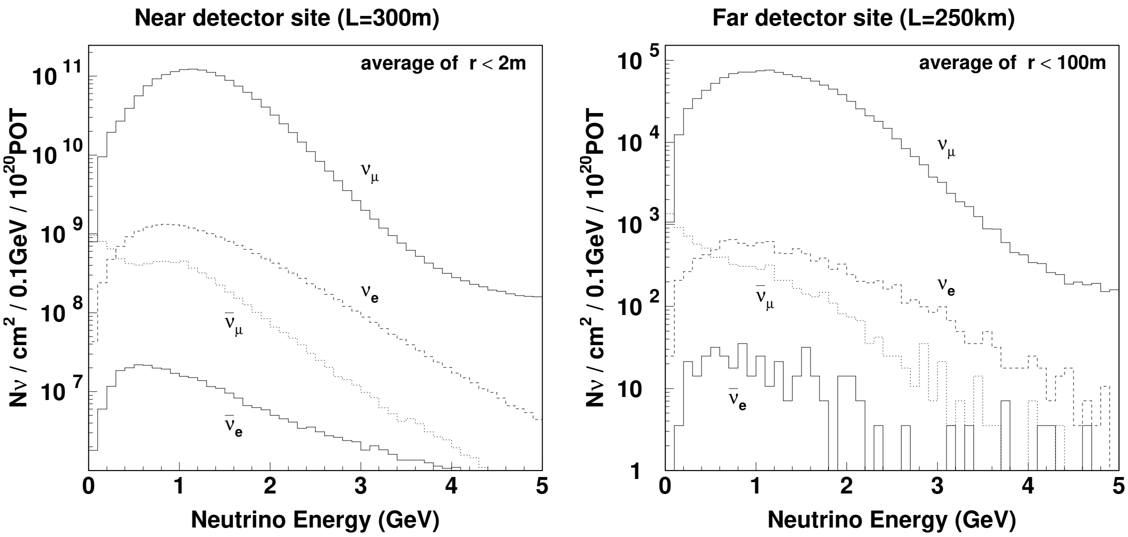

Figure A.5: The simulated flux of each neutrino component at the near site (left) and at the far site (right).

A.5 Simulated Beam Flux

Figure A.5 shows the simulated flux of each neutrino component at the near site and at the far site. It is found that ν_μ's account for 98.2 % of the flux at the near site. Almost all the ν_μ's are made by π^+ decays in the neutrino energy region below 4 GeV, while K^+ decays have the dominant contribution to the ν_μ production in the higher energy region. The fraction of ν_e, $\overline{\nu}_\mu$ and $\overline{\nu}_e$ at the near site is estimated to be about 1.3 %, 0.5 % and 0.02 %, respectively. Here, ν_e's are mostly produced by decays of μ^+'s which come from π^+ decays. The $\overline{\nu}_\mu$ contamination is due to decays of π^-'s which can not be swept away by magnetic fields of the horns.

The average neutrino energy within 2 m of the beam center is about 1.25 GeV at the near site, and the peak energy is about 1.15 GeV.

Bibliography

[1] M. Honda *et al.*, Phys. Rev. **D52**, 4985 (1995).

[2] V. Agrawal *et al.*, Phys. Rev. **D53**, 1314 (1996).

[3] K.S. Hirata *et al.*, Phys. Lett. **B205**, 416 (1988).

[4] K.S. Hirata *et al.*, Phys. Lett. **B280**, 146 (1992).

[5] D. Casper *et al.*, Phys. Rev. Lett. **66**, 2561 (1991).

[6] R. Becker-Szendy *et al.*, Phys. Rev. **D46**, 3720 (1992).

[7] S.L. Glashow, Nucl. Phys. **22**, 579 (1961).

[8] S. Weinberg, Phys. Rev. Lett. **19**, 1264 (1967).

[9] A. Salam, In *Proceedings of the 8th Nobel Symposium on Elementary particle theory, relativistic groups and analyticity*, edited by N. Svartholm (1969).

[10] Z. Maki, M. Nakagawa, and S. Sakata, Prog. Theo. Phys. **28**, 870 (1962).

[11] Y. Fukuda *et al.*, Phys. Lett. **B433**, 9 (1998).

[12] Y. Fukuda *et al.*, Phys. Lett. **B436**, 33 (1998).

[13] Y. Fukuda *et al.*, Phys. Lett. **81**, 1562 (1998).

[14] M. Ishitsuka for the Super-Kamiokande Collaboration, In *Proceedings of the XVI International Conference on Particles and Nuclei*, to be published.

[15] S.H. Ahn *et al.*, Phys. Lett. **B511**, 178 (2001).

[16] S. Fukuda *et al.*, Phys. Rev. Lett. **86**, 5656 (2001).

[17] Q.R. Ahmad *et al.*, Phys. Rev. Lett. **89**, 011301 (2002).

[18] S. Fukuda *et al.*, Phys. Lett. **B539**, 179 (2002).

[19] K. Eguchi *et al.*, hep-ex/0212021 (2002).

[20] C. Athanassopoulos *et al.*, Phys. Rev. Lett. **77**, 3082 (1996).

[21] B. Armbruster *et al.*, Phys. Rev. **D65**, 112001 (2002).

[22] A. Aguilar *et al.*, Phys. Rev. **D64**, 112007 (2001).

[23] D. Decamp *et al.*, Z. Phys. **C35**, 1 (1992);
P. Abreu *et al.*, Nucl. Phys. **B367**, 511 (1992);
B. Adeva *et al.*, Z. Phys. **C51**, 179 (1991);
G. Alexander *et al.*, Z. Phys. **C52**, 175 (1992).

[24] L. Wolfenstein, Phys. Rev. **D17**, 2369 (1978).

[25] S.P. Mikheyev and A.Y Smirnov, Sov. J. Nucl. Phys. **42**, 1441 (1985);
S.P. Mikheyev and A.Y Smirnov, Nouvo Cimento Soc. Ital. Fis. **9C**, 17 (1986);
S.P. Mikheyev and A.Y Smirnov, Sov. Phys.-Usp. **30**, 759 (1987).

[26] E. Akhmedov, P. Lipari and M. Lusignoli, Phys. Lett. **B300**, 128 (1993);
P. Lipari and M. Lusignoli, Phys. Rev. **D58**, 73005 (1998);
Q.Y. Liu and A.Y. Smirnov, Nucl. Phys. **B524**, 505 (1998);
Q.Y. Liu, S.P. Mikheyev and A.Y. Smirnov, Phys. Lett. **B440**, 319 (1998).

[27] S. Fukuda *et al.*, Phys. Rev. Lett. **85**, 3999 (2000).

[28] H. Kume *et al.*, Nucl. Inst. and Meth. **205**, 443 (1983).

[29] A. Suzuki *et al.*, Nucl. Inst. and Meth. **A329**, 299 (1993).

[30] R. Claus *et al.*, Nucl. Inst. and Meth. **A261**, 540 (1987).

[31] H. Ikeda *et al.*, Nucl. Inst. and Meth. **A320**, 310 (1992).

[32] T.Tanimori *et al.*, IEEE Trans. Nucl. Sci. **NS-36**, 497 (1989).

[33] J. George, Ph.D. Thesis, University of Washington (1998).

[34] Y. Kitaguchi, Master Thesis, Niigata University (1996).

[35] T. Shiabata, Master Thesis, Niigata University (2002).

[36] P. Hanggi *et al.*, Phys. Lett. **B51**, 119 (1974)

[37] M. Yamada *et al.*, Phys. Rev. **D44** 617 (1991)

[38] D. Rein and L.M. Sehgal, Nucl. Phys **B233**, 29 (1983).

[39] C.H. Llewellyn Smith, Phys. Rep. **3**, 261 (1972).

[40] H. Grabosch *et al.*, Z. Phys. **C41**, 527 (1989).

[41] S. Barish *et al.*, Phys. Rev. **D16**, 3103 (1977).

[42] S. Bonetti *et al.*, Nouvo Cimento **38**, 260 (1977).

[43] M. Pohl *et al.*, Nuovo Cimento **26**, 332 (1979);
N. Arimenise *et al.*, Nucl. Phys. **B152**, 365 (1979).

[44] A.S. Vovenko *et al.*, Yad. Fiz. **30**, 1014 (1979).

[45] S. Belikov *et al.*, Z. Phys. **320**, 625 (1985).

[46] C.H. Albright *et al.*, Phys. Rev. **D14**, 1780 (1976).

[47] K. Abe *et al.*, Phys. Rev. Lett. **56**, 1107 (1986).

[48] K. Nakamura *et al.*, Nucl. Phys. **A268**, 381 (1976).

[49] D. Rein and L.M. Sehgal, Ann. of Phys. **133**, 1780 (1981).

[50] R. Feynman *et al.*, Phys. Rev. **D3**, 2706 (1971).

[51] G. Radecky *et al.*, Phys. Rev. **D25**, 116 (1982).

[52] T. Kitagaki *et al.*, Phys. Rev. **D34**, 2554 (1986).

[53] P. Allen *et al.*, Nucl. Phys. **B264**, 221 (1986).

[54] P. Allen *et al.*, Nucl. Phys. **B176**, 269 (1980).

[55] W. Lerche *et al.*, Phys. Lett. **4**, 510 (1978).

[56] J. Bell *et al.*, Phys. Rev. Lett. **15**, 1008 (1978).

[57] D. Allisia *et al.*, Z. Phys. **C24**, 119 (1984).

[58] S.J. Barish *et al.*, Phys. Lett. **B91**, 161 (1980).

[59] M. Derrick *et al.*, Phys. Rev. **D23**, 569 (1981).

[60] C.H. Albright and C. Jarlskog, Nucl Phys. **B84**, 467 (1975).

[61] M. Glück, E. Reya and A. Vogt, Z. Phys. **D57**, 433 (1995).

[62] S.J. Barish *et al.*, Phys. Rev. **D17**, 1 (1978).

[63] S. Barlag *et al.*, Z. Phys. **C11**, 283 (1982).

[64] T. Sjöstrand *et al.*, CERN-TH-7112-93 (1994).

[65] P. Musset and J.P. Vialle, Phys. Rep. **C39**, 1 (1978).

[66] J.E. Kim *et al.*, Rev. Mod. Phys. **53**, 211 (1981).

[67] P.S. Auchincloss *et al.*, Z. Phys. **C48**, 411 (1990).

[68] P. Berger *et al.*, Z. Phys. **C35**, 443 (1987).

[69] S. Campolillo *et al.*, Phys. Lett. **84B**, 281 (1979).

[70] O. Erriquez *et al.*, Phys. Lett. **89B**, 309 (1979).

[71] J.V. Allaby *et al.*, Z. Phys. **C38**, 403 (1988).

[72] N.J. Baker *et al.*, Phys. Rev. **D25**, 617 (1982).

[73] C. Baltay *et al.*, Phys. Rev. Lett. **44**, 916 (1980).

[74] D.C. Colley *et al.*, Z. Phys. **C2**, 187 (1979).

[75] V.B. Anikeev *et al.*, Z. Phys. **C70**, 39 (1996).

[76] A.S. Vovenko *et al.*, Yad. Fiz. **30**, 187 (1979).

[77] D.B. MacFarlane *et al.*, Z. Phys. **C26**, 1 (1984).

[78] D.S. Baranov *et al.*, Phys. Lett. **81B**, 255 (1979).

[79] E. Oset *et al.*, Nucl. Phys. **A484**, 557 (1988).

[80] G. Rowe *et al.*, Phys. Rev. **C18**, 584 (1978).

[81] C. Ingram *et al.*, Phys. Rev. **C27**, 1578 (1983).

[82] GEANT, CERN Program Library Long Writeup W5013 (1994).

[83] C. Zeitnitz and T.A. Gabriel, Nucl. Inst. and Meth. **A349**, 106 (1994).

[84] M. Nakahata *et al.*, J. Phys. Soc. Jpn. **55**, 3786 (1986).

[85] E. Bracci *et al.*, CERN/HERA 72-1 (1972).

[86] A.S. Carrol *et al.*, Phys. Rev. **C14**, 635 (1976).

[87] ZEBRA, CERN Program Library Long Writeups Q100/Q101 (1995).

[88] A. Kibayashi, Ph.D. Thesis, University of Hawaii (2002).

[89] E.R. Davies, *Machine Vision: Theory, Algorithms, Practicalities*, Academic Press, San Diego (1997).

[90] K. Ishihara, Ph.D. Thesis, University of Tokyo (1999).

[91] KEK-PS USERS GUIDE BOOK, KEK Publication (1992).

[92] T. Maruyama, Ph.D. Thesis, Tohoku University (2000).

[93] M. Yoshida, Ph.D. Thesis, Osaka University (2001).

[94] T. Inagaki, Ph.D. Thesis, Kyoto University (2001).

[95] S. Kasuga, Master Thesis, University of Tokyo (1995).

[96] A. Shima, Master Thesis, Kyoto University (2002).

[97] H.C. Kim *et al.*, Phys. Rev. **C53**, 3131 (1996).

[98] S.K. Singh *et al.*, Phys. Lett. **B416**, 23 (1998).

[99] J. Marteau *et al.*, Nucl. Phys. **A663**, 783 (2000).

[100] A. Fassò *et al.*, Fluka92, In *Proceedings of the Workshop on Simulating Accelerator Radiation Environments*, Santa Fe, USA, 11-15 January 1993.

[101] J.R. Sanford and C.L. Wang, BNL-AGS internal report (1967), unpublished;
C.L. Wang, Phys. Rev. Lett. **25**, 1068 (1970).

[102] Y. Cho *et al.*, Phys. Rev. **D4**, 1967 (1971).

[103] J.G. Asbury etal, Phys. Rev. **178**, 2086 (1969).

[104] G.J. Marmer *et al.*, Phys. Rev. **179**, 1294 (1969);
G.J. Marmer *et al.*, Phys. Rev. **D3**, 1089 (1971).

[105] J.V. Allaby *et al.*, CERN Report No. CERN-TH-70-12, unpublished.

[106] A. Yamamoto, "Study On Low-Energy Intense Kaon Beam", KEK 81-13.

[107] M. Kohama, Master Thesis, Kobe University (1997).